NEW APPLICATIONS IN DIGITAL ENGINEERING

EDITED BY
Prof. Dr. Ahmet FERTELLİ

NEW APPLICATIONS IN DIGITAL ENGINEERING

EDITED BY

Prof. Dr. Ahmet FERTELLİ

AUTHORS

Prof. Dr. K. Turgut GÜRSEL

Assoc. Prof. Dr. Ege Anıl DİLER
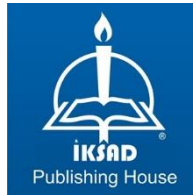
Assoc. Prof. Dr. Sevil AKÇAĞLAR

Dr. Harun SÜMBÜL

Dr. Taner ÇARKIT

Can KIRAN

Mech. Eng. Cemile KAYIŞ

MSc. Mete BERBEROĞLU

Phd(c). Sümeyye ÇARKIT

It is responsibility of the author to abide by the publishing ethics rules.

Iksad Publications – 2023©

CONTENTS

PREFACE

Digitalization, which develops with advancing technology all over the world, has started to play an active role in all areas. The first industrial revolution, which enabled the transition from manual labor to machinery, the second industrial revolution, in which mass production could be achieved by using electricity in production, and the third industrial revolution, in which advanced technologies in both electronics and automation and the use of robots provided significant increases in quality and efficiency, have been completed. Nowadays, the fourth industrial revolution phase has passed, and in this period called Industry 4.0, a new era begins where digital engineering is effective with topics such as simulation, autonomous robots, internet of things, augmented reality big data, cyber security, additive manufacturing, cloud computing and artificial intelligence.

Our book consists of 6 chapters. In the first chapter, the impact and collision of a bulbous bow section into container ship sections with different constructive elements are simulated by ANSYS-LS-DYNA software. The chapter is titled as "*Analysis of Ship's Side Collisions.*"

The second chapter introduces Direct Air Capture (DAC) technology and materials, which are utilized to capture CO2 that has already been emitted into the environment. The chapter is headed "*Advancements in Technology and Materials for Direct Air Capture: A Comprehensive Overview*"

In the third chapter, researchers developed a simulator system to explore sleep apnea, including its types, physiological formation, and basic breathing characteristics. This was achieved by creating a pneumatic circuit and an electronic circuit, with a microcontroller operating the circuit. The title of the paper is "*A Novel Sleep Apnea Simulator Tool: A Mems Based Approach*".

Chapter four of the book focuses on quantum image processing, providing in-depth analysis of quantum computers and non-destructive testing techniques. The chapter is titled "*Applications of Quantum Technology in Image Processing: A Review Study on Electric-Electronic Based Detection and Non-Destructive Testing Methods*".

Chapter five provides a comprehensive overview of diverse techniques used to synthesize silver nanoparticles, as well as their applications in many fields. The chapter is titled "*Synthesis of Silver Nanoparticles*".

Chapter six discusses the use of nanocomposites subjected to sunlight radiation for the treatment of surface water containing polyaromatic hydrocarbons. The chapter is titled "*Treatment of Polyaromatic Hydrocarbons (Pahs) From Surface Water Using $Zno/Na_2S_2O_8$ Nanocomposite Under Sunlight Irradiation*".

For the chapters, all responsibilities for the provided content belong to the authors. We would like to thank everyone who contributed to the preparation of this book and hope it will be useful.

Prof. Dr. Ahmet FERTELLİ

CHAPTER 1

ANALYSIS OF SHIP'S SIDE COLLISIONS

Prof. Dr. K. Turgut GÜRSEL[1]

Can KIRAN[2]

DOI: https://dx.doi.org/10.5281/zenodo.10447837

[1] Dokuz Eylül Üniversitesi, Deniz Bilimleri ve Teknolojisi Enstitüsü, Gemi İnşaatı Programı, Haydar Aliyev Bulvarı, No: 32, Balçova - 35330 İzmir, Türkiye, turgut.gursel@deu.edu.tr
ORCID NO: 0000-0002-9681-680X

[2] Dokuz Eylül Üniversitesi, Deniz Bilimleri ve Teknolojisi Enstitüsü, Gemi İnşaatı Programı, Haydar Aliyev Bulvarı, No: 32, Balçova - 35330 İzmir, Türkiye, can.kıran@ogr.deu.edu.tr
ORCID NO: 0000-0003-1329-4493

INTRODUCTION

Approximately 80% of the products produced in the world are transported by sea. Therefore, collision of ships with each other are very common in ports, which are the loading and unloading places of these cargoes, in the entrance-exit areas of ports and in busy straits and canals, where heavy sea traffic occurs, especially in cases where foggy and severe weather conditions prevail. Therefore, major environmental disasters occur as a result of a ship colliding with a tanker from the side, while high insurance losses are inevitable depending on the cargo carried by a cargo ship crashed from the side. (Fig. 1 and 2).

The oil transportation by tankers, which can also be defined as large-volume crude oil transportation, constitutes approximately half of the tonnage carried in all sea transportation. Tankers' tanks are either completely empty or they only carry liquid crude or processed oil in their full tanks. Oil pollution emitted into the sea as a result of any ship colliding with a tanker or tankers crashing with each other often causes major environmental disasters. This situation not only negatively affects coastal and marine ecosystems, but also has economically destructive effects as it completely damages the sea products in natural or production farms and prevents various recreational activities. It is stated that approximately 5 million tons of oil and petroleum derivatives are emitted into the seas every year.

The interest in oil pollution caused by ship accidents increased mainly after the oil tanker Torrey Canyon ran aground in the Isles of Scilly in 1967 and approximately 119,000 tons of oil spilled into the sea. After this accident, the MARPOL 1973 Convention (The International Convention for the Prevention of Pollution from Ships) came to the fore and new rules such as International Convention on Civil Liability for Oil Pollution Damage (CLC 1969) were established (Onay, 2020).

In this study, the impact and collision of a bulbous bow section into container ship sections with different constructive elements will be simulated. By making limited changes to the ship's section construction, it is investigated primarily to protect its inner plates from damages and then to effectively limit the whole damages on its outer plates.

The first part of the study aims to provide information about the disaster dates and leaks from previous accidents. In the second part, the selected methods and materials were verified by previous physical tests. In the third part, the double-hulled ship construction section was modeled, and collision analyses were carried out.

Fig. 1: Tanker in flame (hurriyetdailynews.com) **Fig. 2:** Ship crash (MarineDeal News)

The scenario of a cargo ship colliding with the side of a tanker and a container ship from the bow will be analyzed in detail by using the ANSYS-LS-DYNA software, and damage analyzes will be carried out by investigating the energy and deformation mechanisms that occur during the collision. In the final section, the findings are listed item by item and countermeasures are presented as suggestions. The result of the study is of great importance in terms of the shipbuilding sector taking measures for the protection of ships and, thus, the environment.

1. MATERIALS AND METHOD

The behavior of damage during ship collisions is basically defined by ship construction and plate thickness. It is the best solution if constructive measures are taken beforehand during the design of tankers and cargo ships by anticipating these major damages. For this, it is possible to develop durable constructions by simulating various collision scenarios in the early stages of the ship design.

Thus, during the design phase of tankers and other ships, it will be possible to develop constructive measures economically in order to prevent environmental disasters and to limit material damages completely.

1.1 Verification of TNO-Crash Experiment

In the test carried out by striking the bulbous bow model of Nedlloyd 34 against the side of the ship model named Amatha, the bow is given as 762 tons and the construction mass of Amatha is given as 1442 tons. The ship height is 4.2 meters, and the cross-section length is 7.5 meters. The thickness of the plates used in the experiment is between 4-6 mm and its quality is at A level in Romanian standards.

In the experiment, Nedlloyd's bow model was ensured to crash into Amatha's side with a speed of 2.55 m/s. The collision lasted about 1 s and the depth of penetration was approximately 1 meter. The distribution of the force generated during the collision in the experiment is given in Figure 3.

In this study, hull and bulbous bow models of the ships were created and meshed in the LS-DYNA software. In the creation of the model mesh structures, the element of 200 type was used. The hull of the ship Amatha was modelled in a ratio of 1:3 for the tests and the crashed ship hull is modeled as a double hull given in Fig. 4.

As the boundary conditions, the crashed ship's side was fixed on both sides as clamped, and the initial velocity and mass per node were defined. The steel A240 was selected as the material that was assumed to have linear elastic-plastic properties (Table 1), and the analyses were run.
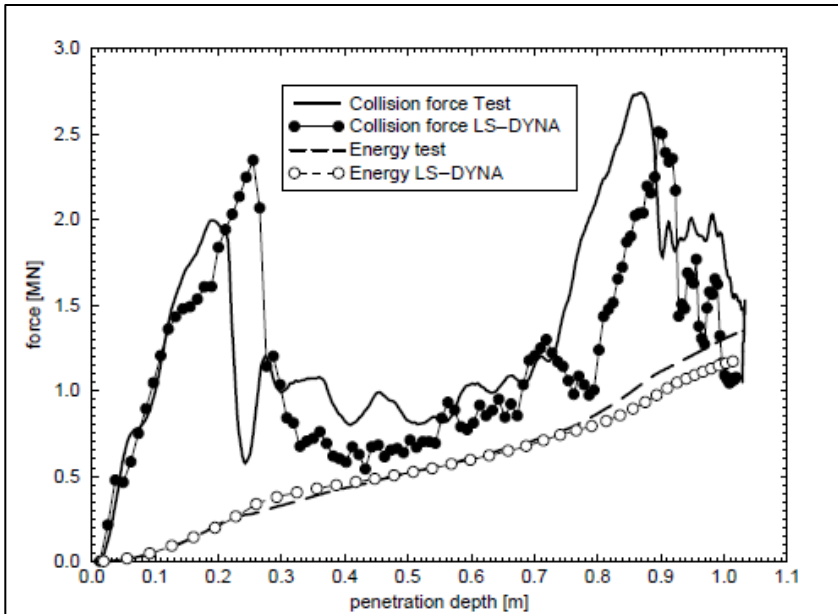
Fig. 3: Values of the force and energy versus penetration depth measured in the experiment (Lehmann and Peschmann, 2001)

While creating the boundaries, support points were visually assigned from the test data. The experimental setup was installed and measured by probes that were placed squarely around the target plates, and thus the damage in the event of collision was investigated elaborately.
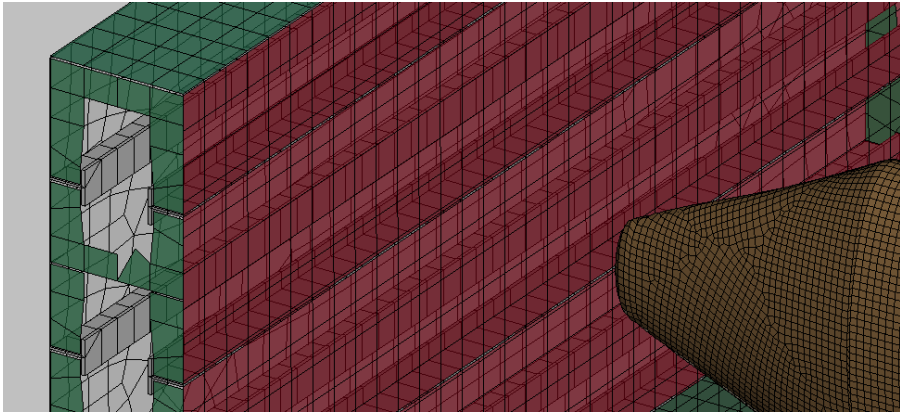
Fig. 4: Creating the mesh structure of the ship model Amatha

Table 1: Mechanical properties of AH36 and A240 Steel

Mechanical Properties	AH 36 Steel (ASTM)	A240 Steel (ASTM)
Yield Stress (MPa)	355.0	195.0
Tensile Strength (MPa)	490-630	250-275
Minimum Strain	0.21	-
Young Modulus (MPa)	206.0	193.0
Poisson Ratio	0.30	0.29
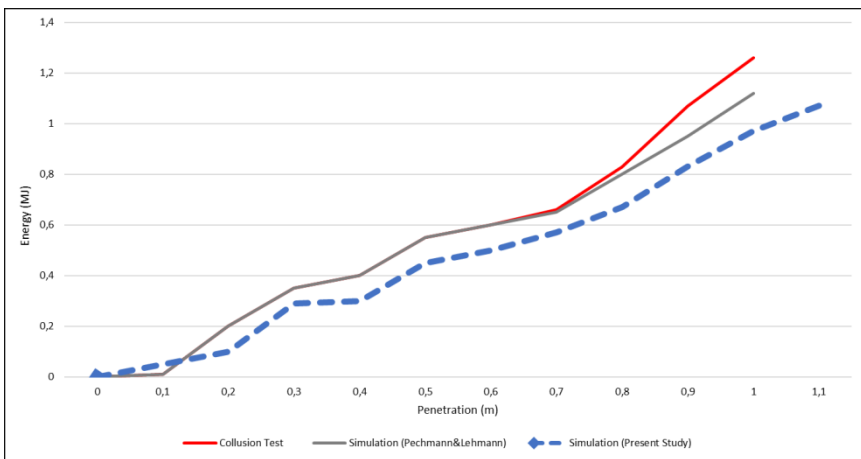
Fig. 5: Measuring the energy (MJ) and penetration depth (m) during the crash test and comparing the results obtained in the analyzes of the software LS-DYNA
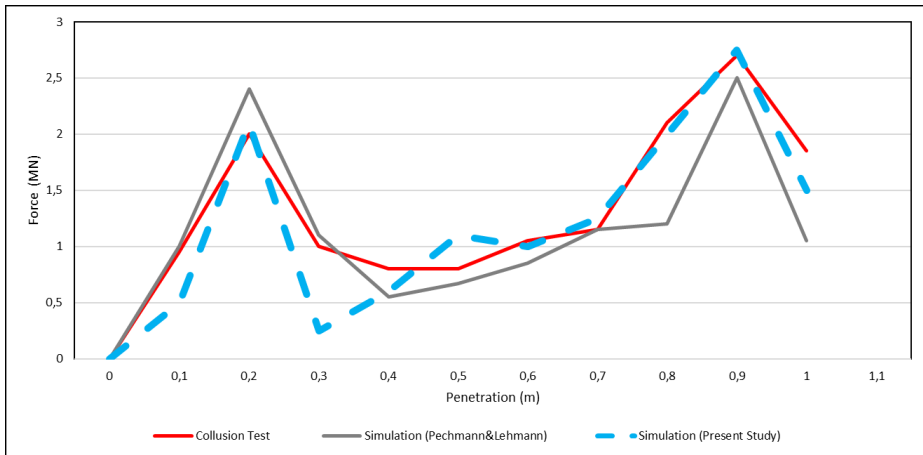
Fig. 6: Measuring the force (MN) and penetration depth (m) during the crash test and comparing the results obtained in the analyzes of the software LS-DYNA

It is seen that the results of the crash test performed by Lehmann and Peschmann (2001) are quite compatible with the results of the LS-DYNA analysis (Figures 5 and 6). In the analyzes carried out within the scope of this study, it was determined that the force (MN) and energy values (MJ) as well the penetration depth values measured in the crash test agree with the results of the analysis performed under the same conditions (Figures 5 and 6).

1.2 ASIS (1993)-Verification of Free Fall Test

Another experiment that is the subject of this study is the deformation test performed by ASIS in 1993, which was performed as a result of the impact of a free-fall bow against a simple construction as seen in Figures 7 and 8. Figure 9 exhibits the results of the test and the analyses that were carried out by Paik (2010).
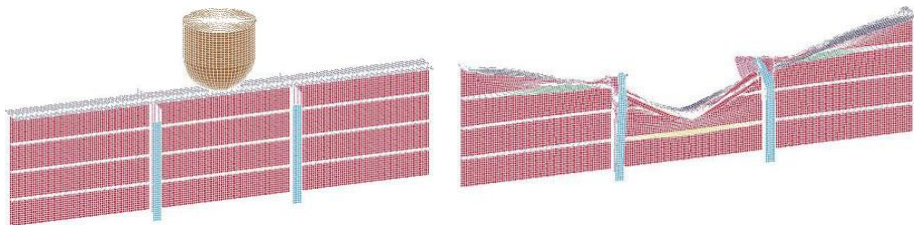
Fig: 7 a. Before Test   b. After Test (Paik, 2010)
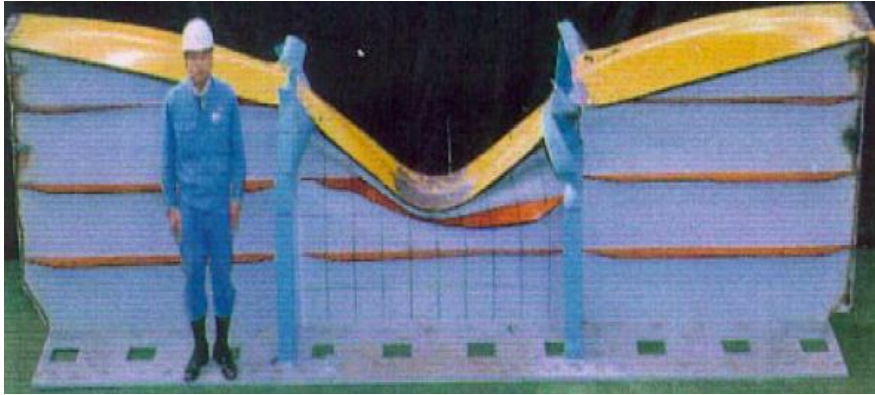
Fig. 8: Deformation experiment (Paik, 2010)

To verify the results of the ASIS test in this study, numerical analyzes of this Experiment and Model-I, Model-II as well Model-III were simulated for different plate thicknesses. The force and energy values obtained were given in Figure 10, where the dimensions of the bow and construction model as well as the plate and profile thicknesses are given in Table 2.
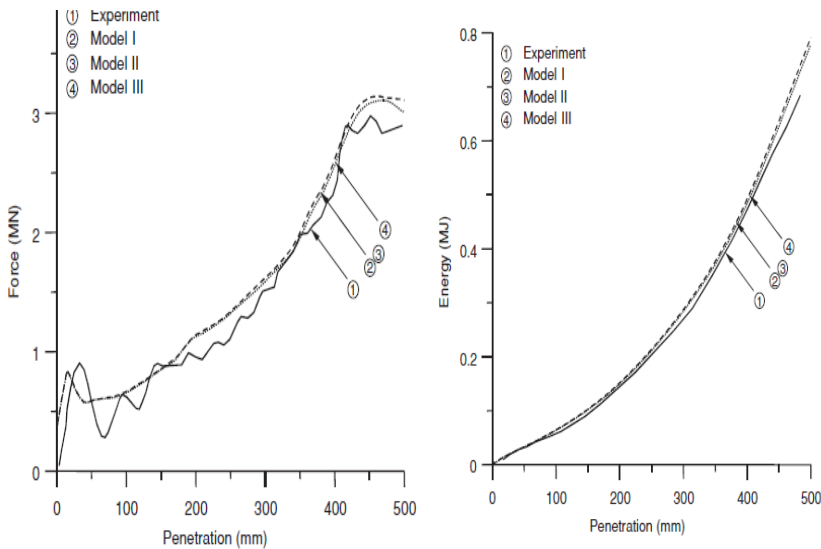
Fig. 9: ASIS a) Force-Penetration Variation b) Energy-Penetration Variation (Paik, 2010)

Table 2. ASIS Test data

Deck Height	(H_w)	1635.0 mm
Overall Lengh	(L)	6000.0 mm
Web Spacing	(2b)	2000.0 mm
Width of side plating	(2a)	450.0 mm
Side Plating Thickness	(t_p)	10.0 mm
Stiffener Thickness	(t_s)	8.0 mm

According to the data in Table 2, the construction plate model was created and the free fall of the bow onto the construction was analyzed. Examining the results obtained also in this study, it becomes clear that the results of the test and the analyses are in perfect agreement as seen in Figures 10 and 11.
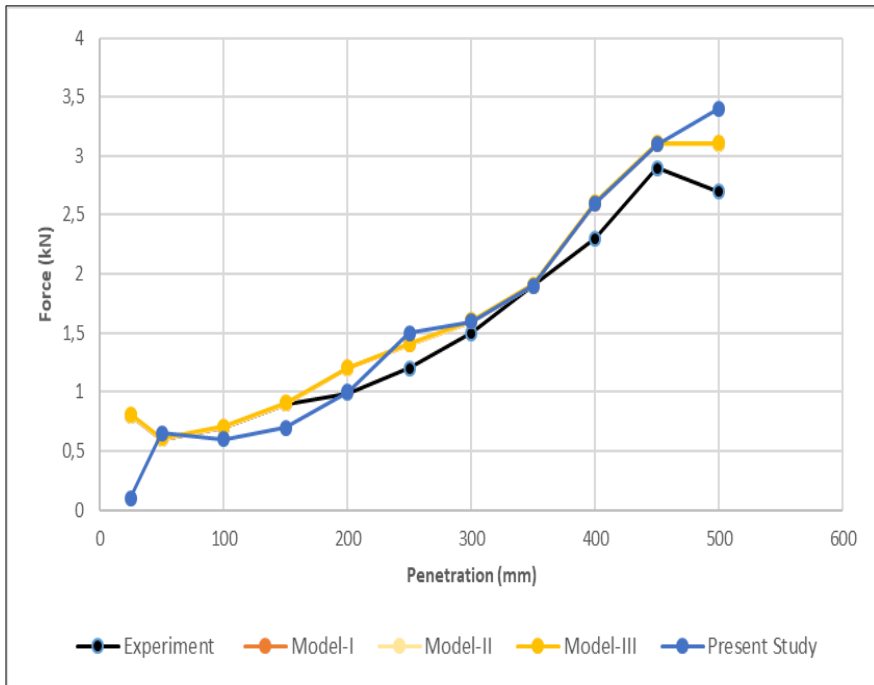
Fig. 10: Strength and penetration depth obtained from tests and analyzes
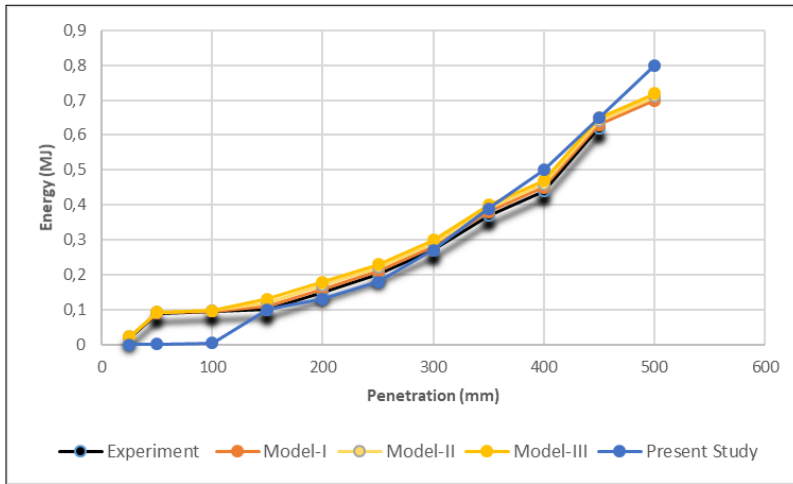
Fig. 11: Absorbed energy and penetration depth from tests and analyzes

2. ANALYSIS OF THE COLLISIONS

Plates, stringers and stiffeners constitute the basic construction elements that provide strength in ship constructions. The height of the moments of inertia of the stiffened plates in planes perpendicular to the impact direction increases the strength capability of the construction against impacting objects. Another very important issue in this type of steel constructions is the welding process of plates and stiffeners. In this study, it was assumed that the welding methods and processes were carried out failure free and the strength value of the welding seams in the collision zone was above the strength values of the plates and stringers as well stiffeners.

The impact of the ship crashing perpendicular to the side of another tanker and thus the reduction of the impact surface is very effective in the occurrence of environmental disaster after the collision. The plate and stiffener thicknesses of the crashed ship, the closeness of the stiffeners used, that is, the average moment of inertia value of the crashed area and the quality of the material determine the effect area of the accident. Consequently, since the most dangerous collision is induced when a ship collides perpendicularly with the side of another ship, analysis of this type of impact is usually conducted.

Potential collision situations that may occur at ships are examined in detail by Liu and Villavicencio (2020). The collisions are scaled according to their severity as "lightly damaged" and "heavily damaged" and the percentage of 50% and 90% were assigned to minor "lightly damaged" and major "heavily damaged" accidents, respectively. In these analyses, apart from the

ship grounding, the cases where the bow of a ship with or without a bulbous collides the ship's side with severe damage (90%) were investigated (Fig. 12 and 13).
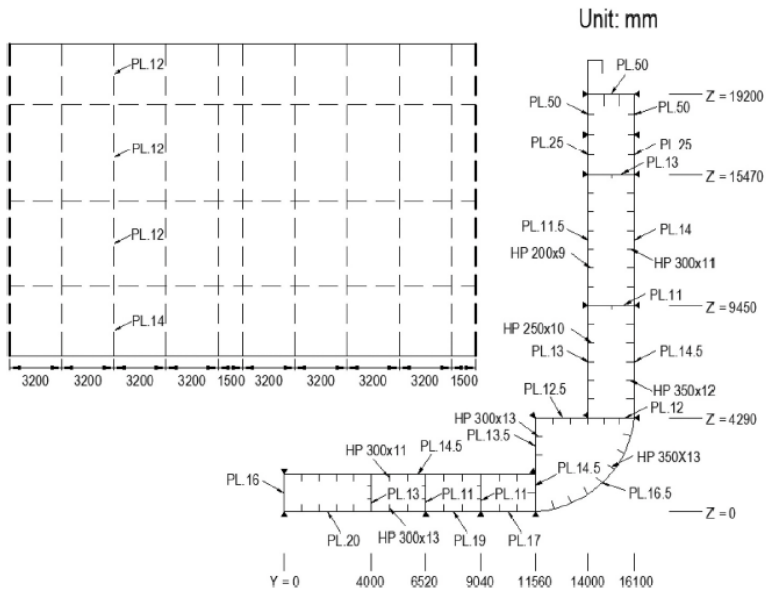
Fig. 12: Model of the ship hull section analyzed (Liu and Villavicencio, 2020)
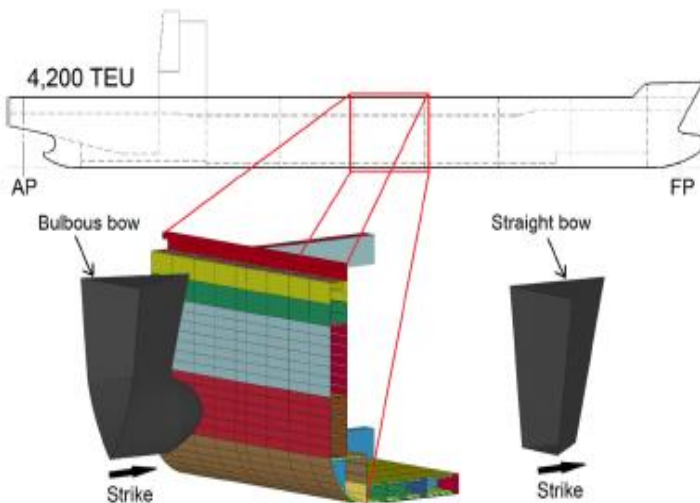
Fig. 13: A bulbous bow and straight bow ship colliding with the side of another ship (Liu and Villavicencio, 2020)

In this study, the models of the bow and construction were created, and mesh structures were generated in the software LS-DYNA (Fig. 14-17). As seen in Fig 15 and 16, a) Standard VLCC and c) Stringer type constructions were modeled. As the boundary conditions, the impacted ship's side was fixed on both sides as clamped, and the initial velocity and mass per node were defined. AH36 steel was selected by accepting the material as having linear elastic-plastic properties (Fig. 17).
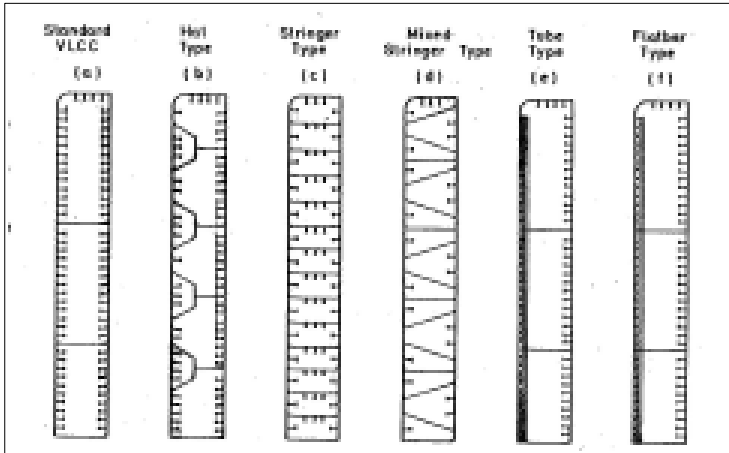
Fig. 14: Ship Structures (Tørnqvist, R. 2003)
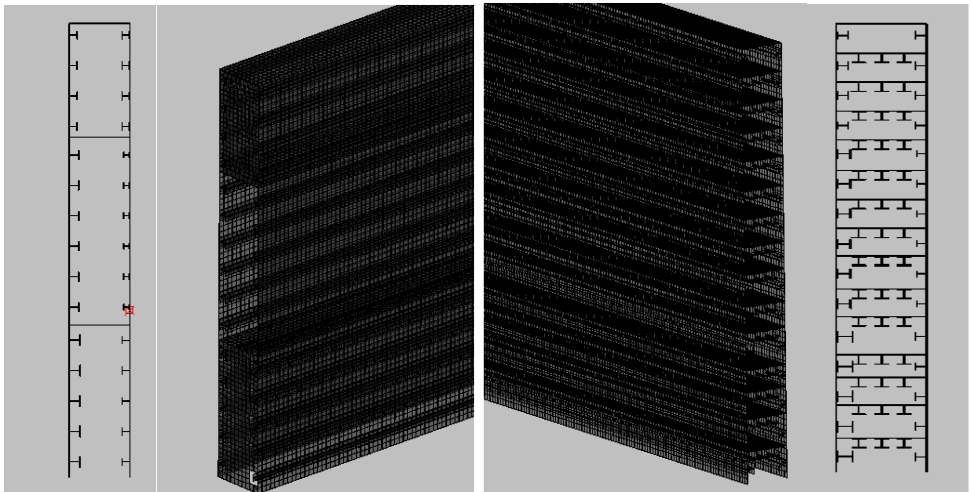
Fig. 15: Selected standard VLCC (a)   **Fig. 16:** Selected stringer type (c)

Gürsel and Nane (2010) simulated crash scenarios of an automobile in their study and showed that the amount of energy to be absorbed during the collision increases in direct proportion with the thickness of the profile placed inside the door. Based on this study, in the following stages of the analysis, plate and stringer thicknesses of the model in Liu and Villavicencio (2020) were increased by 15% and 30% in two stages in order to increase the strength of the double-walled tanker construction against collisions by means of absorbing more energy (Fig. 17 and 18). In these analyses, as in the previous analyses, the mesh structure, contact type and friction coefficients were taken as the same. One of the most important parameters in the analysis is the bow model (Fig. 18). This element must be rigidly processed and standardized. Although there is no rule about how the collision should be, perpendicular collisions to the side of another ship, which will cause the most dangerous accident, were considered, and analyzed (Figure 13).
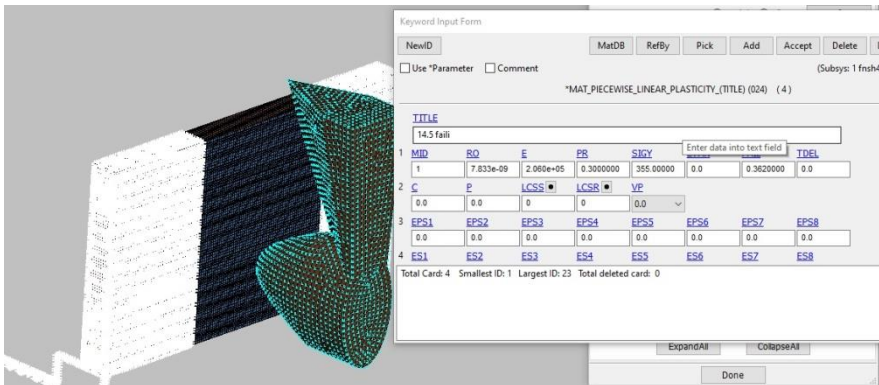
Fig. 17: Boundary and material conditions

It was determined that the absorbed energy increased slightly when the plate and stringer thicknesses were increased by 30%. However, the absorbed energy changed barely if the plate and stringer thicknesses were increased by 15% as seen in Figure 19 and 20. Therefore, it was concluded that a ship construction that shall be more resistant to collision should be planned in detail at the preliminary design stage.

Therefore, double-walled constructions of a tanker and/or a container ship with stringer+plates and only plates were generated, respectively (Fig. 18). Furthermore, a hypothetic case was arranged that the thicknesses of the double-walled construction plates without stringer on side walls was reinforced about 30%. These three different cases were modelled and analyzed. The results obtained were given in Fig. 19 and 20.

CONSTRUCTION MODELS and ANALYSES		
Standard VLCC (Present Study)	**Std. VLCC Reinforced+15%Thck.**	**Std. VLCC Reinforced+30%Thck.**
Stringer Type	**Stringer Type Only Plates**	**Stringer Type with reinforcement**
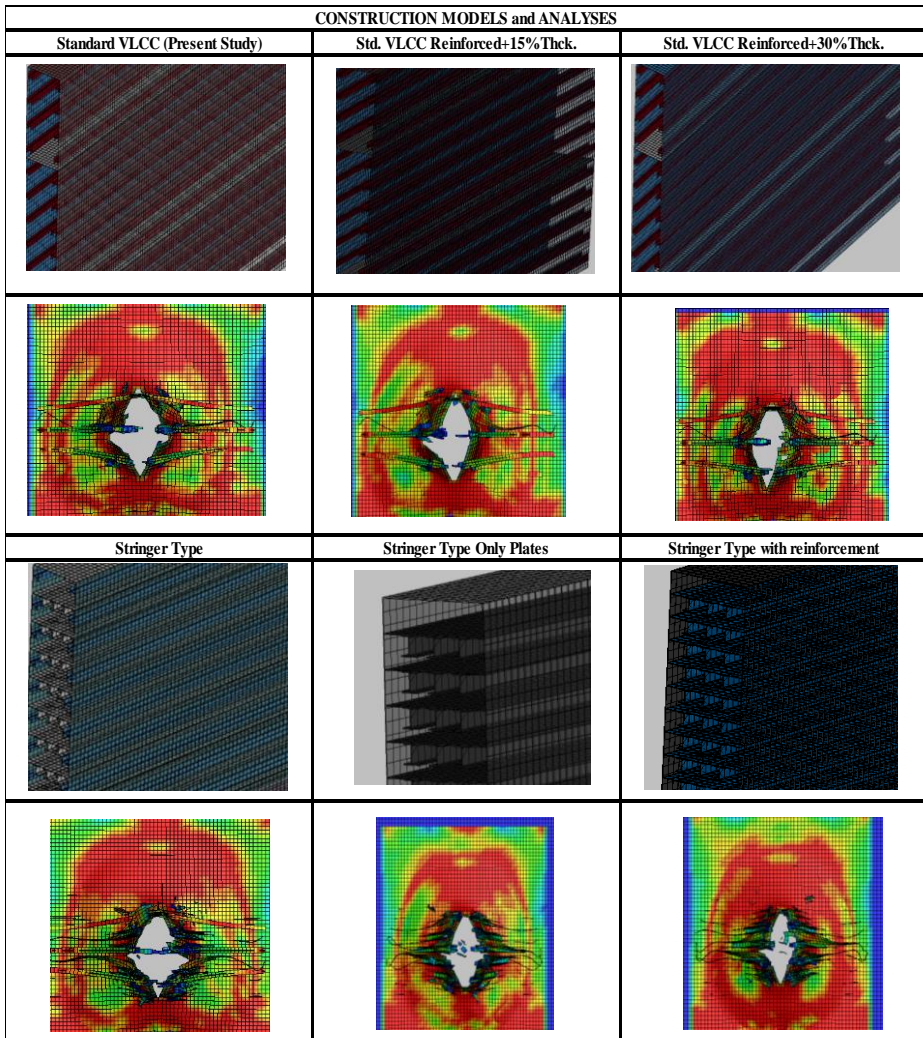
Fig. 18: Standard VLCC and stringer type construction models and analyses

While the forces and energy absorbed during collision of the ships achieved magnitudes of 100 MN and 165 MJ by means of the double wall constructions with stringer+plates, respectively; in double wall constructions with only plates, collision forces and absorbed energy ranged from 120 MN and 200 MJ, respectively. The double wall construction with only plates that were reinforced about 30% was proved itself as the best one, because it absorbed forces and energy in height of 150 MN and 275 MJ, respectively.
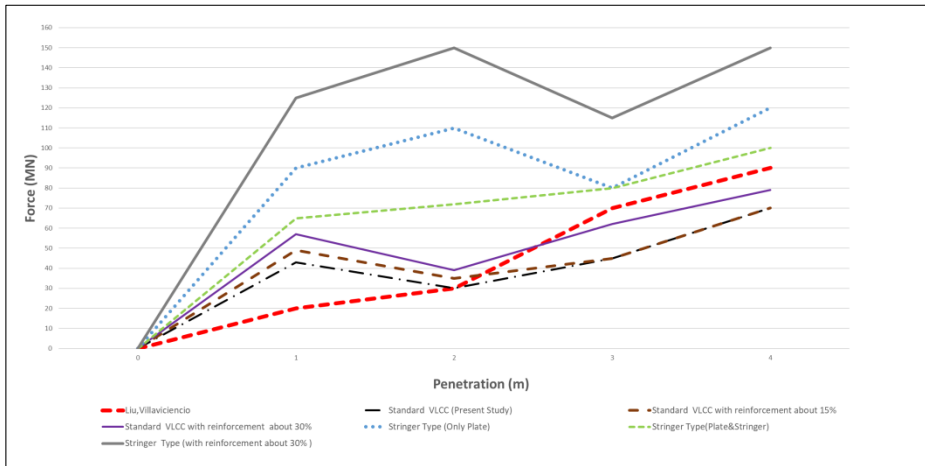
Fig. 19: The force and the penetration values during the collision
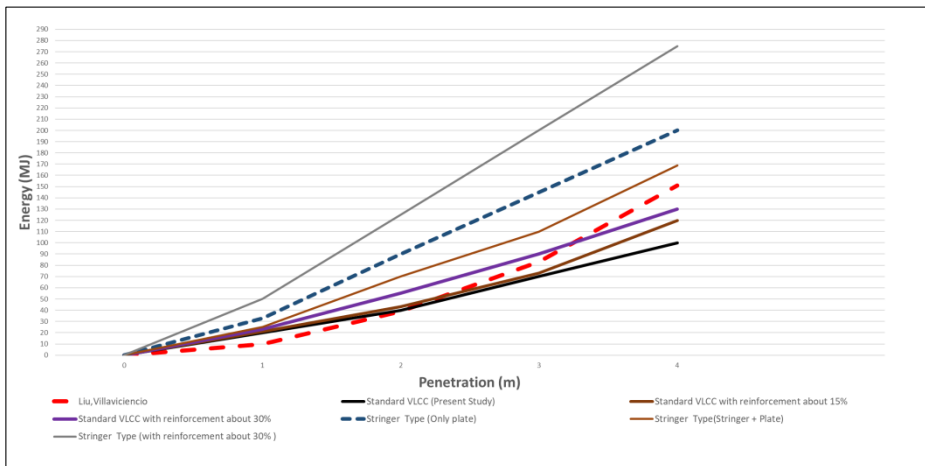
Fig. 20: Magnitudes of the energy absorbed and the penetration generated during the collision

CONCLUSION

In this study, after the test data of the ship collisions had been obtained from the literature, the test setups were modeled and then the results of the analysis obtained in the simulations were verified with these test data. The collision simulations of the ship models were carried out using the software "ANSYS/LS-DYNA".

In the analyses, a scenario in which collisions and impacts intensified was determined and collisions with shipboards of different constructions were simulated.

In the last stage, the analyzes of the more durable constructions created by increasing the plate and stringer thicknesses by 15% and 30%, were performed. It was determined that the absorbed energy increased to a limited extent when the plate thicknesses increased by 30%. While increasing the plate and stringer thicknesses by 15%, the absorbed energy barely changed.

Therefore, it has been concluded that a ship construction that is more resistant to collisions should be handled and examined in much more detail during the preliminary design phase.

Furthermore, double-walled constructions of a tanker and/or a container ship with stringer+plates, only plates and only plates reinforced about 30% were generated. These three different cases were modelled and analyzed. It was determined that the doublewalled construction with only 30% reinforced plates, the hypothetical case, was the best one as expected, while the ship construction with stringer+plates absorbed insufficient energy during collision. In spite of this effective reinforced construction, it is possible that the energy created during the collision could cause that the bulbous bow of the crashing ship penetrates the inner plates of the other ship.

Hence, all in this sector must realize that the hulls of the ships can always be injured by the bulbous bows although they can be stiff and shielded as vessels with armored guarding. Therefore, the phase should finally be started that not only crashed ships but also the impacting ships have to be taken into consideration elaborately.

REFERENCES

Gürsel, K. T., Nane, S. N. (2010). Non-linear finite element analyses of automobiles and their elements in crashes. International journal of crashworthiness, 15(6), 667-692.

Lehmann, E., Peschmann, J. (2002). Energy absorption by the steel structure of ships in the event of collisions. Marine Structures, 15(4-5), 429-441.

Liu, B., Villavicencio, R., Pedersen, P. T., & Soares, C. G. (2021). Analysis of structural crashworthiness of double-hull ships in collision and grounding. Marine Structures, 76, 102898.

Onay, M. G., Pehlivanoglu-Mantas, E., & Martins, F. (2020). Oil spill modeling in East Mediterranean. Journal of the Faculty of Engineering and Architecture of Gazi University, 35(4), 1737-1750.

Paik, J. K. (2007). Practical techniques for finite element modelling to simulate structural crashworthiness in ship collisions and grounding (Part II: Verification). Ships and Offshore Structures, 2(1), 81-85.

Tørnqvist, R. (2003). Design of crashworthy ship strucures. Technical University of Denmark.

CHAPTER 2

ADVANCEMENTS IN TECHNOLOGY AND MATERIALS FOR DIRECT AIR CAPTURE: A COMPREHENSIVE OVERVIEW

Mech. Eng. Cemile KAYIŞ[1]

Assoc. Prof. Dr. Ege Anıl DİLER[2]

[1] Ege University, Graduate School of Natural and Applied Sciences, Mechanical Engineering, Izmir, Turkey, cemilekayis@hotmail.com, ORCID: 0000-0002-4401-2412
[2] Ege University, Faculty of Engineering, Department of Mechanical Engineering, Izmir, Turkey ege.anil.diler@ege.edu.tr, ORCID: 0000-0002-1667-5737

INTRODUCTION

Greenhouse gas levels in the atmosphere of the world have increased at a rate that is unprecedented in the nearly 200-year period from the Industrial Revolution to the present. Greenhouse gases act as a blanket in the atmosphere, limiting the reflection of sunlight and providing the essential heat for life on Earth. Common greenhouse gases include chlorofluorocarbons (CFC), hydrofluorocarbons (HFC), carbon dioxide (CO_2), methane (CH_4), ozone (O_3), and water vapor. Calculations reveal that if greenhouse gasses were not present in our atmosphere, the earth's temperature would be around -18˚C (Yoro and Daramola, 2020). However, the massive increase in the rate of these gases observed today has resulted in an unnatural rise in earth temperatures, leading to global warming.

In today's context, many distinct types of greenhouse gases are released into the atmosphere by humans. Figure 1 (a) shows the percentage shares of each gas in the total greenhouse gases released in 2021. CO_2 appears here as the gas with the highest emission rate. However, in addition to the amount of emissions, the extent to which greenhouse gases contribute to global warming depends on two characteristics: their energy retention capacity and their residence time in the atmosphere. It is known that methane, the second most released gas, has the capacity to absorb 25 times more energy than CO_2. However, since methane combines with hydroxyl radicals in the troposphere, it only has a decade of life in the atmosphere. On the other hand, the lifespan of CO_2 in the atmosphere is measured in centuries. The energy absorption capability of N_2O gas, which has another high percentage, is determined to be 300 times that of CO_2, and its residence time in the atmosphere is around 125 years (Behbahani and Green, 2023).

The energy absorption capacity of fluorinated gases, which is the group with the lowest emission rate in the chart in Figure 1 (a), is 20.000 times greater than that of CO_2 and they, like CO_2, can remain in the atmosphere for centuries (Behbahani and Green, 2023). Since it was discovered that CFCs, which were widely used in the 1980s, caused significant damage to the ozone layer, their use was severely restricted by the Montreal Protocol, which was signed in 1987. CFC emissions decreased rapidly in the years following the protocol's signing due to the rapid development of an alternative material

group that can replace CFCs (Figure 1 (b)), thus preventing the major contributions of these gases to global warming (Rigby et al., 2013).

(a)

(b)
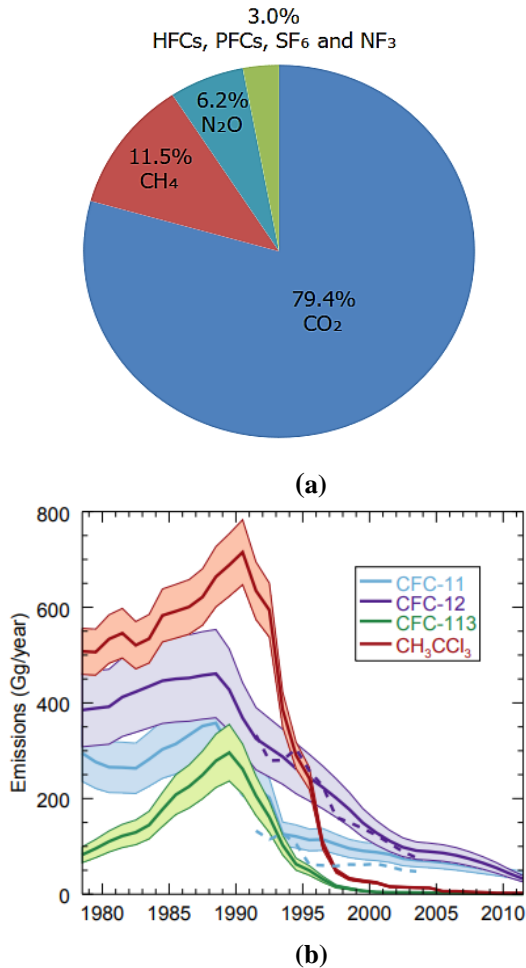
Figure 1: (a) Emission Percentages of Greenhouse Gases in 2021 (www.epa.gov/ghgemissions/overview-greenhouse-gases) and **(b)** CFC Emissions among Years (Rigby et al., 2013)

The current increase in CO_2 emissions, and thus its rate in the atmosphere, is comparable to the increase in CFCs observed in the 1980s. However, CO_2 is not a greenhouse gas that can be easily reduced, particularly because it is emitted by fossil fuel sources, which are still widely used for electricity generation and transportation fuels, and the renewable energy technologies that can replace them are relatively expensive. Figure 2 (a) illustrates the change in CO_2 concentration in the atmosphere from 800 years

ago to the present, based on technical calculations. Given the slope of the graph between the 1900s and today, it is clear that such a rapid increase has not occurred in human history. CO_2 concentration data recorded with technological devices since 1958 are shown in Figure 2 (b).
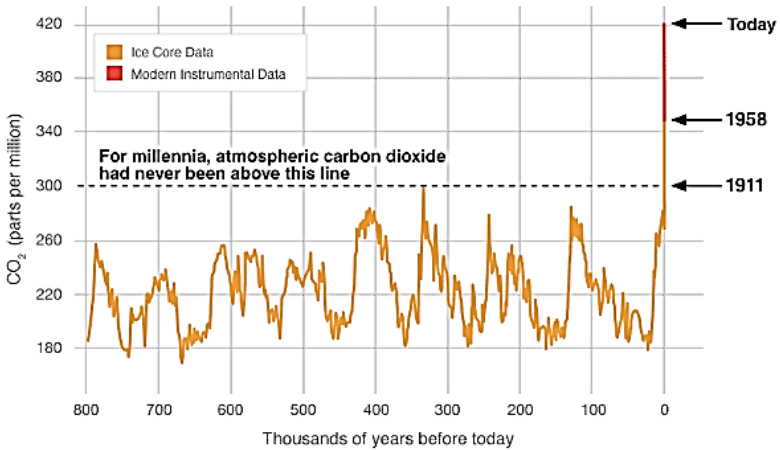
(a)
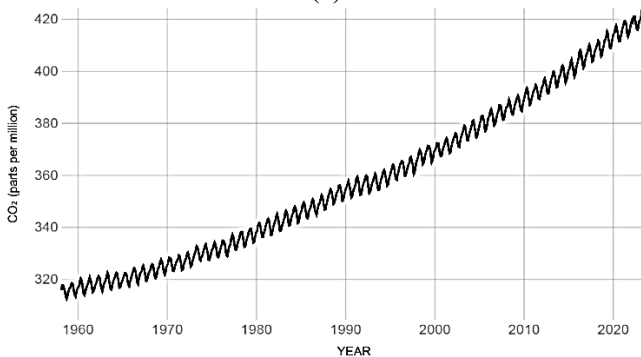
(b)

Figure 2: (a) CO_2 Concentration in the Atmosphere from 800 Years Ago to the Present, Mostly Based on Technical Calculations and **(b)** Extended CO_2 Concentration for Recent History Based on Instrument Data (https://climate.nasa.gov/vital-signs/carbon-dioxide/)

Figure 3 (a) shows the global temperature anomaly graph for the period from the 1880s when observation records began to be kept in the world, to the present day. Despite the variability in annual average temperatures shown in grey in the graph, it can be observed that the temperature change shown in black is in an increasing trend when evaluated for many years. Global temperatures have consistently been in a positive anomaly, particularly from the 1980s to the present. When Figure 3 (a) and Figure 2 (b) are interpreted

together, it is clear that the slopes of the increase curves of CO_2 concentration in the atmosphere and global temperature anomaly since the 1960s are in accordance. In this case, given the previously stated reasons, it appears as an undeniable fact that CO_2 emissions directly and very effectively cause global warming.
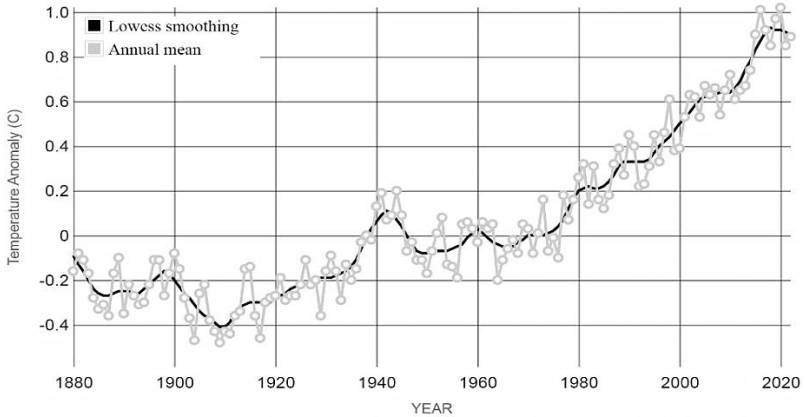
(a)
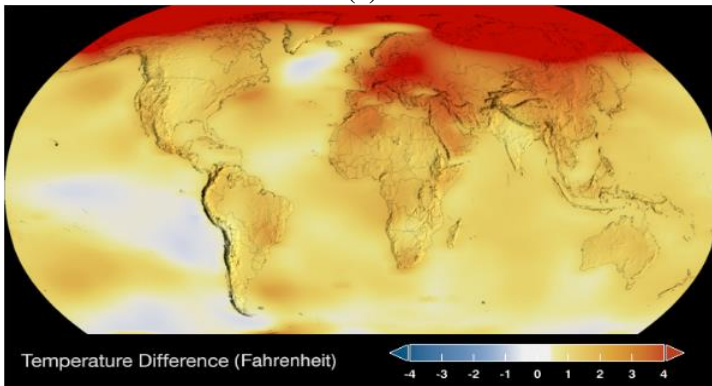
(b)

Figure 3: (a) Global Temperature Anomaly Chart from 1884 to 2022 and **(b)** Change in Global Surface Temperature in 2022 Compared to 1884 (https://climate.nasa.gov/vital-signs/global-temperature/)

Figure 3 (b) shows the changes in global surface temperatures from 1884 to 2022. The average warming in the lithosphere is 2˚F (1.1˚C) or higher, and in some regions, this warming has reached 4˚F (2.2˚C). The Paris Agreement, signed in 2015, was designed to set safe limits on this issue, stating that the global average temperature increase should be limited to a maximum of 2˚C compared to the pre-industrialization level. In this context, although there is no direct limit on the amount of gas released in the Paris

Agreement, as there is in the Montreal Protocol, calculations based on IPCC scenarios have revealed that 30 Gt CO_2 must be removed from the atmosphere every year to prevent a warming of more than 2˚C (Ozkan et al., 2022).

As a result of all of these circumstances, CO_2 capture technologies are becoming an increasingly popular research topic. These developed technologies are generally classified according to the stage at which they perform the capture process to be better examined. Figure 4 illustrates a diagram of these technologies, which can be divided into four categories. Technologies that capture CO_2 at the use stage aim to reduce emissions of greenhouse gases from the source. These are categorized as post-combustion capture, oxy-combustion capture, and pre-combustion capture, respectively, in Figure 4.
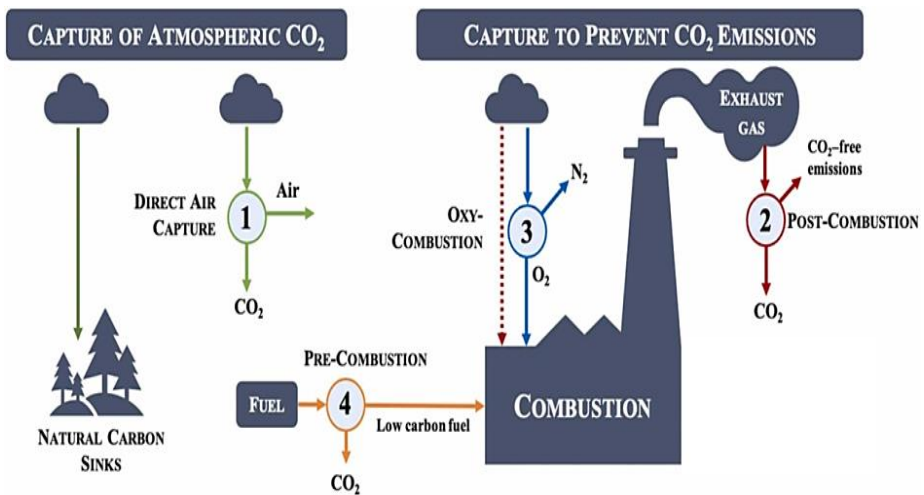
Figure 4: CO_2 Capture Technologies (Garcia et al., 2022)

Pre-combustion capture technologies seek to reduce CO_2 emissions by decarbonizing the carbon-based fuel used in energy production via a variety of processes. The conversion of methane into hydrogen fuel is the best example of this.

- $CH_4+H_2O \rightarrow CO+3H_2$ (1)

- $2CH_4+O_2 \rightarrow 2CO+4H_2$ (2)

- $O+H_2O \rightarrow CO_2+H_2$ (3)

While the reaction is endothermic when methane is converted using water vapour, as in reaction 1, it can be exothermic when oxidation is performed, as in reaction 2. Today, a combination of the two processes is used in industrial applications for cost optimization. The aim is to produce more efficient hydrogen fuel by re-reacting the carbon monoxide released as a by-product in both reactions (Garcia et al., 2022). The third reaction is critical for CO_2 utilization technologies. Electrochemical reactions have the potential to convert CO_2 to CO. This has raised the question of whether the captured CO_2 can be used to produce clean hydrogen fuel after being converted to CO. This issue is presently taking the place of an idea that researchers are working on. However, as previously stated, because it changes the fuel used, pre-combustion technology necessitates a redesign of production facilities to accommodate this new situation. As a result, while it is a promising technology for new facilities, it is not feasible to completely transform existing facilities due to high costs.

Post-combustion technologies capture CO_2 from flue gases released after combustion. As a result, this technology is regarded as the most appropriate method for reducing emissions in production facilities that may be considered old. It is the most widely used method in industrial applications today. The fact that flue gases contain other mixtures such as NO_x, SO_x, and fly ash, as well as being at very high temperatures, are among the factors that make the method difficult to apply and increase separation costs (Garcia et al., 2022). Many different methods have been developed that can be used in the post-combustion stage to overcome all of these conditions. Chemical absorption with a liquid solvent, physical or chemical adsorption on a solid surface, membrane filtration, cryogenic decomposition, and microbial methods are examples of post-combustion technologies (Fu et al., 2022).

The principle of Oxy-combustion technology is to burn the fuel during production with pure O_2 rather than free air. Changes to the flue gas content can thus be made without changing the fuel type. While standard flue gas contains 71.5% N_2, 19% H_2O, and 9.5% CO_2, oxygen-burned fuel contains 60% CO_2 and 40% H_2O. Although the CO_2 rate appears to have increased in this case, the absence of N_2 gas produced at a high rate by the standard combustion process in the flue gas content to be captured using post-combustion technology allows for a significant increase in CO_2 selectivity (Garcia et al., 2022).

So far, the capture technologies described have been designed specifically for manufacturing facilities and function to reduce or eliminate the emissions gases released by those facilities. However, even if the zero-emission target is met in this manner, it is assumed that it can be met by 2050 according to the most optimistic scenario, given that the atmospheric life of CO_2 is measured in centuries, it is understood that our existing forest ecosystem can reduce CO_2 in the atmosphere to normal levels within a few centuries at best. The concept of DAC technology appeared as a solution to this impasse. It is possible to capture CO_2 that has already been released into the atmosphere using this technology. In this sense, DAC can be considered as an approach that artificially achieves the CO_2 reduction that the forest ecosystem achieves naturally, without producing a by-product as photosynthesis does. If more CO_2 is removed from the atmosphere in a year than is released, the pre-industrial atmosphere can be reached without exceeding the Paris Agreement's 2°C warming limit. The following sections provide more in-depth explanations of the technology.

1. DIRECT AIR CAPTURE (DAC) TECHNOLOGY

Direct Air Capture (DAC) is the process of removing CO_2 from the atmosphere. Although the process differs depending on the method used, it essentially consists of two stages: CO_2 capture by the sorbent and sorbent regeneration. Figure 5, shows the capture mechanism to provide a general representation. Firstly, fans are used to blow atmospheric air into the process room. The CO_2 in it is absorbed by the sorbent there, and the clean air is released back into the atmosphere through the process room exit. The process is carried out until the sorbent is saturated with CO_2. The process room's fans

and outlet are then turned off, and the regeneration stage begins. At this point, the sorbent is heated to desorb CO_2, and the separated CO_2 is pumped to a storage location via a piping system. Critical values such as the complexity of the equipment used in these processes, the size of the process rooms, the regeneration temperature, and the energy spent per ton of CO_2 captured vary depending on the type of sorbent used (Temmerman and Rochette, 2023) . Direct Air Capture (DAC) is the process of removing CO_2 from the atmosphere. Although the process differs depending on the method used, it essentially consists of two stages: CO_2 capture by the sorbent and sorbent regeneration. Figure 5, shows the capture mechanism to provide a general representation.

Firstly, fans are used to blow atmospheric air into the process room. The CO_2 in it is absorbed by the sorbent there, and the clean air is released back into the atmosphere through the process room exit. The process is carried out until the sorbent is saturated with CO_2. The process room's fans and outlets are then turned off, and the regeneration stage begins. At this point, the sorbent is heated to desorb CO_2, and the separated CO_2 is pumped to a storage location via a piping system. Critical values such as the complexity of the equipment used in these processes, the size of the process rooms, the regeneration temperature, and the energy spent per ton of CO_2 captured vary depending on the type of sorbent used (Temmerman and Rochette, 2023).
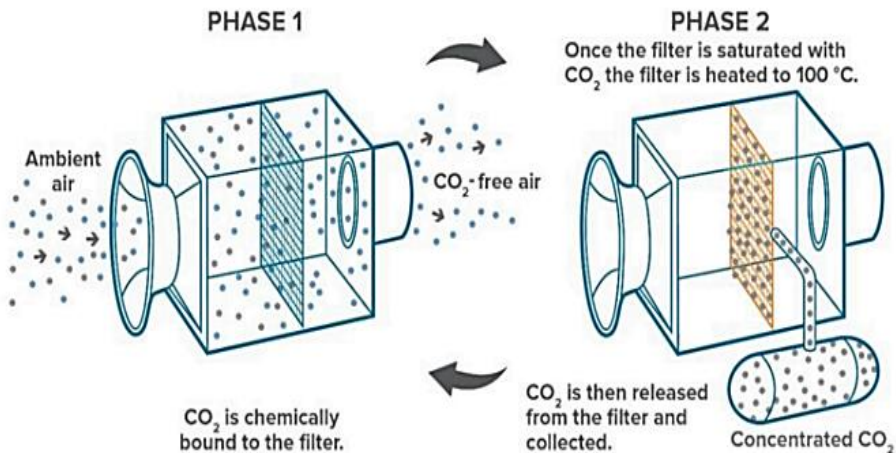
Figure 5: A Representative DAC Process (Beuttler et al., 2019)

Many different materials have been developed for use in DAC technology. Although it varies depending on the material, the process costs are too high to be compared to the costs of any industrial application because it is a new technology. Understanding how each item in the process contributes to the total cost and how these items change with material change serves as a guide to see which areas can be focused on to contribute to the development of DAC technology. The various materials used were divided into two major groups (liquid sorbents and solid sorbents), which are used differently by the two companies that dominate the sector, and the energies spent and costs incurred in the stages of the DAC process were analyzed.

	Liquid DAC/heat	Liquid DAC/electricity	Solid DAC/heat	Solid DAC/electricity
Low	5.25	1.32	2.9	0.6
High	8.1	1.8	5.5	1.1
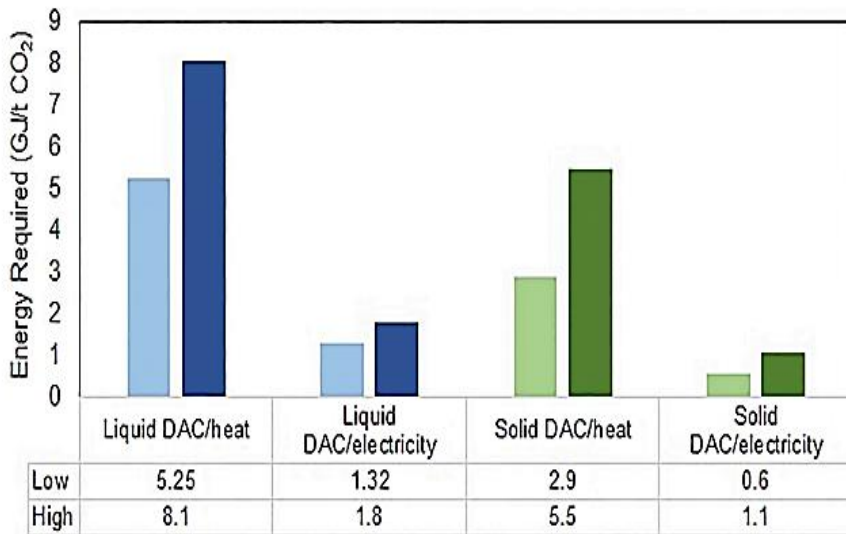
Figure 5: Energy Requirements for Solid and Liquid Sorbent DAC Systems (Ozkan et al., 2022)

The first thing to notice about the energy requirements of the systems shown in Figure 6 is that they are expressed in GJ order. As was noted in the Introduction section, considering the need to remove 30 Gt CO_2 from the atmosphere each year to stay within the maximum warming target of 2˚C, the energy required for DAC will be 1.97×10^{20} J. This value can be made more meaningful by using the following example: The United States used 0.98×10^{20} J of energy in 2020 as a country. DAC requires twice this value (Ozkan et al., 2022). In such a case, setting up a DAC system capable of capturing 30 Gt of CO_2 per year would be irrational. Because the resources used to generate this

energy also emit CO_2 into the atmosphere. Although this value is lower than that of other sources in renewable energy systems, it is not non-existent. Table 1 shows the amount of CO_2 released into the atmosphere per year based on the various energy sources used for supplying the electrical energy required for running fans, etc. systems in DAC processes using liquid and solid sorbents, as well as the heat energy used in the regeneration stage.

Consider in Table 1 DAC systems with liquid and solid sorbents that use solar sources for electrical energy and natural gas sources for heat energy to make an equivalent comparison. While the CO_2 produced by the liquid sorbent system as a result of the heat energy used ranges between 0.47 Mt/year and 0.66 Mt/year, the solid sorbent system produces between 0.22 Mt/year and 0.30 Mt/year. It should be noted that these values are parallel to the values in the energy graph shown in Figure 6; whereas the energy required for heat by the liquid sorbent system ranges from 5.25 GJ/t to 8.1 GJ/t, the solid sorbent system ranges from 2.9 GJ/t to 5.5 GJ. As a result, it would be an appropriate assessment to conclude that systems using solid sorbents, which require less energy, emit less CO_2. This energy difference is mainly originated by the regeneration temperature. While the regeneration temperatures of solid sorbents vary between 80-120˚C, this temperature reaches 900˚C for liquid sorbents (Temmerman and Rochette, 2023).

Table 1: Amounts of CO_2 Generated by the DAC System Depending on the Sorbent Material and Energy Source (Ozkan et al., 2022).

Sorbent	Electricity	Heat	Carbon generated from heat (MtCO$_2$/year)	Carbon generated from electricity (MtCO$_2$/year)
Liquid	Solar	Natural Gas	0.47–0.66	0.01–0.03
Liquid	Wind	Natural Gas	0.47–0.66	0.004–0.009
Liquid	Nuclear	Natural Gas	0.47–0.66	0.01–0.02
Liquid	Natural Gas	Natural Gas	0.47–0.66	0.11–0.23
Liquid	Coal	Natural Gas	0.47–0.66	0.18–0.38
Solid	Solar	Solar	0.008–0.01	0.0004–0.008
Solid	Nuclear	Nuclear	0.004–0.005	0.002–0.004
Solid	Solar	Natural Gas	0.22–0.30	0.0004–0.008
Solid	Wind	Natural Gas	0.22–0.30	0.002–0.003
Solid	Natural Gas	Natural Gas	0.22–0.30	0.07–0.14
Solid	Coal	Coal	0.32–0.44	0.15–0.3
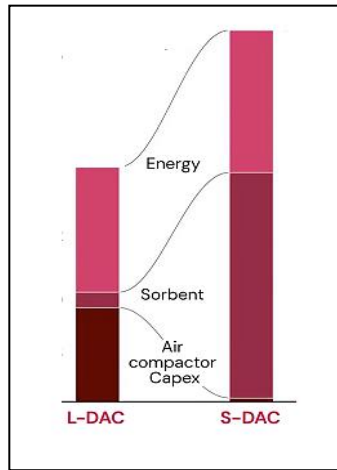
Figure 6: The Key Components Affecting the Cost of Liquid and Solid Sorbent DAC Systems (Temmerman and Rochette, 2023).

When heat and electrical energies are considered together, the required energy range for liquid sorbents is between 6.57 GJ/t and 9.9 GJ/t, while for solid sorbents this range is between 3.5 GJ/t and 6.6 GJ/t. Moving to the cost side that corresponds with these values, it is possible to arrive at the opinion that liquid sorbent systems necessitate higher costs per ton captured. The reality, however, is quite the opposite. ClimeWork, which uses solid sorbents, and Carbon Engineering, which uses liquid sorbents, have cost statements of $600/tCO$_2$ and $94-232/tCO$_2$, respectively (Ozkan et al., 2022). The reason for this contrast is visualized in Figure 7. Sorbent costs have surpassed almost all other items in systems with solid sorbents. Because these adsorbents reach saturation by capturing less CO$_2$ per cycle than liquid sorbents, they are subjected to more regeneration processes per unit of time. Following each regeneration process, both sorbents' CO$_2$ capture capacity and sorbent efficiency decrease. As a result, the material life of solid sorbents that is shorter. Because this increases material consumption, it becomes the most cost-prohibitive unit among cost items.

Aside from the sorbent cost, research is continuing to develop materials with higher CO$_2$ capture capacity and less wear through regeneration for DAC technologies with solid sorbents, which are more advantageous in terms of energy use, CO$_2$ emissions, system component costs, and so on.

2. MATERIALS FOR DIRECT AIR CAPTURE

The circumstance that the CO_2 expected to be removed from atmospheric air is quite dilute in the air mixture, 420 ppm (0.04%), increasing the amount of energy required in the capture process. As a result, it is critical to identify and develop materials for DAC processes with high CO_2 selectivity and sorption capacity. CO_2 capture is carried out predominantly through two mechanisms: absorption and adsorption. Sorbate (CO_2) is absorbed volumetrically in the sorbent during absorption, whereas it adheres to the surface during the adsorption. Although both mechanisms can be observed in both solids and liquids, absorption is known to occur in most liquid sorbents and adsorption is known to occur in most solid sorbents (Zanatta, 2023).
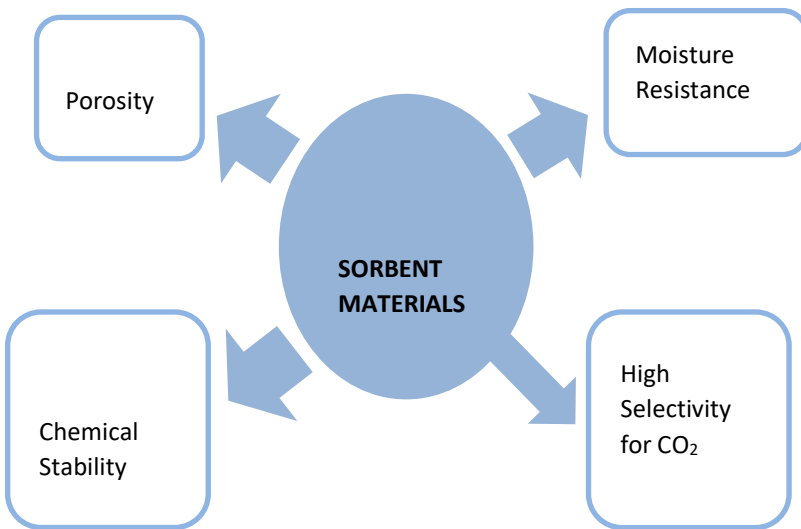
Figure 7: Important Properties of Sorbent Materials for DAC Conditions

Adsorption in solid sorbents can occur in two ways: physical and chemical. Chemical adsorption occurs when chemical bonds are formed between the sorbent surface and the sorbate through electron exchange; physical adsorption occurs when the sorbate adheres to the surface through structures such as Van der Walls bonds, electrostatic forces, and hydrogen bonds. Adsorption is an exothermic phenomenon. The magnitude of the heat released during adsorption determines the strength of the bond between the

sorbate and the sorbent. Since chemical bonds are stronger than physical bonds, the heat of adsorption is much higher in chemical adsorption reactions. This means that sorbents that can form chemical bonds with sorbate have a much higher adsorption capacity (Ghanbari et al., 2019). However, high adsorption heat also results in high regeneration temperatures. As mentioned before, a high regeneration temperature necessitates more energy, more CO_2 emissions, and higher costs. This review looks in depth at solid sorbents that perform physical adsorption.

A solid sorbent must have certain properties to be used in the CO_2 adsorption process under DAC conditions (Figure 8). The first and most important of these is that it has a porous structure. Porosity boosts the surface area of the material, and since adsorption occurs on the surface, the larger the surface area, the greater the adsorption capacity. Another important feature is the ability to resist moisture. Atmospheric air can contain up to 4% water vapor, which is much more concentrated than CO_2. Due to water molecules are polar, they have a much greater tendency to form relationships with the surrounding components than non-polar CO_2 molecules. As a result, the sorbent material must be chemically stable and have high CO_2 selectivity in order to be not impacted by moisture (Zanatta, 2023).

Zeolite and metal-organic frameworks, which are the most commonly used materials in DAC processes with the mentioned properties, are reviewed in detail in the following sections. MOFs, a newly developed material group, stand out with their manipulable properties, particularly when compared to zeolite.

2.1. Zeolite

Zeolite is a highly porous material that can form naturally by mixing volcanic materials and saline water, but it is also produced in laboratories present. It is made up of SiO_4 and AlO_4 compounds that are linked by an oxygen atom (Figure 9). The quadrupolar structure formed by aluminum has a high affinity for CO_2. As a consequence of this, it is a material that has been used in CO_2 capture processes (Behbahani and Green, 2023).
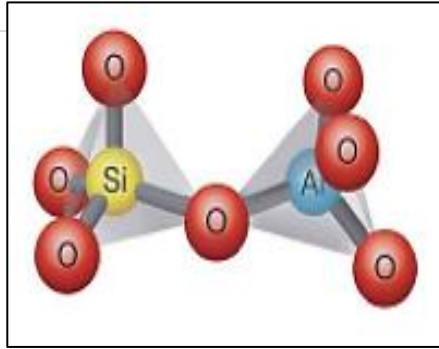
Figure 8: Atomic Structure of Zeolite (Behbahani and Green, 2023)

Unfortunately, research into how it performs under DAC conditions has demonstrated that it does not provide complete compatibility. This material, which has a strong affinity for CO_2, also has a strong affinity for water vapour, which is abundant in atmospheric air. As a result, working in a humid environment caused significant decreases in zeolite adsorption capacity. Approaches such as hydrophobic coatings and functionalization processes with amine groups have been utilized to mitigate this, with a certain increase in capture efficiency observed (Fu et al., 2022). However, after hydrophobization with amine groups, materials often become more inclined to chemical adsorption, making regeneration a more challenging process.

In a study that measured the adsorption capacity of zeolite released to humidity, the adsorption capacity of four different types of zeolite was analyzed when the air temperature was 25°C and -20°C. Although the capacities of different zeolite types vary, a significant increase in capacity was observed in all of them at -20°C, as shown in Figure 10 (a). While interpreting the data, it was proposed that the amount of water vapour in the air mixture at low temperatures was much lower, and a second study was conducted to confirm this, the results of which are shown in Figure 10 (b). This time, the same zeolite types were tested to capture conditions in which the amount of water vapor was increased by entering air with a temperature of -20°C. As can be seen, even though the temperature remained constant, the adsorption capacity of all zeolite types decreased as the amount of water vapour increased (Song et al., 2022).
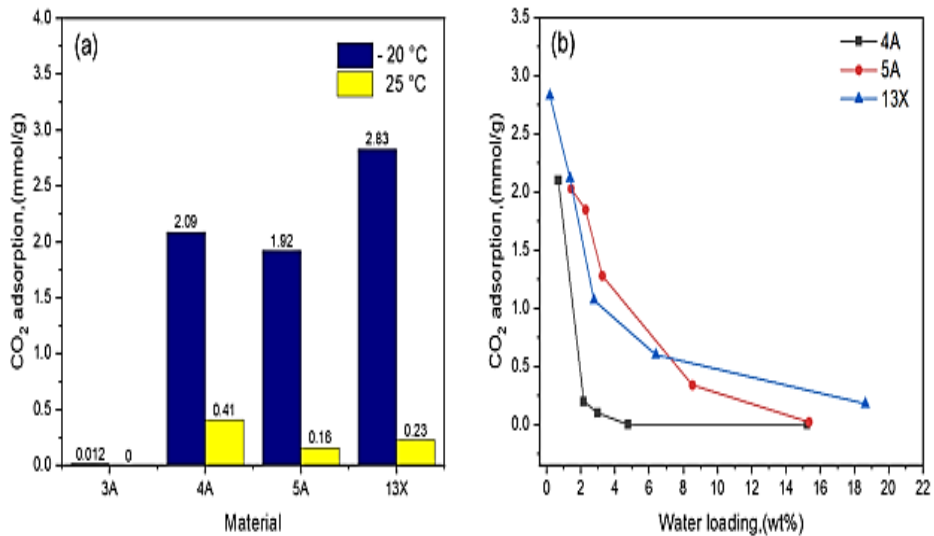
Figure 9: At 0.4 mbar CO_2 Pressure, Zeolite Types' (a) CO_2 Capture Capacities Related to Air Temperature and (b) CO_2 Capture Capacities Related to Humidity Rates at -20˚C (Song et al., 2022)

If the moisture resistance of zeolite is increased, it is obvious that it can be a good capture material for DAC conditions. Composite production experiments using zeolite-based nanoparticles are being conducted to improve these and other properties. It has been determined that such composites have good regeneration properties and a low efficiency decrease in repeated cycles (Li, 2023). Presently, research is being conducted to increase the adsorption capacity of this material.

2.2. Metal-Organic Frameworks (MOFs)

Metal organic cages are new generation materials with a highly porous structure consisting of metal ions or metal clusters and organic ligands that connect these metals, as illustrated in Figure 1 (Shi et al., 2023). Inorganic ligands can be used together with organic ligands in the same structure to provide metal binding. In this case, the material produced is also referred to as HUMs, which indicates hybrid ultra-microporous materials (Behbahani and Green, 2023).

Metals
or
Metal clusters

Organic linker
molecules

Metal-organic framework
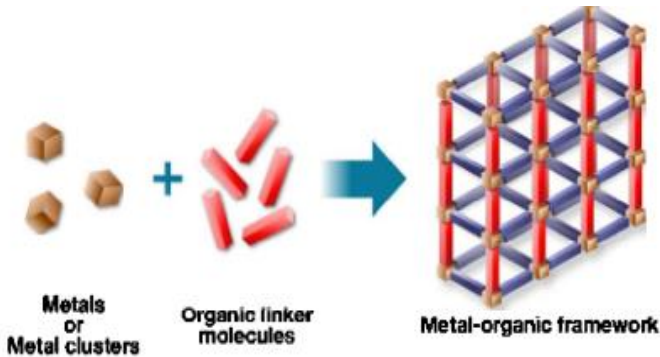
Figure 10: Structure of MOF (Behbahani and Green, 2023)

MOFs can have a specific surface area of up to 6000 m^2/g due to their high porosity (Tao and Xu, 2023). As shown some examples in Table 2 combinations of metal ions and/or organic ligands can be used to adjust the size of the pores with high tolerance (Zhang et al., 2023). All of these characteristics, as well as their development potential, make MOFs an ideal adsorbent material.

Table 2: Pore Sizes and BET Areas of MOF Materials Based on Metal Ion and Organic Ligands.

Materials Name	Metallic Group	Ligand Group	Pore Size (Å)	BET Area (m^2/g)	Ref.
Mg-MOF-74	Mg^{2+}	DOBDC (dioxybenzenedicarboxylate)	1.2	1495	(Kari et al., 2021)
SIFSIX-3-Cu	Cu^{2+}	SiF_6^{2-} (hexafluorosilicate)	3.54	300	(Forrest et al., 2019)
SIFSIX-3-Ni	Ni^{2+}	SiF_6^{2-} (hexafluorosilicate)	3.55	368	(Forrest et al., 2019)
UiO-66	$[Zr_6O_4(OH)_4]^{12+}$	$[OOC-C_6H_4-COO]^{2-}$ (BDC: benzenedicarboxylate)	7	1200	(Taddei, 2016)

Furthermore, MOFs can increase adsorption capacity by establishing mechanisms for interacting with the CO_2 atoms during adsorption process. Three concepts can be used to explain these mechanisms: kinetic sieving, Lewis interactions, and open metal sites (OMSs) (Figure 12).
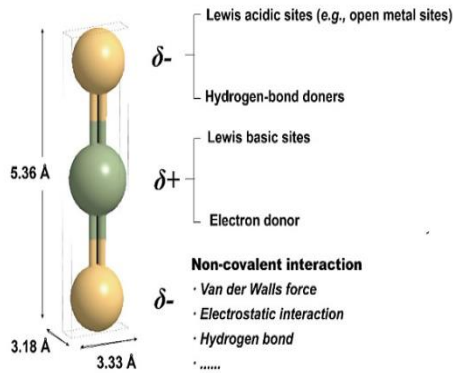
Figure 112: Geometric Dimensions and Physical Adsorption Interactions of the CO_2 Molecule (Zhang et al., 2023)

Adjusting the pore size of the MOF material close to 3.3 Å, which is the kinetic diameter of the CO_2 molecule, can assist in increasing CO_2 selectivity, according to the kinetic sieving approach. Other gases (such as N_2 and Ar) with much higher partial pressures than CO_2 under DAC conditions exhibit a higher adsorption tendency due to this pressure difference. As shown in Table 3, the kinetic diameter of the majority of these gases is greater than that of CO_2. Utilizing these values to design the MOF pore diameter will result in high CO_2 selectivity by creating a natural sieve effect, as large-sized gases cannot overcome the energy barrier that may cause pore deformation (Zhang et al., 2023). Figure 13 shows a graph comparing the CO_2 adsorption capacities of some of the MOF materials listed in Table 2, taking into account their pore diameters.

Table 3: Volume Fractions and Kinetic Diameters of Gas Molecules in the Air (Zhang et al., 2023).

Gas	Volume Fraction	Kinetic Diameter (Å)
CO_2	0.042%	3.3
N_2	78.084%	$3.64 - 3.80$
O_2	20.946%	3.467
Ar	0.934%	3.542
H_2O	0-4%	2.641
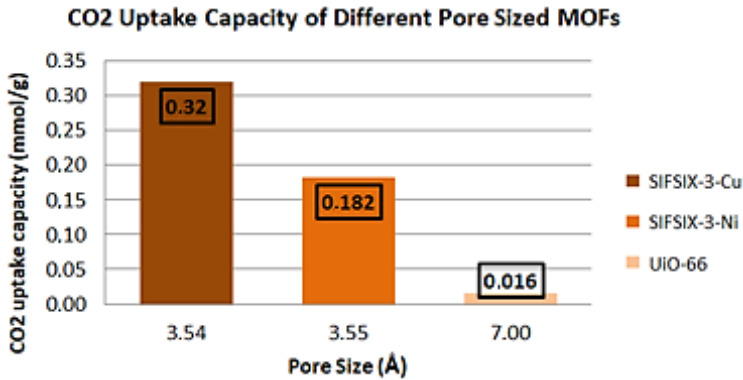
Figure 13: CO_2 Capture Capacities of Different MOF Materials Based on Their Pore Diameters (Shi et al., 2023).

Lewis interactions between CO_2 and MOF structure can be investigated as another factor that helps in adsorption. Organic ligands in the material structure have Lewis base properties due to their negatively charged nature. This interaction between the carbon atom in CO_2 and the Lewis bases in the MOF structure, particularly in the intrapore channels, strengthens the gas-material bond, improves CO_2 selectivity, and increases adsorption (Zhang et al., 2023).

OMSs are commonly used to increase the adsorption capacity of MOFs. Transition metals appear to be frequently used for MOF synthesis. Transition metals interact with other atoms via d orbitals, which is one reason for this (Ghanbari et al., 2019). According to D Band Center Theory, an adsorbate gas bound to the surface can form energy bands by interacting with these orbitals (Prabowo et al., 2017).

The high bond energy (enthalpy) indicates a strong interaction between the guest molecule and the solid surface. The binding enthalpies of some gases during adsorption on MOF-74 material are given in Table 4. Since the metals in the MOF structure have a positive charge, they are electrophilic and can act like a Lewis acid, accepting electrons that can be transferred by the oxygen atoms in the CO_2 structure. However, due to the high polarity of H2O atoms, which are more concentrated than CO_2, this mechanism is mostly

carried out by H_2O atoms rather than CO_2 under DAC conditions (Zhang et al., 2023). As shown in Table 4, the binding enthalpy of H2O is greater than that of CO_2 in all metal combinations except Cu. As a result, it will bind to the adsorbent material more strongly.

Table 4: Binding Enthalpies of the Flue Gas in the MOF-74 Structure (Ghanbari et al., 2019).

Flue gas	d^0 Mg	d^2 Ti	d^3 V	d^4 Cr	d^5 Mn	d^6 Fe	d^7 Co	d^8 Ni	d^9 Cu	d^{10} Zn
H_2	10	17	18	6	8	9	9	10	6	8
CH_4	19	23	26	14	19	19	18	19	14	19
N_2	28	58	52	14	21	21	21	24	13	19
CO_2	41	46	51	27	34	34	34	37	27	30
H_2O	62	71	77	31	51	49	48	56	24	41

Because of their high polarity, H_2O atoms can even compete with organic ligands in the MOF structure to interact with metal ions. A situation like this could lead to the framework collapsing. The bond between the ligand and the metal must be strengthened to prevent this. When paired according to the Hard and Soft Acid and Base (HSAB) theory, the MOF structure expected to operate under DAC conditions is designed to mitigate this risk. Metal ions with soft acidic properties should be paired with ligands with soft basic properties, and hard acidic metal ions should be paired with hard basic ligands. For example, due to Zn^{2+} having soft acidic properties, it can provide stronger bond coordination with an N-providing soft basic ligand. Furthermore, the use of shorter ligand chains has a growing effect on MOF stability (Zhang et al., 2023).

3. CONCLUSIONS

Global warming has evolved into a phenomenon that is accelerating and showing itself today. If no precautions are taken, it may reach a level that will exacerbate the current severe weather conditions, restrict our ability to access water, cause epidemics, and even lead to ocean acidification and the extinction of some species. The Paris Agreement, signed by many countries, states that we must keep global warming under 2˚C before it has a significant impact. For this purpose, capture technologies that reduce or even prevent CO_2 emissions, the primary cause of global warming, have become widely used. However, IPCC reports have revealed that even if zero emissions are achieved in this manner, it will take many years for the global climate to

return to normal. As a solution to this problem, DAC technology was created. It aims to reduce CO_2 levels in the air by capturing CO_2 that has already been released into the atmosphere. However, because it is a relatively new technology, it faces numerous challenges. The most significant of these is the high energy requirement, which makes this development impossible for a few businesses looking to increase their capture capacity. A second major issue is the lack of suitable sorbent material. Many sorbents that work well in other areas of capture cannot produce the expected results in DAC conditions due to CO_2 dilution and high humidity. Although chemical adsorption sorbents have a higher capacity, they require high regeneration temperatures due to the strong bonds they form with the CO_2 molecule, which increases the already high energy requirement. The high porosity of zeolite and MOF, two of the most promising sorbents for physical adsorption, distinguishes them from the others. Since it has been demonstrated that zeolite is extremely sensitive to moisture when not functionalized, current research focuses on this issue and attempts to give the material hydrophilic properties. MOF, on the other hand, with its intervenable and customizable structure, allows the way for the development of new solution methods. It provides numerous advantages, including adjustable pore size and the quantification of adsorption heats by selecting ligands and metal ions. With all of these characteristics, MOF, a new-generation material, is seen as a promising development for the future of DAC technology.

REFERENCES

Behbahani, H. S. and Green, M. D. (2023). Direct air capture of CO_2. Washington: ACS Publications. https://doi.org/10.1021/acsinfocus.7e7016

Beuttler, C., Charles, L., & Wurzbacher, J. A. (2019). The role of direct air capture in mitigation of anthropogenic greenhouse gas emissions. Frontiers in Climate, 1(10), 1-7. https://doi.org/10.3389/fclim.2019.00010

Climate change: vital signs of the planet, carbon dioxide concentration (n.d.). NASA Global Climate Change. https://climate.nasa.gov/vital-signs/carbon-dioxide/

Climate change: vital signs of the planet, global surface temperature (n.d.). NASA Global Climate Change. https://climate.nasa.gov/vital-signs/global-temperature/

De Temmerman, G. and De Rochette, F. (2023). The CDR series: direct air capture (DAC). Zenon Research, 1-16. https://hal.science/hal-03947547

Forrest, K. A., Pham, T., Elsaidi, S. K., Mohamed, M. H., Thallapally, P. K., Zaworotko, M. J., and Space, B. (2019). Investigating CO_2 sorption in SIFSIX-3-M (M = Fe, Co, Ni, Cu, Zn) through computational studies. Crystal Growth& Design, 19(7), 3732–3743. https://doi.org/10.1021/acs.cgd.9b00086

Fu, L., Ren, Z., Si, W., Qian, M., Huang, W., Liao, K., … Xu, P. (2022). Research progress on CO_2 capture and utilization technology. Journal of CO_2 Utilization, 66(102260), 1-29. https://doi.org/10.1016/j.jcou.2022.102260

García, J. G., Villén-Guzmán, M., Rodríguez-Maroto, J. M., and Paz-García, J. M. (2022). Technical analysis of CO_2 capture pathways and technologies. Journal of Environmental Chemical Engineering, 10(5), 1-18. https://doi.org/10.1016/j.jece.2022.108470

Ghanbari, T., Abnisa, F., and Daud, W. M. A. W. (2020). A review on production of metal organic frameworks (MOF) for CO_2 adsorption. Science of the Total Environment, 707(135090), 1-28. https://doi.org/10.1016/j.scitotenv.2019.135090

Kari, N. E. F., Bustam, M. A., and Ismail, M. (2021). Metal-organic frameworks: screening M-MOF-74 (M = CO, CR, CU, FE, MG, MN, NI, TI, and ZN) based for carbon dioxide adsorption. E3S Web of Conferences, 287(02011), 1-5. https://doi.org/10.1051/e3sconf/202128702011

He, L. (2023). CO_2 capture by various nanoparticles: Recent development and prospective. Journal of Cleaner Production, 414(137679), 1-11. https://doi.org/10.1016/j.jclepro.2023.137679

Overview of greenhouse gases. (2023). US EPA. https://www.epa.gov/ghgemissions/overview-greenhouse-gases

Ozkan, M., Nayak, S. P., Ruiz, A. D., and Jiang, W. (2022). Current status and pillars of direct air capture technologies. iScience, 25(4), 1-23. https://doi.org/10.1016/j.isci.2022.103990

Prabowo, W. a. E., Khoiroh, N., Wibisono, S., and Supardi, A. (2020). D-band center theory for the case of hydrogen atom adsorption on FE(100) and AL(100) surfaces: a density functional study. Journal of Physics, 1445(1), 1-6. https://doi.org/10.1088/1742-6596/1445/1/012011

Rigby, M., Prinn, R. G., O'Doherty, S., Montzka, S. A., McCulloch, A., Harth, C. M., …Fraser, P. J. (2013). Re-evaluation of the lifetimes of the major CFCs and CH3CCl3 using atmospheric trends. Atmospheric Chemistry and Physics, 13(5), 2691–2702. https://doi.org/10.5194/acp-13-2691-2013

Shi, X., Lee, G. A., Liu, S., Kim, D., Alahmed, A., Jamal, A., …Park, A. A. (2023). Water-stable MOFs and hydrophobically encapsulated MOFs for CO_2 capture from ambient air and wet flue gas. Materials Today, 65, 207–226. https://doi.org/10.1016/j.mattod.2023.03.004

Song, M., Rim, G., Kong, F., Priyadarshini, P., Rosu, C., Lively, R. P., and Jones, C. W. (2022). Cold-temperature capture of carbon dioxide with water coproduction from air using commercial zeolites. Industrial & Engineering Chemistry Research, 61(36), 13624–13634. https://doi.org/10.1021/acs.iecr.2c02041

Taddei, M. (2016). UiO-66: a case study metal-organic framework [Class handout]. Paul Scherrer Institut, Catalysis Class, 529-0502-00L.

Tao, Y. and Xu, H. (2024). A critical review on potential applications of metal-organic frameworks (MOFs) in adsorptive carbon capture technologies. Applied Thermal Engineering, 236(121504), 1-17. https://doi.org/10.1016/j.applthermaleng.2023.121504

Yoro, K. O. and Daramola, M. O. (2020). CO_2 emission sources, greenhouse gases, and the global warming effect. Advances in Carbon Capture in (pp. 3–28). Sawston: Woodhead Publishing. https://doi.org/10.1016/b978-0-12-819657-1.00001-3

Zanatta, M. (2023). Materials for direct air capture and integrated CO_2 conversion: advancement, challenges, and prospects. ACS Materials Science Au, 3(6), 576–583. https://doi.org/10.1021/acsmaterialsau.3c00061

Zhang, X., Zhao, H., Yang, Q., Yao, M., Wu, Y., and Gu, Y. (2023). Direct air capture of CO2 in designed metal-organic frameworks at lab and pilot scale. Carbon Capture Science & Technology, 9(100145), 1-23. https://doi.org/10.1016/j.ccst.2023.100145

CHAPTER 3

A NOVEL SLEEP APNEA SIMULATOR TOOL: A MEMS BASED APPROACH

Dr. Harun SÜMBÜL[1]

[1] Yesilyurt D.C. Vocational School, Ondokuz Mayis University,Samsun, Turkey, harun.sumbul@omu.edu.tr, Orcid ID: 0000-0001-5135-3410

INTRODUCTION

Sleep apnea (SA) is an important disease that can result in death (Sümbül at al., 2022). SA is an important and fatal disease affecting both the right and left heart ventricles and is marked by decreased oxygen saturation and repeated episodes of upper airway obstruction throughout a full night's sleep (Polat at al., 2008). During apnea, the patient stops breathing for 10 seconds or longer (Oliver at al., 2021).

SA, characterized by abnormal and potentially life-threatening episodes of breath cessation during sleep, poses a grave health risk. Sleep apnea (SA) impacts around 2% of middle-aged women and 4% of middle-aged men, as reported by Xie et al. in 2012. SA is a public problem in children as well as adults, and if not intervened early, it becomes a major health risk (Hui at al., 2010). SA is associated with cognitive impairment as well as cardiovascular effects (Yunxiao at al., 2015). Apnea is characterized by the magnitude of the respiratory effort falling below 5% of the regular value and stopping the airflow for at least 10 s (Várady at al., 2002). While certain instances of sleep apnea may have a physiological basis, it is considered pathological if there are more than 5 episodes of apnea per hour.

SA is generally classified into 3 groups:

• Obstructive type sleep apnea (OSA): is characterized by the presence of thoracic effort to continue breathing when the airflow is completely obstructed. It occurs when the airway is floppy in the throat, and this is the most common type of sleep apnea (Verbraecken at al., 2013).

• Central-type sleep apnea (CSA): This form of apnea is recognized by a complete cessation of both airflow and respiratory movements lasting a minimum of 10 seconds. This occurrence is attributed to the brain's inability to regulate the respiratory muscles (Sabil at al., 2019).

• Mixed-type sleep apnea (MSA): MSA is a combination of OSA and CSA (Diego at al., 2015). This type of apnea is characterized by no breathing effort and no airflow in the first part of the event and breathing effort in the last part without air flow (Herkenrath at al., 2019). Figure 1 illustrates sleep apnea-related types of breathing continuum.

According to research findings, around 84% of patients exhibit symptoms of OSA, 1% of patients experience CSA, and the remaining 15% of patients have central sleep apnea (Morgenthaler at al., 2006). While polysomnography (PSG) remains the essential standard for diagnosing apnea (Zoroglu and Türkeli, 2017), the literature encompasses various crucial measurement techniques and decision algorithms. Measurement techniques can be summarized as nasal air flow (Choi at al., 2018), SaO_2 (Tian and Liu, 2005), heart rate (Hayano at al., 2011), snoring voice (Rosenwein at al., 2015), wearable bands (Lin at al., 2016), ECG (Sakai at al., 2013), pressure monitoring (Glos at al., 2018), accelerometer (Yüzer at al., 2019), neural network (Yüzer at al., 2020), and in-bed force sensors (Waltisberg at al., 2017). In addition,

OSA is among the prevalent chronic respiratory disorders, and major comorbidities include cardiovascular diseases (Lee and McNicholas, 2011). Therefore, while investigating sleep apnea, basic respiratory parameters should also be examined.
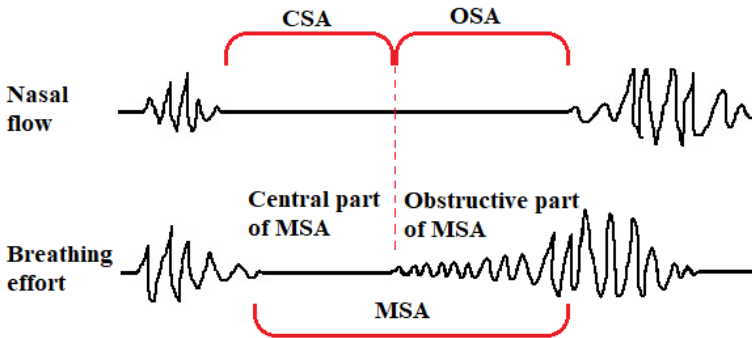
Figure 1. Sleep apnea-related to types of breathing continuum (Herkenrath at al., 2019).

Therefore, the human respiratory mechanism (Chen at al., 2021) has been studied in detail, and its similarity with the parameters that can be adjusted in the simulator has been provided. The parameters of RR (respiratory rate), TV (tidal volume), MVV (maximum voluntary ventilation) and FVC (forced vital capacity), which are among the most important parameters for COPD, were determined from the related literature (Feher,

2017; Barthel at al., 2012; Sümbül and Yüzer, 2016) and their simulations were carried out successfully.

As a result of detailed literature and market research (both academic and commercial), it has been discerned that numerous studies about SA in the literature, but there are no studies on SA simulator. This simulator can also serve as a useful biomedical lecture tool, with its ability to be shown repeatedly in biomedical-related courses for the investigation of basic respiratory parameters and apnea events. The presented study can provide a practical solution for use in courses in medical schools and others in the field of biomedical device technology education. Hence, it is anticipated that the provided study will address a significant void in the literature on biomedical device technology. In this study, we investigated sleep apnea, its types, physiological formation and basic breathing parameters, existing devices and their working principles, and we tried to realize a simulator in light of this information. To achieve this, we created a test setup for the simulator by realizing a pneumatic circuit and an electronic circuit with a microcontroller controlling this circuit.

2. METHOD

The purpose of the study in this article is to design and manufacture a simulator device to be used as a training set in biomedical device technology that can simulate apnea episodic cases and basic respiratory parameters and provide real-time monitoring and control over the developed interface. Figure 2 shows the general architecture of the simulator.
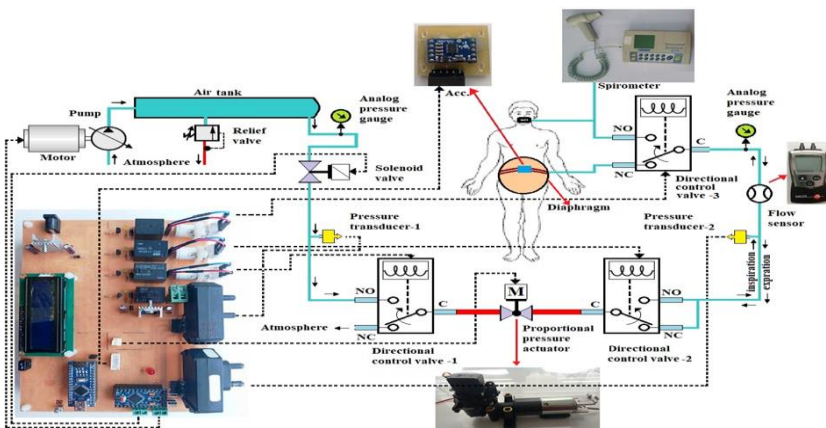
Figure 2. General schematic of the suggested simulator

According to the mode selected from the interface, the device directs the air flow through the directional control valve. The air pressure supplied to the system is in the range of 4-20 cmH$_2$O pressure (approximately 20 mBar) and can be adjusted with the help of the compressor regulator. The air tank that supplies air to the system must be filled with the help of the button on the interface before each use. Additionally, the amount of air available in the tank can be seen in real time. The system flow status can be followed on the LCD screen on the card. In the case of power failure, the system continues to operate with the help of rechargeable batteries placed under the circuit, so the device can be used in portability.

2.1. Definition of the Hardware Components

The pneumatic actuator is one of the most important parts of the simulator device. The pneumatic actuator has a servo control system, a venture tube and a fully enclosed pneumatic piston-type actuator. The model is designed to throttle and increase the air passing through the venture tube. Actuator control (to throttle the air) is provided by the servo motor. According to the rotation angle of the servo motor, the restriction mechanism in the actuator moves forward over the movable spring and restricts the air passing through the venture tube. The technical drawing is shown in Figure 3.
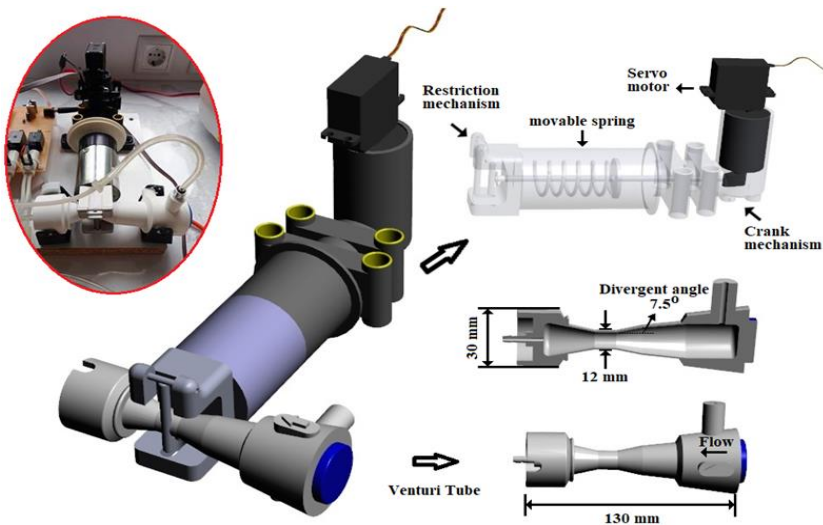
Figure 3. Pneumatic Actuator and Venture tube

A venture tube is a mechanism used to find the velocity of fluids by using this pressure difference. The Venture tube was designed with the Fusion360 program and produced using a 3D printer. Venture tubes are widely used in industry (Song at al., 2021; Soyama, 2021). As a result of mathematical calculations in light of Bernoulli's equations, the instantaneous flow rate is calculated as in equation (1) (Beaulieu at al., 2012; Shi at al., 2020).

$$A\frac{dqv(t)}{dt} + B|qv(t)|qv(t) = \frac{\Delta P(t)}{\rho} \qquad (1)$$

where A and B are flow meter geometric parameters (major diameter is 30 mm, overall length is 130 mm), q; volume flow, ΔP is the pressure difference between inlet and outlet. Pneumatic differential pressure sensor 163PC01D75 (measuring range ± 623 Pa, accuracy ± 0.15% full scale, Honeywell, Minneapolis, MN, USA) was used to measure the air pressure to calculate the amount of air taken and delivered in the simulator (Tardi at al., 2015). This sensor has a low power consumption of 10 mW at 5 V and consumes little energy. This sensor is used in many medical applications (Schena at al., 2015; Lo Presti at al., 2019). The differential pressure sensor used in the simulator provides an analog output voltage proportional to the applied pressure (internet, 2019). Since the volumetric flow rate is a function of time, the volume of air (V) can be calculated as in equation (2) (Mehta and Sinha, 2013);

$$V = \int_{t1}^{t2} (P1 - P2)\, dt \qquad (2)$$

where (P1 - P2) is the value measured by the differential pressure transducer.

There is an acceleration sensor based on Mems (Micro-Electro-Mechanical Systems) on the simulator to measure abdominal movements and discriminate apnea. Mems-based accelerometers are widely used in many different applications (Sümbül and Böğrek, 2013; Biryukova and Koretskaya, 2018). In medical practice, it is vital to know the lying positions of patients and elderly patients during sleep (Sümbül and Yüzer, 2016). In this research,

the MMA7361 L accelerometer and a gyroscope are employed. The MMA7361 L represents an analog-based MEMS accelerometer (Priswanto et al., 2019). Therefore, measured analog data were enumerated with the help of ADC to be used in the microcontroller.

When MMA7361 L is positioned according to Figure 3 to measure abdominal movements, the X-, Y-, and Z-axis output information is calculated according to equations (3) and (4) as follows:

$$Vx = Vy = (0.8 * Sin\theta)volt \tag{3}$$

$$Vz = (0.8 * Cos\theta)volt \tag{4}$$

Spirometry furnishes flow-volume and volume-time curves, offering a basis for evaluating numerous pulmonary function parameters (Nepomuceno at al., 2021). It has an important point in biomedical technology (Sümbül and Yüzer, 2017; Sümbül and Yüzer, 2017). The system is calibrated with both an industrial spirometer (Fukuda Sangyo spiroanalyze ST-75 model) and Testo 510 Differential Pressure Gauge. Figure 4 shows the simulator system experiment setup.
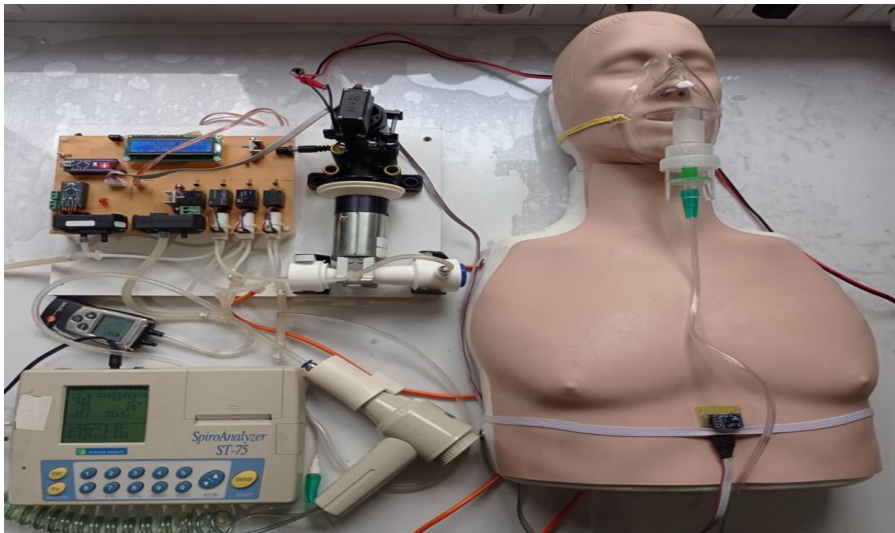
Figure 4. Experimental setup of the simulator system

The flowchart illustrates the procedural steps of the simulation algorithm, as depicted in Figure 5.
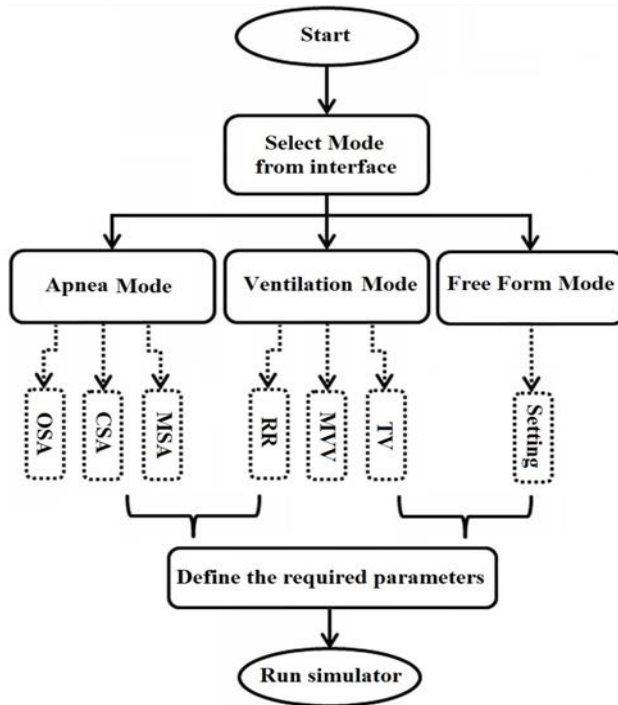
Figure 5. The flowchart for the simulator system

2.2. Prepared User Interface

In this section, the user interfaces and working principle of the simulator were explained. The user interface has been developed using the C# programming language, featuring a highly functional and user-friendly structure. With the help of this interface, the user can first select the type of apnea mode (Apnea Mode, Basic Mechanical Ventilation Mode and Free Form Mode) to be simulated. Once the required mode is selected, a different interface is opened for the user to set the parameters of the selected mode. After the required parameters are given and selections are made with this interface, the procedure given in Figure 5 works. When simulation is started, while the device operates the hardware connected to it, it also provides real-time monitoring from the computer screen by making the necessary measurements on the model man. At the end of the study, respiration,

inspiration, expiration and apnea graphs of the tested mode were obtained. In this study, an interface was created, and a clear procedure was presented for biomedical students to analyses the dynamic behavior of respiratory physiology and to make concrete measurements about apnea.

Figure 6 shows the first screen of the developed interface. This interface contains general information about the simulator and a graphic environment that allows viewing of previously recorded data, mode selection buttons and other setup buttons. In this menu, there are many useful features and settings, such as filtering the data saved in different formats, separating, zooming, showing the point values on the graph, saving as a picture and printing.
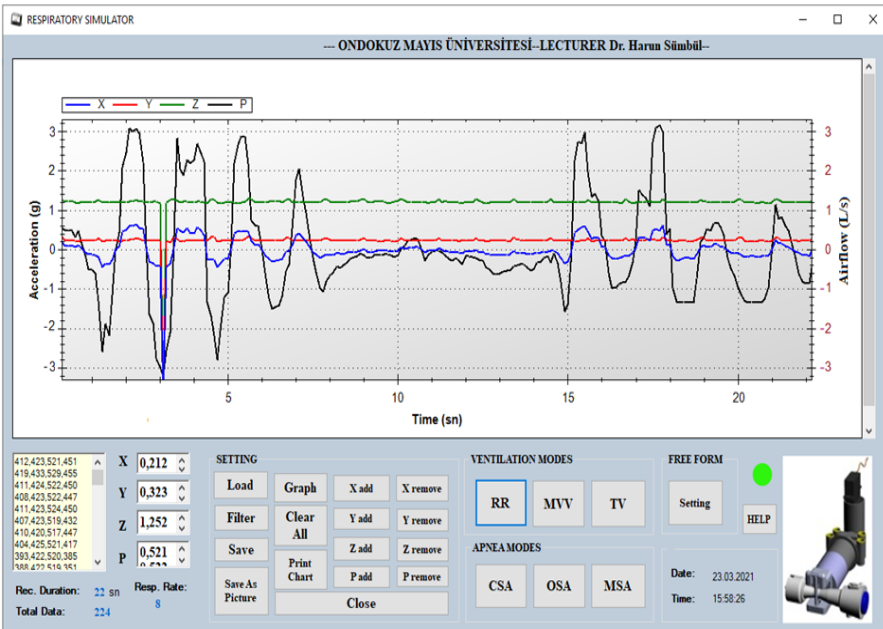
Figure 6. The main window of the simulator interface.

If operations such as graphical display, analysis, and filtering of previously recorded data are to be performed, the simulation can be started by clicking the appropriate buttons under the SETTING heading. If a new simulation will be started optionally in the simulator mode, the device can be started by pressing the relevant button on the right. When the relevant mode is selected and the button is clicked, the new interface given in Figure 7 will

open (Tidal Volume Menu, example). A new and different interface meets the user for each mode.
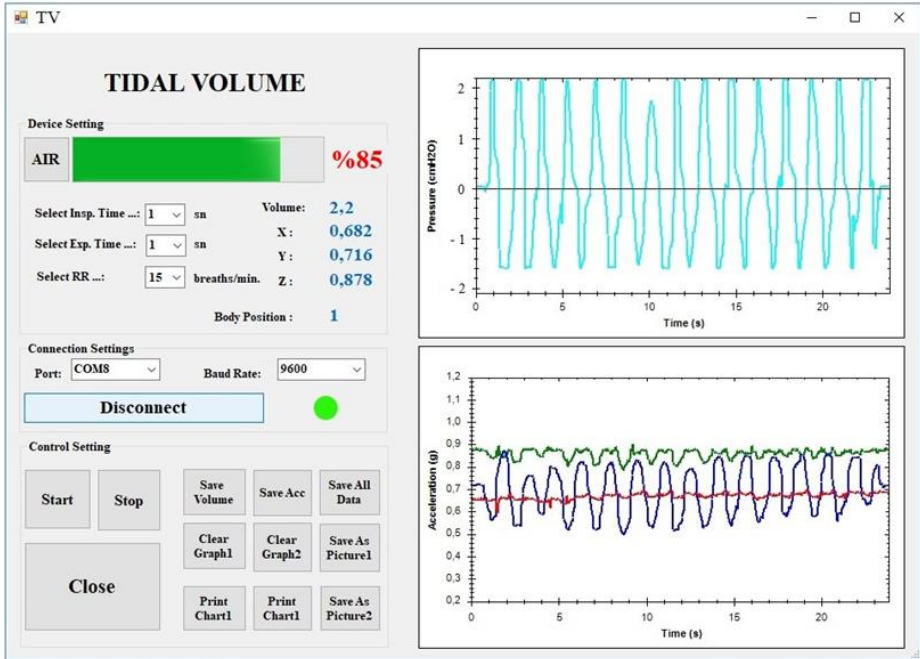
Figure 7. Tidal volume interface.

There is also a helpful option in this chapter, which includes descriptive information about the interface and the use of the program. When the help option is selected, the interface is prepared on the information page, information about the working principle of the program, basic respiratory parameters, apnea and its graphics and interpretation, satisfactory explanations about the hardware components used in the study and the user manual are reached. Firstly, it is necessary to make a connection between the device and the computer, and then, according to the tank filling status, if needed, the tank should be filled with air before the simulator is started. Commencing the simulation is achieved by activating the "start" button within each interface. By initiating the process through the "Start" button, the device commences operations based on the specified parameter values. The air condition in the air tank, patient body position, air volume in the lungs of the patient, air flow rate and abdominal diaphragm movements can be monitored

in real time through this interface. Simulation can be stopped and paused, and all measured data can be recorded. The interface also offers the possibility to print the graphic via the printer or to save the graphic as an image file. Figure 8 shows other interfaces of system control. These interfaces can be accessed from the main page. If the user wants to select which mode, clicks on the interface and accesses the relevant page. It runs the simulator by selecting the other parameters it needs here. While the simulator controls the output according to the values set on the one hand, it also makes measurements from the other side. It is possible to monitor all measurements in real time via the program.

(a)	(b)
(c)	(d)
(e)	(f)
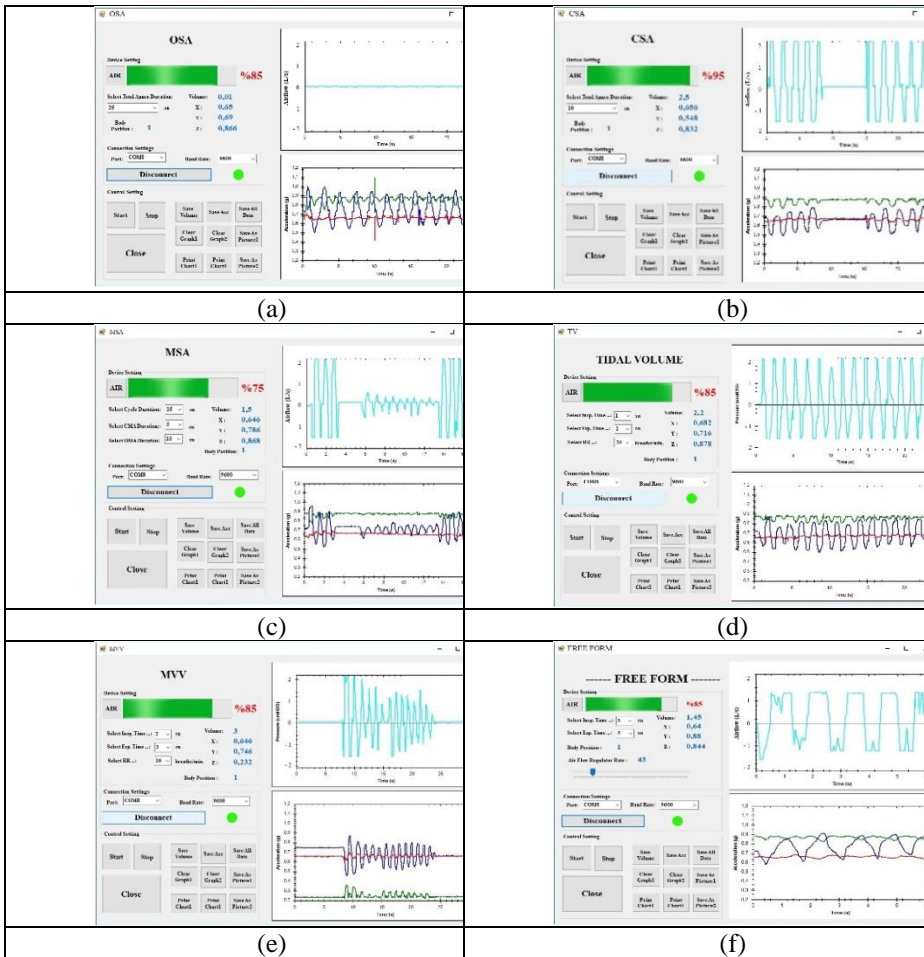
Figure 8. Simulator menus for OSA (a), CSA (b), MSA (c), TV (d), MVV (e) and FREEFORM (f)

The MAF (moving average filter) is used to calculate the output y(i) as a running average of the input signals x(i), as shown in equation (5):

$$y(i) = \frac{1}{k+1}\sum_{j=0}^{k} x(i-j) \qquad (5)$$

where y (i) is flattened and time-delayed version of x (i). If (k + 1) is averaged over, the output y(i) is smoother and over delayed. The delay occurs because the output y(i) is a task of only the current and preceding inputs x(i − j), $0 \leq j \leq k$ (Fig. 9) (Lynch at al., 2016). Figure 9 shows the example operation of the filter.
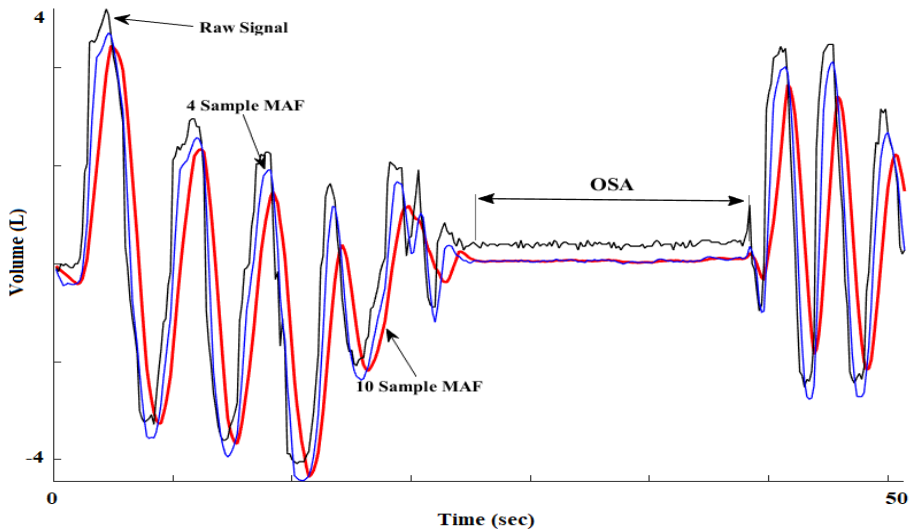
Figure 9. The illustration provided with the color black depicts the raw noise signal represented by x(i), signal z(i) derived from filtering through 4-point MAF (k = 4), and the signal from a 10-point MAF denoted as z(i) (k = 10).

RESULTS

To test the system performance, spirometry was connected to the simulator device, and 5 different modes (OSA, CSA, MSA, TV and MVV) were performed. In total, 3326 volume data were measured and recorded (excluding acceleration data). Measurements were conducted concurrently. Several graphics obtained as a result of test measurements are presented in Fig. 10.
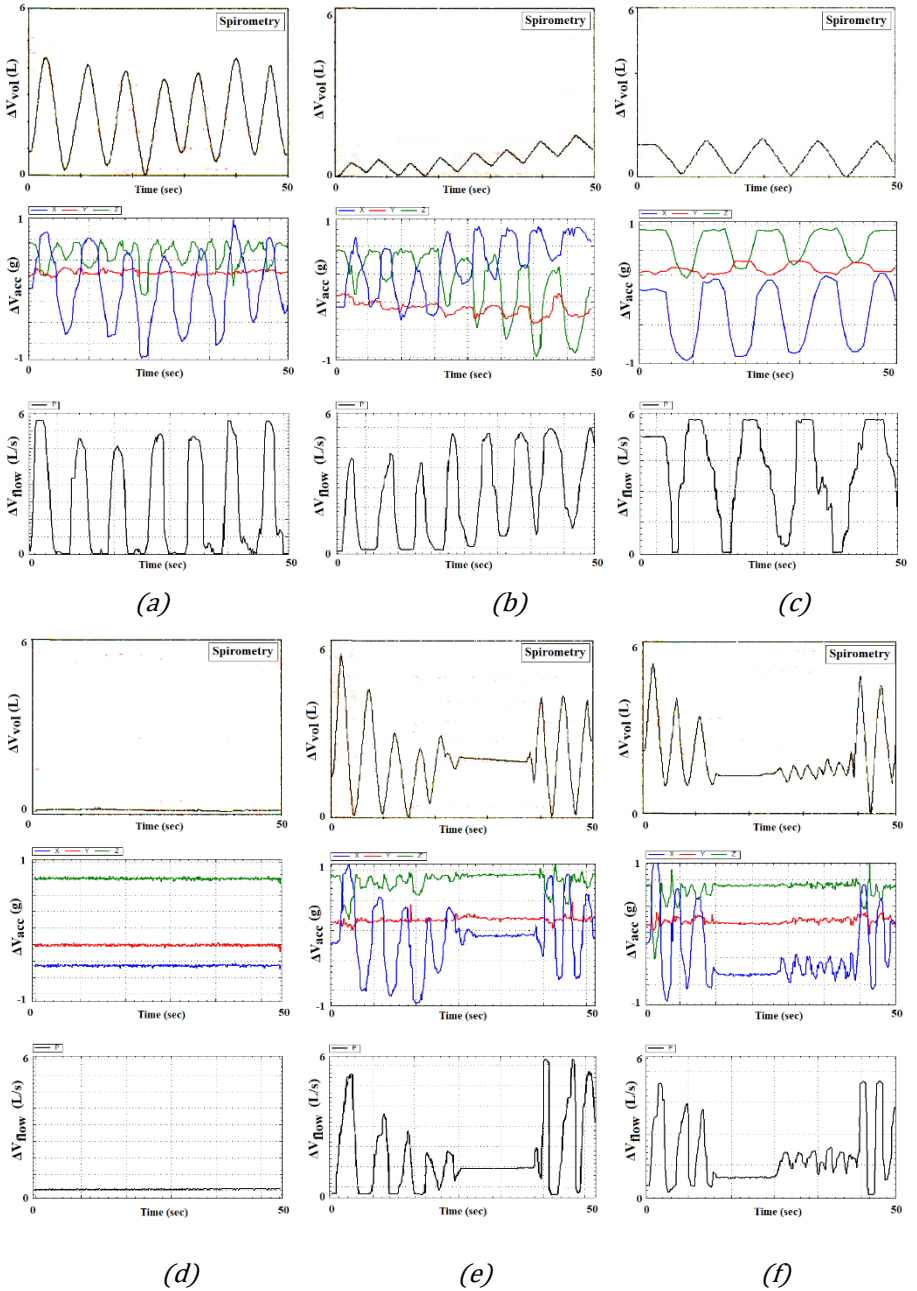
Figure 10. Graphs for (a) TV, (b) MVV, (c) Free Form, (d) CSA, (e) OSA, (f) MSA

The developed experimental education set was successfully used in BCL (Biomedical Device Lab) courses (Course Codes; BCT110, BCT213, BCT203) for the students of the Biomedical Device Technology Department of Ondokuz Mayıs University, and very positive results were obtained from the students. To evaluate our proposed method, the sensitivity, specificity and accuracy rates are calculated using the following formulas given in Eq. (6, 7, 8) respectively.

$$\text{Accuracy} = \frac{TN + TP}{TN + TP + FP + FN} \; X \; 100 \tag{6}$$

$$\text{Sensitivity} = \frac{TN}{TN + FP} \; X \; 100 \tag{7}$$

$$\text{Specificity} = \frac{TP}{TP + FN} \; X \; 100 \tag{8}$$

Overall, the accuracy is 97%, sensitivity is 98% and specificity is 96%. Precision, recall and f1-score parameters were also calculated as 0.96, 0.97 and 0.96, respectively. A confusion matrix was formulated to evaluate the performance of the our classifier employed. Table 1 represents values of these measures calculated for five different modes:

Table 1. The confusion matrix derived from the simulator

A	P	
	Predicted: (0)	Predicted: (1)
Actual: (0)	1986	47
Actual: (1)	27	1266

CONCLUSIONS

In the proposed study, a simulator device was developed that can also measure basic mechanical ventilator parameters. Thanks to this system, it can

be observed how and which form apnea occurs. Some important parameters, such as apnea duration, apnea type, and inspiration and expiration times, can be measured as intended via the developed interface. All changes can be monitored instantly through the interface, and data can be recorded. In terms of this feature, the system can be used repeatedly. Medical spirometry (Fukuda Sangyo brand spiroanalyze ST-75 model) and Testo 510 Differential Pressure Gauge were used for the accuracy and calibration of the simulator system. Simultaneous sample measurements were carried out for 5 different modes, and according to the statistical analysis made as a result of the measurements, it was observed that the simulator device had very high accuracy, sensitivity, and specificity. Thus, with the simulator system developed, it has been observed that reliable, consistent, and successful results can be obtained for apnea detection and classification and can be used safely in biomedical applications and training.

DISCUSSION

It is known that apnea disease is a subject that is important and deeply needs to be studied. An apnea simulator device similar to the device presented in the detailed literature review conducted in both academic and commercial fields was not encountered. For investigations on this subject, hospitals are visited, and studies are carried out in sleeping rooms in hospitals, or many studies are theoretically given without practice. With this study, an important biomedical instrument has been developed that can be used in apnea studies and practice courses in health sciences, medicine, biomedical device technologies, biomedical engineering, and emergency medicine technicians.

The proposed simulator concept can be quickly approved with the permission of the relevant authorities to be used as a respiratory system simulator in daily clinical practice, which is very important during the pandemic period. In addition, new innovative technological solutions can be developed, including the integrated automatic control of all systems. It is planned to enable the simulator to be used with the web interface in the light of difficult pandemic conditions and thus to make this training set suitable for the distance education model.

REFERENCES

Alvarez-Estevez, D., & Moret-Bonillo, V. (2015). Computer-Assisted Diagnosis of The Sleep Apnea-Hypopnea Syndrome: a review. Sleep Disorders, 2015, 237878, 33 pages.

Barthel, P., Wansel R., Bauer A., Müller A., Wolf P., Ulm K., Huster K. M., Francis D. F., Malik M. and Schmidt G. (2012). Respiratory Rate Predicts Outcome After Acute Myocardial Infarction: A Prospective Cohort Study. European Heart Journal, 34(22), 1644–1650.

Beaulieu, A., Foucault, E., Braud, P., Micheau, P., Szeger, P. (2011). A Flowmeter for Unsteady Liquid Flow Measurements, Flow Measurement and Instrumentation. 22(2):131-137.

Biryukova, O. V., & Koretskaya, I. V., (2018). The Usage of Acceleration Sensor to Control Spatial Orientation for Experiment Automatization, Conference: Systems of Signal Synchronization, Generating and Processing in Telecommunications (SYNCHROINFO) Location: Belarusian State Acad Commun, Minsk, BELARUS. 1-6.

Chen, A., Zhang, J., Zhao, L., Rhoades, R. D., Kim, D. Y, Wu, N., Liang, J. and Chae J. (2021). Machine-Learning Enabled Wireless Wearable Sensors to Study Individuality of Respiratory Behaviors, Biosensors and Bioelectronics, 6(173), 112799.

Choi, S. H., Yoon, H., Kim, H. S., Kim, H. B., Kwon, H. B., Oh, S. M., Lee, Y. J., Park, K. S. (2018). Real-time apnea-hypopnea event detection during sleep by convolutional neural networks, Comput Biol Med. 2018 Sep 1(100), 123-131.

Diferansiyel basınç sensörü İnternet:https://tr.farnell.com/honeywell/163pc01d75/pressure-sensor-2-5-h2o/dp/731882 (21.12.2021, 22:14:18).

Ding, H., Liu, X. C. & Zhang, J.P. (2010). Influence of Obstructive Sleep Apnea Syndrome on Cognition Development in Children, Biological Rhythm Research, 41(3), 235-246.

Feher J. (2017). Lung Volumes and Airway Resistance. Editors: Merken S, Mcfadden N. Quantitative human physiology (second edition) an introduction, 633-641, Elsevier.

Faust, O., Barika R., Shenfield, A., Ciaccio, E. J., Acharya, U. R. (2021). Accurate Detection of Sleep Apnea With Long Short-Term Memory Network Based On RR Interval Signals, Knowledge-Based Systems, 212, 106591, 1-10.

Glos, M., Sabil, A., Jelavic, K. S., Schöbel, C., Fietze, I., Penzel, T. (2018). Characterization of respiratory events in obstructive sleep apnea using suprasternal pressure monitoring., J Clin Sleep Med. 14(3):359-369.

Hayano, J. et al., (2011). Diagnosis of sleep apnea by the analysis of heart rate variation: A mini review. 2011 Annual International Conference of the

IEEE Engineering in Medicine and Biology Society, Boston, MA, 7731-7734.

Herkenrath, S., Pavsic, K., Treml, M., Hagmeyer, L., Randerath W. (2019). Mixed apnea metrics during diagnostic polysomnographies in obstructive sleep apnea patients with/without treatment-emergent central sleep apnea, European Respiratory Journal, 54: Suppl. 63, PA824.

Johan, V., (2013). Complex Sleep Apnoea Syndrome. Breathe, 9(5): 372-380.

Lin, Y. Y., Wu, H. T., Hsu, C. A., Huang, P. C., Huang, Y. H. and Lo, Y. L. (2016). Sleep apnea detection based on thoracic and abdominal movement signals of wearable piezo-electric bands. IEEE Journal of Biomedical and Health Informatics. 21(6), 1533 – 1545.

Lynch, K. M., Marchuk, N., Elwin, M.L. (2016). Chapter 22 - Digital Signal Processing, Embedded Computing and Mechatronics with the PIC32, 2016, Pages 341-374.

Mehta, P., & Sinha, V. (2013). Development of First Proto-Types of a Low-Cost Computer based Solid-State Spirometer for application in rural Health-Care Centres across India. Global Journal of Medical Research, 13(12), 7-17.

Morgenthaler, T.I., et al., (2006). Complex sleep apnea syndrome: is it a unique clinical syndrome? Sleep New York Then, Westchester, 29(9), 1203.

Nepomuceno, A. C., Alberto, N., Andre, P., Antunes, P. F. D., Domingues, M. D. (2015). 3D Printed Spirometer for Pulmonary Health Assessment Based on Fiber Bragg Gratings. IEEE Sensors Journal. 21(4), 4590-4598.

Polat, K., Yosunkaya, Ş., Güneş, S. (2008). Comparison of Different Classifier Algorithms on the Automated Detection of Obstructive Sleep Apnea Syndrome. J Med Syst 32, 243–250.

Presti, D. L., Romano, C., Massaroni, C., D'Abbraccio, J., Massari, L., Caponero, M. A., Oddo, C. M., Formica, D., Schena, E. (20149). Cardio-Respiratory Monitoring in Archery Using a Smart Textile Based on Flexible Fiber Bragg Grating Sensors. Sensors, 19(16), 3581, 2019.

Priswanto, A., Maryanto, S., Santoso, D. R. (2019). Wireless Sensor Module For 3-Axis Vibration and Tilt Monitoring on The Structural Building, Journal of Physics: Conf. Series 1153(1), 012040.

Rosenwein, T. et al., (2015). Breath-by-breath detection of apneic events for OSA severity estimation using noncontact audio recordings. 37th Annual International Conference of the IEEE Engineering in Medicine and Biology Society (EMBC), Milan, 7688-7691.

Ruth, L., & Walter, T. M. (2011). Obstructive Sleep Apnea in Chronic Obstructive Pulmonary Disease Patients, Current Opinion in Pulmonary Medicine. 17(2), 79-83.

Sabil, A. K., Christoph, S., Martin, G., Alexandra, G., Christian, V., Philipp, A., Ingo, F., & Thomas, P. (2019). Apnea and hypopnea characterization using esophageal pressure, respiratory inductance plethysmography, and suprasternal pressure: a comparative study. Sleep and Breathing. 23, 1169–1176.

Sakai, M. et al., (2013). Development of Lead System for ECG-Derived Respiration Aimed at Detection of Obstructive Sleep Apnea Syndrome. 2013 International Conference on Signal-Image Technology & Internet-Based Systems, Kyoto, 971-975.

Schena, E., Massaroni, C., Saccomandi, P., Cecchini, S. (2015). Flow Measurement in Mechanical Ventilation: A review. Medical Engineering & Physics, 37(3), 257-264.

Shi, H., Liu, Q., Nikrityuk, P. (2020). Numerical Study of Mixing of Cavitating Flows in A Venturi Tube, Canadian Journal of Chemical Engineering, 99(3): 813-828.

Song, Y., Shentu, Y., Qian, Y., Yin, J., Wang, D. (2021). Experiment And Modelling Of Liquid-Phase Flow In A Venturi Tube Using Stereoscopic PIV, Nuclear Engineering and Technology, 53(1): 79- 92.

Soyama, H. (2021). Luminescence Intensity Of Vortex Cavitation In A Venturi Tube Changing With Cavitation Number, Ultrasonics Sonochemistry, 71,105389.1-11.

Sümbül, H., & Yüzer A. H., (2016). The Measurement of COPD Parameters (VC, RR, and FVC) by using Arduino Embedded System. 1st International Mediterranean Science and Engineering Congress (IMSEC2016) Çukurova University, Congress Center, Adana, Turkey. 201-207.

Sümbül, H., Yüzer, A.H. & Şekeroğlu, K. (2022). A Novel Portable Real-Time Low-Cost Sleep Apnea Monitoring System based on the Global System for Mobile Communications (GSM) Network. Med Biol Eng Comput 60, 619–632.

Sümbül, H., & Böğrek, A., (2017). Development of The Road Analysis System to Provide the Fuel Efficiency Awareness in the Vehicles," Bilge International Journal of Science and Technology Research. 1(Special Issue) (1), 6–9.

Sümbül, H., & Yüzer A. H. (2016). 3D Monitoring of Lying Position for Patients with Positional Sleep Apnea Syndrome. Journal of New Results in Science. 12(2016), 59–70.

Sümbül, H., & Yüzer A. H. (2017). Development of Diagnostic Device for COPD: A MEMS Based Approach. IJCSNS International Journal of Computer Science and Network Security. 17(7), 196-203.

Sümbül, H., & Yüzer A. H. (2017). Estimating the Value of the Volume from Acceleration on the Diaphragm Movements During Breathing. Journal

of Engineering Science and Technology, School of Engineering, Taylor's University. 13(5), 1205 – 1221.

Tardi, G., Massaroni, C., Saccomandi, P, and Schena, E. (2015). Experimental Assessment of a Variable Orifice Flowmeter for Respiratory Monitoring, Journal of Sensors. 2015, 752540, 1- 7.

Tian, J. Y. and Liu, J. Q. (2005). Apnea Detection Based on Time Delay Neural Network. 2005 IEEE Engineering in Medicine and Biology 27th Annual Conference, Shanghai, 2571-2574.

Várady P. et al., (2002). A Novel Method for the Detection of Apnea and Hypopnea Events in Respiration Signals. IEEE Transactions on Biomedical Engineering. 49(9), 936-942.

Waltisberg, D., Amft, O., Brunner, D. P., and Troster, G. (2017). Detecting disordered breathing and limb movement using in-bed force sensor. IEEE Journal of Biomedical and Health Informatics. 21(4), 930-938.

Xie, B., & Minn H. (2012). Real-Time Sleep Apnea Detection by Classifier Combination. IEEE Transactions on Information Technology In Biomedicine. 16(3), 469-477.

Yunxiao, Wu., Zhifei, Xu., Zhang, L., & Shen, K. (2015). Screening Obstructive Sleep Apnea–Hypopnea Syndrome from Snorers In Children By Heart Rate Variability Analysis, Biological Rhythm Research, 46(2), 161-171.

Yüzer, A. H., Sümbül, H. and Polat, K., A. (2019). Novel wearable real-time sleep apnea detection system based on the acceleration sensor", IRBM Innovation and Research in BioMedical engineering. 41(1), 39-47.

Yüzer, A. H., Sumbul, H., Polat K., & Nour M. (2020). A Different Sleep Apnea Classification System with Neural Network Based on The Acceleration Signals, Applied Acoustics, 163, 107225, 1-8.

Zoroglu, C., Türkeli, Serkan. (2017). Fuzzy Expert System for Severity Prediction of Obstructive Sleep Apnea Hypopnea Syndrome. The Journal of Cognitive Systems. 2(2), 37-43.

CHAPTER 4

APPLICATIONS OF QUANTUM TECHNOLOGY IN IMAGE PROCESSING: A REVIEW STUDY ON ELECTRIC-ELECTRONIC BASED DETECTION AND NON-DESTRUCTIVE TESTING METHODS

Dr. Taner ÇARKIT[1]

MSc. Mete BERBEROĞLU[2]

Phd(c). Sümeyye ÇARKIT[3]

[1]Dept. of Electrical and Electronics Engineering, Kırklareli University, Kırklareli, Turkey, tanercarkit@klu.edu.tr, ORCID ID 0000-0002-5511-8773

[2]Dept. of Electrical and Electronics Engineering, Kırklareli University, Kırklareli, Turkey, mete.berberogluqklu.edu.tr, ORCID ID 0000-0002-5236-4813

[3]Food Sup. Sec. and Digital. Joint App. and Res. Center, Kırklareli University, Kırklareli, scarkit@klu.edu.tr, Turkey ORCID ID 0000-0003-2826-6575

INTRODUCTION

Until the current century, operations in the field of technology had been carried out with combinations based on the numbers 0 and 1. In the last century, humanity has been in search of a new technology revolution that includes subatomic particles, information and speed. Quantum technology (Q-technology) is the most likely option to be the name of this revolution. Q-mechanics is one of the sub-branches of physics that studies the behaviors of particles at atomic and subatomic levels. Q-technology describes the possibilities created by combining the fields of physics and related engineering using the principles of Q-mechanics. Some important concepts for Q-technology are:

- Quantum computing (Q-computing): Phenomenas such as quantum entanglement and quantum superposition enabled the usage of novel techniques for information processing that may be faster or more powerful than what traditional computers are capable of (Yetis, 2022). Q-computing offers speed as well as the ability to solve extremely complex calculations unsolvable by the world's most powerful supercomputers.
- Quantum communication (Q-communication): Ways to make communication between users, customers, and businesses safer, as well as data storage, are being explored [URL-1, 2023; URL-2, 2023]. Q-communication offers the ability to initiate the quantum internet, which enables the exchange of quantum signals between quantum computers (Q-computer), sensors, and any device.
- Quantum sensors (Q-sensors): Q-sensors are based on ultra-cold atoms and/or photons. In the studies carried out to increase the accuracy and sensitivity of the sensors, the acquisition of a higher quality signal is aimed through the reduction of the signal to noise ratio of the data signal which is being used in areas such as detection, targeting, and measurement.
- Quantum simulation (Q-simulation): The modeling of complex systems reduces the amount of resources spent on trial and error experiments.

Quantum-based new generation systems replace conventional technological methods with much faster and more powerful systems. Currently, the areas that benefit from this power and the potential use of Q-technology are given in Figure 1 (Gell-Mann, 1979; Goyal et. al., 2009;Kaptan, 2017; Hempel et. al., 2018; URL-3, 2023; URL-4, 2023). Considering these fields of study, some of the situations that are expected to occur as a result of the use of specialized systems with Q-technology support are listed below:
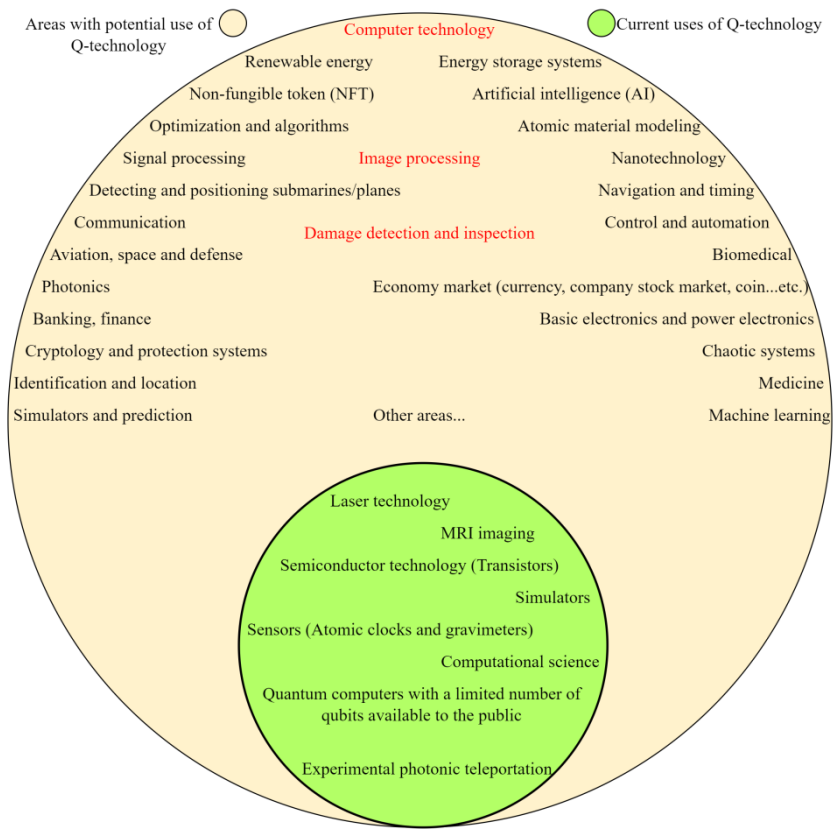
Figure 1. Areas where Q-technology is applied and Q-technology has potential to be used.

- Existing security protocols for communication that are robust against or entirely uncrackable by conventional means will become vulnerable to Q-computers.
- To eliminate the vulnerability, quantum cryptography is required.
- If an attempt at infiltration is discovered on the line, it may be possible to stop the flow of data.
- Thanks to quantum random number generators and quantum key distribution technologies, data can be encrypted in a way that prevents the deciphering without the key.
- It is possible to analyze a large amount of data in short time.
- Artificial intelligence (AI) and machine learning (ML) elements will become much smarter and faster to work, thanks to the speed of computation.
- High computing power can be achieved that enable the development of AI-supported systems with human-like capabilities.

- The speed of product creation will increase by providing faster solutions to the problems in the pharmaceutical industry based on the formula in which many parameters are included.
- With the rapid optimization calculations and algorithm studies by Q-computers, the processing times in air/land traffic will be shortened, and fluency in transportation will be ensured.
- It is foreseen that it will bring clarity and convenience to weather forecasting.
- It will play a role in quickly determining the right measures and taking the measures with the right methods regarding the modeled climate change.
- Q-technology supported computers provide speed and memory advantages by performing quantum bit (Q-bit or qubit) based operations, which handles all the problems at once, instead of existing computers that perform sequential operations.
- If cyber attacks get stronger, it may create national security problems.
- Thanks to Q-computers, which enable enormous amounts of information to be processed, companies' logistics/supply chains are expected to become more efficient and more resilient to disruptions.
- Nano-scale high spatial resolution and single-turn ultra-high detection sensitivity, which is applied to examine magnetic/superconducting materials, can be achieved, thanks to Q-technology.
- Q-technology creates new capabilities, efficiency, and precision for military applications. On the other hand, it necessitates the creation of new military strategies, doctrines, policies, and moral codes (Krelina, 2021).
- Q-technology provides speed and memory advantage for the analysis of multidimensional and multi-layered images. In addition, it creates an information security risk by decrypting encrypted private images.
- It ensures that image processing (IP) processes are carried out very quickly and in-depth.

The relationship between the mentioned advantages and disadvantages makes it necessary to work in the field of Q-technology. In this study, various IP-based detection and non-destructive testing methods (NDTM), which are in the electrical and electronics engineering fields of study, are investigated. The different usage areas of IP operations carried out with the help of Q-technology are examined. As a result, the aim is to prepare for the applications of advanced technology that will come strongly in the field of IP-based NDTM.

1. QUANTUM COMPUTERS

Q-computers integrate information technology with Q-mechanics, providing thousands of times the computing power of traditional computers (URL-5, 2023). In doing so, three principles of Q-mechanics are utilized:

- Superposition: One of the main phenomenas in Q-mechanics. It indicates that a quantum particle (Q-particle) can be in a state that is a superposition of all possible states until it is measured. Due to this phenomena, a manipulation to a state effects other states. This property allows doing multiple calculations on different states without breaking the superposition and enables the Q-computer to run parralel computations on a single bit. The manipulation is made by using quantum logic gates.

- Entanglement: It means that particles separated by great distances can be connected to each other and "detect" the state of others. In the context of Q-computing, stable and consistent predictions can be made from entangled Q-bits to develop conclusions about other Q-bits in the system. Considering situations like $|\Psi\rangle$ in Hilbert space, which can be written as $\mathcal{H}=\mathcal{H}A\otimes\mathcal{H}B$, if $|\Psi\rangle$ state $|a\rangle\in\mathcal{H}A$ and $|b\rangle\in\mathcal{H}B$ cannot be written as a tensor produce of two states, it is stated that $|\Psi\rangle$ state is entangled. The sum of properties such as position, momentum, and spin of two quantum entanglement particles is zero. If one spins clockwise, the other always spins counterclockwise.

- Interference: It is possible to direct an assigned Q-bit to a state or set of states whose measurement is desired. It represents the inner behavior of Q-bits. After the quantum logic gates manipulate the Q-bits' states, the interference pattern will be constructive between the desired states and destructive between the unwanted states. Upon measurement, the probabilty of the desired states to occur are higher than the unwanted ones. This states represents the solutions, and to reliablely obtain the desired solution, the operation may need to be performed more than once.

- In Q-technology, which is more comprehensive than the concept of Q-computer, there are some definitions that offer differences apart from the features mentioned above: Teleportation, superdense coding, reversible, non-cloning theorem, entanglement swapping (Candelon, 2022).

- Teleportation: It is the use of quantum entanglement and classical communication skills previously shared by the data source and the receiver during the movement of quantum information between locations. An example of a teleportation communication line is given in Figure 2.

- Superdense coding: It is the process of sending the information and content of two traditional bits using a Q-bit. This encoding requires entanglement in the form of Bell pairs like teleportation. An example superdense coding pipeline is given in Figure 3.
- Reversible: The initial state changes after an operation applied to a data state. After this change, the same process is repeated on the changed data, and the initial state is obtained ($U|\Psi\rangle=|\Psi'\rangle \rightarrow U-1|\Psi'\rangle=|\Psi\rangle$). This feature allows Q-computers to run operations below the Landauer Limit which states that an irreversible operation's energy cost cannot go below the energy calculated from Landauer's Principle, resulting with lesser heat emmissions and less energy consumption than conventional computers in principle.
- Non-cloning theorem: This theorem states that, copying a quantum objects superposition state into another one perfectly is impossible. While having imperfect copies are possible, this theorem makes superluminal communication impossible. This theorem also makes usage of classical error correction techniques impossible but other error correction methods are developed. In the Q-computer, the operators other than the measuring operator are unitary. Unity can be expressed as $(U*)T=U-1$.
- Entanglement swapping: The entanglement state is tradable (Chen et. al., 2018). Combinatorial entanglement between both systems X, Y, and Z can be transferred between other binary systems.
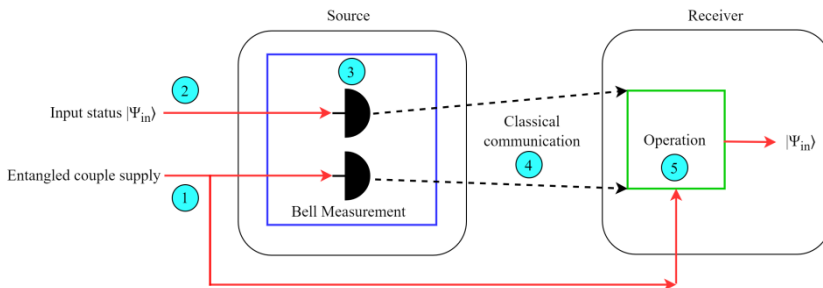
Figure 2. An instance teleportation communication line.
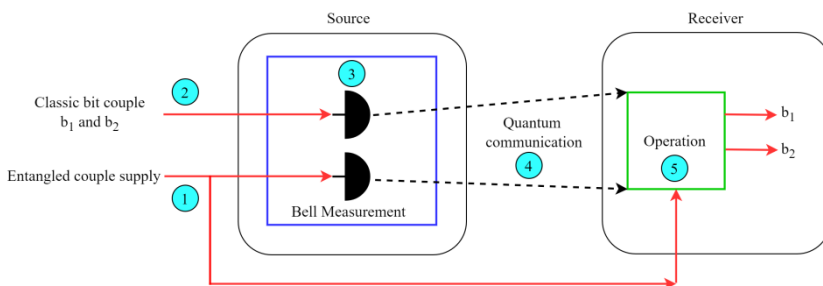
Figure 3. A sample of a superdense coding pipeline.

Data processing and data storage methods in computers in daily life are based on binary number systems consisting of 1s and 0s. Considering the situation that a particle can be in different states at the same time by making use of the concept of superposition in the field of physics, data storage systems in Q-technology can be both 1 and 0 at the same time, as seen in Figure 4 (Sahin, 2019). These particles, which can be both 1 and 0 at the same time, are called "Q-bits". In addition, thanks to the concept of "entanglement" in quantum physics, it can be used in semi-Q-bits that can take values as spaced as 0.15. The speed feature of quantum-based systems is qubit and semi-Q-bits. In some fields, such as photonics where Q-technology is used, the fact that a data unit can be 0 or 1 or both at the same time is expressed as "kutrit" (Zukowski, 1993; URL-6, 2023). Q-bits must be cooled to the absolute minimum temperature (or zero Kelvin) to control, manipulate, and use them. Because qubits are extremely sensitive to external influences. To deliver this degree of heat, a better cooling system must be accompanied by space studies (URL-7, 2023).
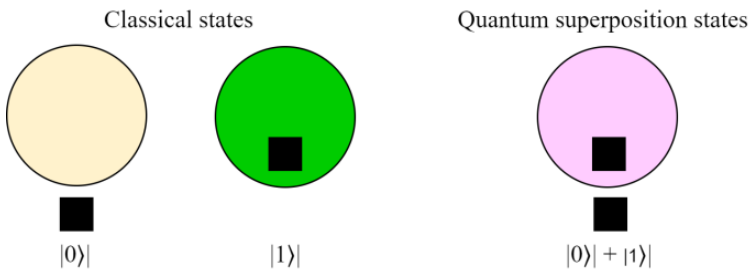
Figure 4. Data storage and data processing systems at Q-technology.

2. VARIOUS DEVELOPMENTS IN THE LITERATURE AND APPLICATIONS OF QUANTUM TECHNOLOGY IN IMAGE PROCESSING

Many topics in the field of digital image processing (DIP) were given shape in the 1960s at the Jet Propulsion Laboratory, the Massachusetts Institute of Technology, Bell Laboratories, the University of Maryland, and several other laboratories. In these laboratories, especially satellite imagery, medical imaging, sending images over telephone wires, sending video over telephone cables, character recognition, and image enhancement applications were made (URL-8, 2023). DIP is an important branch of technology and IP has entered daily life in many aspects:

- Image filters,
- Object detection in the image,

- Making different analyzes on the image,
- Image encryption,
- Image compression and steganography,
- Detections and analyzes made in the field of medicine,
- Error and damage detection…etc.

The obtained images should be processed with appropriate methods and serve the purpose of the study. In this context, in addition to IP, it is of great importance that the image is securely stored and delivered to the recipient. Especially high resolution and large size multi-wavelength images need memory to be analyzed. Therefore, the analysis of these images takes a long time. In such cases, classical computers can sometimes be insufficient. Multi-wavelength images can be processed faster and more effective work can be done, with Q-computers (Ball, 2021; Candelon, 2022). Quantum image processing (Q-IP) is the use of Q-computer technics to capture, process, and retrieve quantum images (Q-image) in different formats for various purposes. For processing the Q-image, firstly, the quantum form of the image and Q-image processing algorithms on this symbol are needed.

The first quantum revolution (Quantum 1.0) began at the beginning of the 20th century, when scientists came up with mathematical equations describing the structure of the atom and the quantum nature of electromagnetic fields. Result of the development of technologies such as transistor and laser, the way of the information and technology age has been opened [20]. In the second quantum revolution (Quantum 2.0) experienced at the beginning of the 21st century, groundbreaking technological developments began to be experienced with the use of quantum properties of particles, breaking the classical boundaries in computing, communication, metrology, sensors,imaging and etc. Some of the quantum-based studies in the literature for IP in this study are as follows: In studies carried out in 2003; various Q-image representation models have been proposed for storing and processing image information. The idea of "Qubit Lattice", a representation of the Q-image, has been introduced (Sahin & Yilmaz, 2018). In the studies in 2005; the idea of "Real Ket" was conveyed through image compression in the quantum context (Bohr, 1935).

In studies researched in 2010; the effects of the applied electric field on the isolated square quantum well have been researched with analytical and perturbative methods. The energy eigenvalues and wave functions in the quantum well have been found by perturbative way. Electric field effects have been analyzed by analytical process. The outcomes of the perturbative and analytical method have been compared. It has been monitored that the externally applied electric field significantly changes the electronic features of

the system (Andraca & Bose, 2003). Another study proposes the idea of an "Entangled Image" using entangled Q-bits (Latorre, 2005). In 2011; a elastic representation model of Q-images for Q-computers is presented. The hue and position information is kept in the form of a normalized quantum case for the quantum shape of images. The goal is to represent images with grayscales quantumly. Color information is collected in a quantum state, similar to pixels that provide information about the dimensions of the image in current computers (Bahar & Ersoy, 2010). In 2012; Q-image watermarking and authentication algorithm using flip and transposition procedures is developed to generate a watermark map and give the map-based watermark circuit (Andraca & Ball, 2010). In another study conducted in the same year, Q-computing applications are being researched in the IP field. Demonstrates how operations can be disclosed using quantum form to study fundamental gray grade transformations such as image negatives, binaryizing images, detecting histogram plots of images, histogram computation, and histogram equalization. In addition, Q-computing-based IP is compared with its classical competitors and their superiority is determined (Le et. al., 2011). In 2013; a novel advanced quantum impression model of digital images has been developed that uses the fundamental base states of a Q-bit array instead of the probability amplitude of one Q-bit to store the grayscale values of each pixel. A watermark scheme is proposed for Q-images (Iliyasu et. al., 2012). In other study; a flexible representation model of Q-images has been developed and a Red-Green-Blue (RGB) model for the representation of three-channel Q-images has been proposed (Caraiman & Manta, 2012). In another study conducted in the same year; a new dynamic watermark diagram for Q-images has been studied using quantum wavelet transform (Zhang et. al. 2013). Moreover, Q-image encryption and decryption algorithms based on geometric transmutations of Q-images are presented (Sun et. al., 2013). In studies done in 2014; A unique 8-bit Kogge-Stone summation circuit working with the wave pipeline method has been designed. And, original logic blocks such as the full adder logic block used in the circuit have been designed. The circuit parameters of the designed blocks have been optimized using the particle swarm optimization (PSO) tool. It is aimed to rise the performance of the collection circuit. Improvements have been made using the statistical timing analysis tool to enhance the efficiency and operating tolerance of the completed collector circuit. An 8-bit Kogge-Stone adder circuit has been designed with a target frequency of 25 GHz and consists of 6581 Josephson Junctions (Song et. al., 2013). In other study conducted in the same year; a easyy quantum form of infrared pictures is presented using the "Qubit Lattice" and flexible representation techniques of Q-images. During these processes, the radiation energy of the objects has been converted into a quantum state (Zhou et. al., 2013). In another study; a model is proposed for the quantum representation of three-dimensional (3D) images (Ozer, 2014).

In scientific studies conducted in 2015; the experiment conducted by the National Institute of Standards and Technology has been aimed to communicate at the speed of light. Contrary to moving objects and materials at the speed of light, the aim has been achieved with the transmission speed of the information carried. In the related experiment, concepts of quantum technology such as entanglement has been used (Yuan et. al., 2014). In another study conducted in the same year; Q-image encryption algorithm based on image correlation decomposition is presented (Li et. al., 2014). In 2016; a new quantum grayscale image watergram protocol is proposed using small-scale quantum circuits. In the related work, the 8-bit gray scale image size (nn×nn) has been enlarged to the 2-bit gray scale image size (2nn×2nn). After that, the expanded image is scrambled to be meaningless by portals controlled by keys known only to the operator. The scrambled image is embedded in the carrier image by other attendant gates (Shalm et. al., 2015). In 2017; A fresh advanced quantum form model of digital displays has been developed and a model for the representation of RGB three-channel color Q-images has been introduced (Hua et. al., 2015). In 2019; The advantages of Q-computing on IP have been investigated by revealing its superior features. A quantum projection model of multi-wavelength images (QRMW) is presented for Q-IP. The preparation of quantum states and the recovery of the image from the quantum situation are explained in the QRMW model. Compression way is recommended for images in the QRMW model. A steganography algorithm is proposed to cover up text and binary image hidden knowledge in a Q-image in the QRMW model. It is shown how the secret information is hidden from the carrier image and how they are extracted from the carrier image, in the steganography algorithm (Candelon et. al., 2022).

In the studies carried out in 2020; a Q-IP algorithm has been improved using the border extraction technique together with the Kirsch operator. Q-image representation model is used to process the Q-image. It has been observed that the studied algorithm completes real-time IP processing with high accuracy (Miyake & Nakame, 2016). Many papers attempt to define quantum presentments based on very big superposition conditions, covering as many terms as the number of pixels in the picture being represented. This process provides advantages in terms of space depending on the number of Q-bits used, and in terms of processing speed due to quantum parallelism. On the other hand, bottleneck occurs when only one pixel can be recovered from the quantum form of the entire image. The economic cost between classical IP and Q-IP is being investigated (Abdolmaleky et. al., 2017). In 2021; Q-computers that can be used in the field of IP and AI are classified and compared (Xu et. al., 2020). Suspicion and manipulations in the field of Q-IP have been investigated (Nagy & Nagy, 2020). In 2022; it is aimed to process images in a quantum environment in parallel in AI-based research. For the proposed quantum data coding method for the optimized coding of large data

such as images, an application has been made on a 4x4 sample image with 4-bit resolution. Compared to traditional methods, 57% better results have been achieved (Yetis, 2022). In 2023; by utilizing unique spatial and temporal quantum correlations, Q-imaging has been studied to develop parameters including modulation transfer function. Application processes of photonic Q-imaging level have been investigated to obtain an improved imaging system (Yetis & Karakoes, 2021).

Although most of the studies in the literature present quantum image presentments for one or tricolor (RGB) images, studies on all wavelengths have started to emerge in recent years. Since the importance of IP is known in today's studies, various applications are aimed in areas such as detection and tracking over satellite, military target determination, control in total quality management, laboratory applications in medicine and biophysics, and non-destructive testing methods by using the advantages of quantum technology, especially on multi-wavelength images. Considering the events that have developed over the years in Q-technology, it is seen that the investments and researches made in this direction have increased rapidly, especially since 2020. According to the analysis of Boston Consulting Group, the market in the field of Q-technology is expected to increase in value of 850 billion USD between 2036 and 2051 (Ruan et. al., 2021; Kuniyil, 2023).

3. ELECTRIC-ELECTRONIC BASED DETECTION AND NON-DESTRUCTIVE INSPECTION METHODS

Non-destructive testing (NDT): It provides the detection of damages and errors in the internal/external structure of the material or materials. The tests that allow the inspection of the sample without affecting the service for the purpose of production or use, without impairing its properties and without damaging it are called non-destructive testing methods (NDTM). NDTM is important for production efficiency, use efficiency, safety, and quality. NDTMs can be classified as in Figure 5:
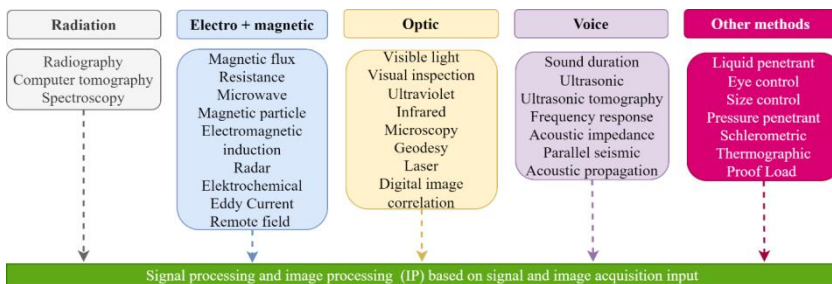

Figure 5. Non-destructive testing methods.

IP which is used in the field of non-contact and non-destructive testing and is the subject of this study, is used for visual inspection and testing of components/assemblies. In addition to the monitoring of production processes, automatic control and supervision of individual production stages can also be provided. In other words, it is ideal for assuring, monitoring and documenting both production and product quality. Quantum theory has been studied for many years in some areas of NDT and this theory has been used. Some of the first examples that come to mind include:

- Quantum-tunneling (electron microscobe),

- Quantitative radiation (MRI),

- X-ray,

- Computed tomography (CT) (IAEA, 2020),

- Superconducting quantum interference device (SQUID) (Kojima & Kasai, 2000; Sternickel & Braginski, 2006).

Current applications in industry and scientific studies in recent years can be exemplified as follows: In 2010; quantum dots (Q-dot) used as fluorescent dye penetrating have been used to detect damages greater than or equal to 5 μm at weld joints. Laser technology was used in the analysis phase of the study (Daneshvar & Dogan, 2010). In 2019; NDTMs has not provided the desired performance to detect errors and damages caused by micro-sized composite bonding in the production of materials used in electrical networks. Therefore, new quantum-based ways have been proposed (Wang et. al., 2019). In 2020; quantum-based study has been done to detect typos in written texts. Auxiliary Q-bits are used to collect the information in the Q-bits. It has been stated how the principles in Sectin 2 have been used while conducting the related study. In the light of the data obtained from the experimental consequences, the proposed method has increased the success rate for various quantum algorithms and has proven to be effective in debugging (Liu et. al., 2020). In 2022; different algorithms and methods have been studied for the detection of waveguide defects and dirt using automatic optical inspection and deep learning (DL). For the classification of images obtained by the quantum cascade laser, an advanced capsule neural network (WaferCaps) and convolutional neural network (CNN) based on parallel determination fusion is used to classify the examples (Ebayyeh et. al., 2022). In 2023; the latest advances in sensor technologies have been utilized for NDT of civil structures and structural health monitoring. Information on sensing methods like as fiber optics, laser vibrometry, acoustic emission, ultrasonic, thermography, drones, microelectromechanical systems, magnetostrictive sensors, and new generation technologies is given. In addition, information about Nano-SQUID type sensors that evaluate the magnetic characteristics of atoms at the

quantum level, quantum sensors for magnetic field measurement, quantum infrared sensors, and their advantages are given (Hassani & Dackermann, 2023). In a different study conducted in the same year; it has been noted that damage detection at sizes below 100 μm is often difficult to make. Service life can be increased by controlling these defects and ensuring safe use. As a result of this, a positive contribution is made to the field of circular economy and sustainability. NDTs are combined with ML and signal processing techniques. Promising techniques such as thresholds and Q-dots of NDTs have been explored (Silva et. al., 2023). In another study; the 3D range-migration algorithm used in radar-based NDTMs and the omega-k algorithm that is the 2D equivalent of this algorithm, have been run on a conventional computer, a Q-computer simulator, and a real Q-computer for data processing (DP) purposes (Waller et. al., 2023). As it can be understood from the information given so far, there is an expectation that Q-computers is going to break new ground in the field of Q-IP, IP and Q-DP, DP-based NDTM.

4. CONCLUSION

This study, which is prepared on quantum studies, that is one of the technological methods of the future, can be summarized as follows: Firstly, information about quantum technologies and principles are given. Current uses and potential future uses of quantum technology are described. Afterwards, detailed information about quantum computers and their principles are given. The developments in the literature on quantum image processing, which is the focus of the study, are exemplified. Finally, the study has been completed by giving information about non-destructive testing methods and the potential of quantum image processing in this field.

Quantum computers are promising for different fields and current image processing methods that need high computational power. On the other hand, it raises concerns about what kind of information people or nations who have this technological power can access. Considering the reliability of the encryption methods used and the area of use in the field of image processing, the speed of decryption of images becomes a matter of debate. Moreover, it is predicted that the combination of artificial intelligence and quantum technology will create a groundbreaking power.

In the field of nondestructive testing, there are currently ongoing studies and algorithms under development to overcome the deficiencies of quantum-based methods. However, the fact that the qubit numbers of the quantum computers in which the images are processed have not yet reached the desired levels and that these devices cannot be open to the public (such as personal computers) is seen as the main problem. In addition, the existing bottlenecks are that the quantum gates that enable rotation and transform

operations on the image are not flexible enough, alternatives have not been determined yet, and the quantum integration state, which is one of the fundemental features of quantum computing, decays faster than desired.

As a result, even basic image and signal processing studies used for non-destructive testing are home to many vulnerabilities. On the other hand, non-destructive testing methods used with the help of quantum image processing technique constitute a special and advanced study area. Being ready in this field now will allow to be ready when the future comes. It is clear that the studies planned on this subject will directly contribute to the young literature.

REFERENCES

Abdolmaleky, M., Naseri, M., Batle, J., Farouk, A., Gong, L.H. (2017). Red-green-blue multi-channel quantum representation of digital images. Optic, 128, 121-132.

Andraca, S.E.V., Ball, J.L. (2010). Processing images in entangled quantum systems. Quantum Information Processing, 9(1), 1-11.

Andraca, S.E.V., Bose, S. (2003). Storing, processing and retrieving an image using quantum mechanics. Quantum Information and Computation, 5105: 137-147.

Bahar, M.K., Ersoy, A. (2010). Investigation by perturbative and analytical method of electronic properties of square quantum well under electric field. Sakarya University Journal of Science, 14(2), 55-61.

Ball, P. (2021). First quantum computer to pack 100 qubits enters crowded race. Nature, 599, 7886, 542-542.

Bohr, N. (1935). Can quantum-mechanical description of physical reality be considered complete?. Phys. Rev., 48, 696.

Candelon, F., Bobier, J. F., Courtaux, M., Nahas, G. (2022). Can Europe catch up with the US (and China) in quantum computing. BCG Henderson Institute, Report.

Caraiman, S., Manta, V. (2012). Image processing using quantum computing. IEEE 16th International Conference on System Theory, Control and Computing.

Chen, Z.Y., Zhou, Q., Xue, C., Yang, X., Guo, G.C., Guo, G.P. (2018). 64-qubit quantum circuit simulation. Science Bulletin, 63(15), 964-971.

Daneshvar, K., Dogan, B. (2010). Application of quantum dots as a fluorescent-penetrant for weld crack detection. Mater High Temperatures, 27(3), 179-82.

Dincer, S. (2009). Drawing two dimensional images using digital image processing algorithms by the help of Matlab and a microcontroller. Istanbul Technical University, Master Thesis.

Ebayyeh, A.A.R.M.A., Mousavi, A., Danishva, S., Blase, S., Gresch, T., Landry, O., Müller, A. (2022). Waveguide quality inspection in quantum cascade lasers: A capsule neural network approach. Expert Systems With Applications, 210, 118421.

Gell-Mann, M. (1979). The nature of the physical universe. Nobel Conference.

Goyal, P., Knuth, K.H., Skilling, J. (2009). The origin of complex quantum amplitudes, AIP Conference Proceedings,1193, 89-96.

Hassani, S., Dackermann, U. (2023). A systematic review of advanced sensor technologies for non-destructive testing and structural health monitoring. Sensors, 23, 2204.

Hempel, C., Maier, C., Romero, J., McClean, J.i et al. (2018). Quantum chemistry calculations on a trapped-ion quantum simulator. Physical Review, 031022, 8(3), 1-22.

Hua, T., Chen, J., Pei, D., Zhang, W., Zhou, N. (2015). Quantum image encryption algorithm based on image correlation decomposition. International Journal of Theoretical Physics, 54(2), 526-537.

IAEA (International Atomic Energy Agency). (2020). An Introduction to practical industrial tomography techniques for non-destructive testing (NDT)., IAEA-TECDOC-1931.

Iliyasu, A., Le, P., Dong, F., Hirota, K. (2012). Watermarking and authentication of quantum images based on restricted geometric transformations. Information Sciences, 186(1), 126-149.

Kaptan, K. (2017). The interpretation of quantum theory and role of nature. Journal of Applied Sciences of Mehmet Akif Ersoy University, 1(1), 19-28.

Krelina, M. (2021). Quantum technology for military applications. EPJ Quantum Technology, 8(24), 1-53.

Kuniyil, H.P. (2023). Quantum advances in imaging systems. Ozyeğin University, PhD Thesis, p. 123.

Kojima, F., Kasai, N. (2000). Data recovering techniques for superconducting quantum interference device and its application to nondestructive evaluation. AIP Conference Proceedings, 509(1), 1955-1962.

Latorre, J.I. (2005). Image compression and entanglement. Quantum Physics.

Le, P.Q., Dong, F., Hirota, K. (2011). A flexible representation of quantum images for polynomial preparation, image compression, and processing operations. Quantum Information Processing, 10(1): 63-84.

Li, H., Zhu, Q., Zhou, R., Song, L., Yang, X. (2014). Multi-dimensional color image storage and retrieval for a normal arbitrary quantum superposition state. Quantum Information Processing, 13(4): 991-1011.

Liu, J., Byrd, G.T., Zhou, H. (2020). Quantum circuits for dynamic runtime assertions in quantum computation, 25th International Conference on Architectural Support for Programming Languages and Operating Systems, 1017-1030.

Miyake, S., Nakamae, K. (2016). A quantum watermarking scheme using simple and small-scale quantum circuits. Quantum Information Processing, 15(5), 1849-1864.

Nagy, M., Nagy, N. (2020). Image processing: Why quantum?. Quantum Information and Computation, 20(7), 616-626.

Ozer, M. (2014). Design of an RSFQ asynchronous pipelined kogge-stone adder and developing custom compound gates. TOBB Economics and Technology University, Master Thesis, 53.

Ruan, Y., Xue, X., Shen, Y. (2021). Quantum image processing: Opportunities and challenges. Mathematical Problems in Engineering, 8.

Sahin, E. (2019). Image processing based on fundamental of quantum. Çanakkale Onsekiz Mart University, PhD Thesis, p. 86.

Sahin, E., Yılmaz, İ. (2018). QRMW: quantum representation of multi wavelength images. Turkish Journal of Electrical Engineering and Computer Sciences, 26(2), 768-779.

Shalm, L.K., Scott, E.M., Christensen, B.G., et al. (2015). Strong loophole-free test of local realism. Physical Review Letters, 115, 250402.

Silva, M.I., Malitckii, E., Santos, T.G., Vilaça, P. (2023). Review of conventional and advanced non-destructive testing techniques for detection and characterization of small-scale defects. Progress in Materials Science, 138, 101155.

Sternickel, K., Braginski, A.I. (2006). Biomagnetism using SQUIDs: Status and perspectives. Superconductor Science and Technology, 19(3), 160.

Song, X., Wang, S., Liu, S., Abd El-Latif, A., Niu, X. (2013). A dynamic watermarking scheme for quantum images using quantum wavelet transform. Quantum Information Processing, 12(12), 3689-3706.

Sun, B., Iliyasu, A., Yan, F., Hirota, K. (2013). An RGB multi-channel representation for images on quantum computers. Journal of Advanced Computational Intelligence and Intelligent Informatics, 17(3), 404-417.

URL-1: https://www.nato.int/docu/review/articles/2021/06/03/quantum-technologies-in-defence-security/index.html, (Access date: June 2023).

URL-2: https://www.scientificamerican.com/article/quantum-sensors-could-let-autonomous-cars-see-around-corners/, (Access date: July 2023).

URL-3: https://github.com/Strilanc/Quirk, (Access date: July 2023).

URL-4: https://www.ibm.com/quantum, (Access date: July 2023).

URL-5: https://www.bcg.com/publications/2021/building-quantum-advantage, (Access date: July 2023).

URL-6: https://www.nanoqtech.eu/quantum-technologies, (Access date: July 2023).

URL-7: https://thinktech.stm.com.tr/uploads/docs/1608824731_stm-blog-kuantum-isinlanmada-ucuncu-boyut.pdf?, (Access date: July 2023).

URL-8: https://www.independent.co.uk/tech/quantum-teleportation-breakthrough-third-dimension-a9075476.html, (Access date: July 2023).

Waller, E.H., Keil, A., Friederich, F. (2023). Quantum range-migration-algorithm for synthetic aperture radar applications. Scientific Reports, 13, 11436.

Wang, H., Cheng, L., Liao, R., Zhang, S., Yang, L. (2019). Non-destructive testing method of micro-debonding defects in composite insulation based on high power ultrasonic. High Voltage, 4(3), 167-172.

Xu, P., He, Z., Qiu, T., Ma, H. (2020). Quantum image processing algorithm using edge extraction based on Kirsch operator. Optic Express, 28(9), 12508-12517.

Yetis, H. (2022). Development of quantum computation based artificial intelligence algorithms. Fırat University, PhD Thesis, 157.

Yetis, H., Karakoes, M. (2021). Investigation of noise effects for different quantum computing architectures in IBM-Q at NISQ level. IEEE 25th International Conference on Information Technology.

Yuan, S., Mao, X., Xue, Y., Chen, L., Xiong, Q., Compare, A. (2014). SQR: A Simple Quantum Representation of Infrared Images. Quantum Information Processing, 13(6), 1353-1379.

Zhang, W.W., Gao, F., Liu, B., Hia, H.Y., Wen, Q.Y., Chen, H. (2013). A quantum watermark protocol. International Journal of Theoretical Physics, 52(2), 504-513.

Zhou, R.G., Wu, Q., Zhang, M.Q. (2013). Quantum image encryption and decryption algorithms based on quantum image geometric transformations. International Journal of Theoretical Physics, 52(6), 1802-1817.

Zukowski, M., Zeilinger, A., Horne, M.A., Ekert, A.K. (1993). Event-ready-detectors, Bell experiment via entanglement swapping. Phys. Rev. Lett., 71, 4287.

CHAPTER 5

SYNTHESIS OF SILVER NANOPARTICLES

Assoc. Prof. Dr. Sevil AKÇAĞLAR[1]

DOI: https://dx.doi.org/10.5281/zenodo.10447855

[1] Dokuz Eylül Üniversitesi, Mühendislik Fakültesi, Makine Mühendisliği Bölümü İzmir, Türkiye. sevil.akcaglar@deu.edu.tr, Orcid ID: 0000-0002-5386-1862

INTRODUCTION

Nanoscience has recently been recognized as a completely broad and new branch of science. It can be defined as information describing the most important properties of nano-sized objects. The results of nanoscience have led to the creation of new materials and useful facilities based on nanotechnology. Recently, nanochemistry is one of the constantly developing topics for nanoscience (Sergeev and Shabatina, 2008). Because of their high surface-to-volume ratio, metallic particles at the nanoscale seem to have largely different physical, chemical, and biological properties from their macroscale counterparts. As a result, these nanoparticles have been regularly employed in significant current research (Huang and Yang, 2008). The size- and shape-dependent characteristics of metallic nanoparticles have been investigated for key applications such data storage, antimicrobial activity, and catalysts and optics. (Choi and associates, 2007) For instance, different metal nanoparticles, such silver colloids, have antibacterial activity that is nearly proportional to their size; that is, the smaller the silver nuclei, the greater the antibacterial activity.

In addition, the catalytic activity of these nanoparticles depends on their shape, structure, chemical-physical environment and size distribution, as well as their size. Hence, control over the size and size distributing, is a significant function. Mainly, specific control of shape, size, and size distributing, is often obtained by altering stabilizers, the synthesis methods and reducing agents (Zhang et al., 2008). Metal nanoparticles can be introduced by two routes; the first is physical applications using various methods such as laser ablation and evaporation/condensation. The second is a chemical process where the number of metal ions in solution decreases under conditions forming small metal aggregates or groups (Oliveira et al., 2005). Chemical processes can be divided into two categories: those that work in reverse micellar systems, where the collecting process takes place in the aqueous core of inverse micelles and growing particles are enclosed by the surfactant particles, and those that use naturally occurring slimming agents like polysaccharides or plant extract, or that use biological microorganisms like fungus and bacteria as reductants. Stabilization of nanoparticles is typically discussed in terms of two stabilization categories: steric and electrostatic. Coordination of anionic forms, such as halides, carboxylates, or polyoxoanions, with metal particles results in electrostatic stabilization.

1. SYNTHESIS OF SILVER NANOPARTICLES

a. *Physical Approach*

Evaporation-condensation is the typical physical method used for generating metal nanoparticles, and it can be done in a tube furnace at room pressure. A carrier gas is generated when the source material in a vessel

concentrated in the furnace evaporates. A variety of materials, including Ag, Au, Pb, S, and fullerene, were previously produced as nanoparticles via the vaporization/condensation process (Zhang, Xi-F, et al., 2016)

The properties of the metal small particles composed and the ablation yield heavy subject to many factors such as the wavelength of the laser striking the metallic target, the period of the laser impact the laser fluency, the ablation time and the efficient fluid middle, without or with the entity of surfactants (Tarasenko et al., 2006; Kawasaki and Nishimura, 2008) nanoparticles can be altered in dimension and form owing to, their more distant interactivity with the laser beam going via (Mahfouz et al., 2008). Furthermore, the surfactant layer completes the shape of the nanoparticles created by laser ablation. Compared to those formed in a solution with weak surfactant condensation, the nanoparticles constructed in an enhanced surfactant condensation resolution are smaller (Table 1) (Mafune et al., 2001).

Table 1. Physical and chemical syntheses of silver nanoparticles

Type	Reducing agent
Polydiallyldimethylammonium chloride and polymethacrylic acid capped silver nanoparticles	Methacrylic acid po
Silver nanoparticles	Ascorbic acid
Chitosan-loaded silver nanoparticles	Polysaccharide chit
Silver nanoparticles	Hydrazine, D-glucos
PVP-coated silver nanoparticles	Sodium borohydrid

b. Chemical Proses

The bulk of the time, chemical decrease is the most practicable method for distributing AgNPs steadily and colloidally in liquid organic solvents like water. Elements such as hydrogen, borohydride, citrate, and ascorbate are often utilised in reductive processes. Colloidal silver with varying nanometer particle widths is often produced by reducing silver ions (Ag+) at watery solubility.

Silver particles (AgO) are formed when various complexes containing Ag+ ions diminish; this process is furthered by the accumulation of AgO in oligomeric piles. Eventually, colloidal Ag particles will develop and cause these piles. (Tao and others, 2006). Using protective agents to distribute nanoparticles evenly along the metal nanoparticle delivery route is important. The general recommendation is to prevent the aggregation of the nanoparticles by preserving them with protective representatives that can attach to or absorb onto their surface (Libo Wu et al., 2011).

The more prevalent used polymers are poly (ethylene glycol) (PEG), poly (vinylpyrrolidone) (PVP), polymethylmethacrylate (PMMA), poly (methacrylic acid) (PMAA). (Mallesh K. and G.S.N. Koteswara R., 2020). If the molar ratio of silver and gold in the feed increases, the size of the particles decreases and metallic nanoparticles with a much narrower distribution can be formed (Zhang et al., 2008). If the molar ratio of silver and gold in the feed increases, the size of the particles decreases and metallic nanoparticles with a much narrower dispersion can be formed.

For instance, colloid nanoparticles present in non-aqueous medium for delivery of inks disperse well in a weak steam compression organic solvent to readily watery the surface of the polymeric substrate without any agglomeration.

Lately, biosynthetic methods making innately, emerging representatives such as polysaccharides, i.e. green chemistry, biological microorganism such as bacteria and fungus or plants remove, have appeared as a basic and utilizable other to mix chemical synthetically processes, to provide AgNPs (Table 2) (Taiki M. et al., 2021).

**Table 2.** Chemical methods for the synthesis silver nanoparticles

Reducing agent	Precursor agent	Capping agent	Experimental conditions
Trisodium citrate	Silver nitrate	Trisodium citrate	Diameter ≈ 10–80 nm; temperature ≈ boili
Ascorbic acid	Silver nitrate	Daxad 19	Diameter ≈ 15–26 nm; temperature ≈ boilir
Alanine/NaOH	Silver nitrate	DBSA (dodecylbenzenesulfonic acid)	Diameter ≈ 8.9 nm; temperature ≈ 90°C; ti
Ascorbic acid	Silver nitrate	Glycerol/PVP	Diameter ≈ 20–100 nm; temperature ≈ 90'
Oleic acid	Silver nitrate	Sodium oleate	Diameter ≈ 5–100 nm; temperature ≈ 100–
Trisodium citrate	Silver nitrate	Trisodium citrate	Diameter ≈ 30–96 nm; temperature ≈ boili
Trisodium citrate	Silver nitrate	Trisodium citrate/Tannic acid	Diameter ≈ 10–100 nm; temperature ≈ 90°

c. Biological Approach

The production of silver nanoparticles through chemical and physical applications requires a long time, is costly, and is harmful to the environment.

Therefore, it is of great importance to improve an environmentally and economically friendly method that does not include toxicant chemicals and removes another difficulties related to physical and chemical manufacture instruments (Iravani S., 2014).

According to reports, the use of microbes and plants in the manufacturing of nanoparticles is safe, cost-effective, and environmentally less hazardous than chemical synthesis Figure1 (Gowramma B. et al., 2015).
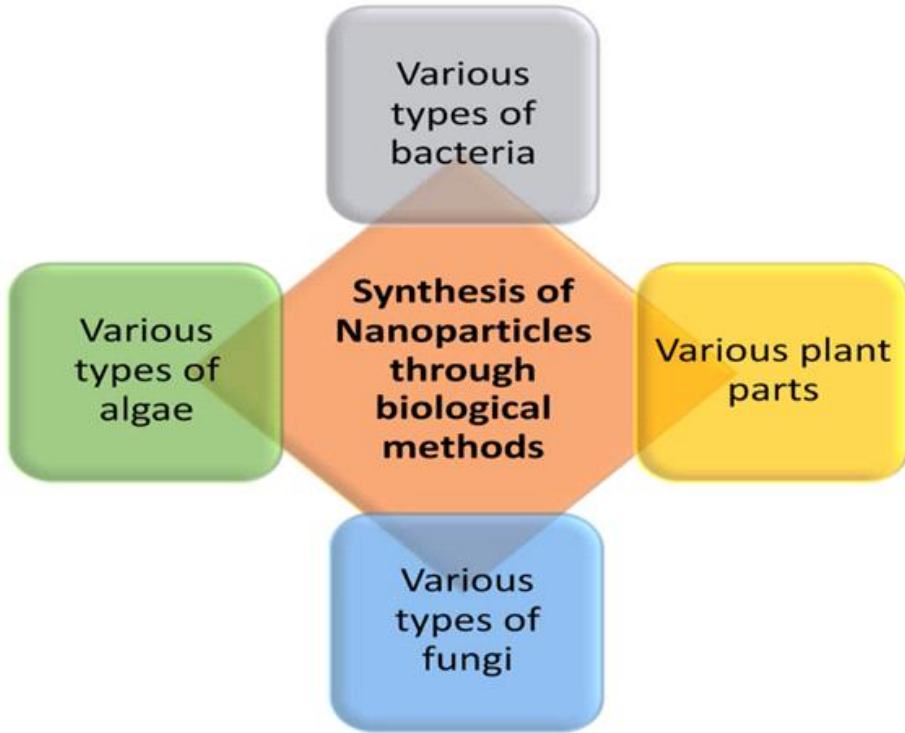
Figure 1. Dissimilar biological procedures for the process of silver nanoparticles

2. CHARACTERIZATION OF SILVER NANOPARTICLES

To identify and validate nanoparticle processes and methodologies, it is important to understand their description. Many techniques, including scanning and transmission electron microscopy (SEM, TEM), dynamic light scattering (DLS), atomic force microscopy (AFM), powder X-ray diffractometer (XRD), Fourier transform infrared spectroscopy (FTIR), X-ray photoelectron spectroscopy (XPS), and UV–Vis spectroscopy, are used in the process of characterization Figure 2 (Mohammad S, Havza I, Ameer A., & Shamsul H. et al., 2023). These processes are used to define many parameters such as particle dimension, form, crystallinity, fractal size, pore size and surface area. Besides, Compatibility, distribution and intercalation of nanoparticles Nanotubes in nanocomposite particulate materials can be with these are transactions.
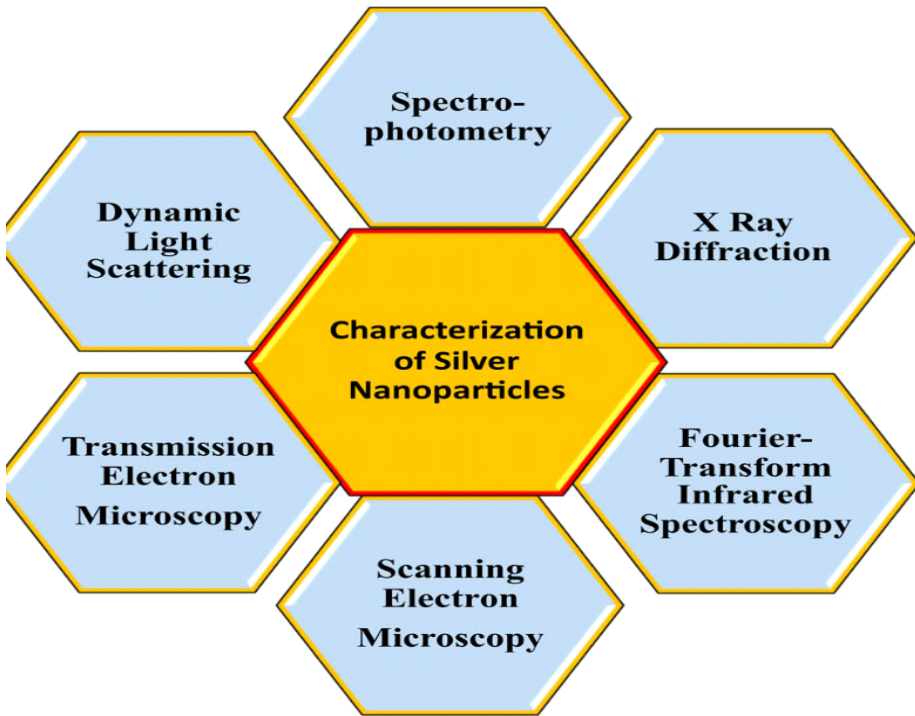
Figure 2. Techniques used for characterization of silver nanoparticles

3. IMPLEMENTATIONS AREAS OF SILVER NANOPARTICLES

AgNPs are widely used as anti-bacterial agents in many healthcare industries, food storage, textile coatings, and environmental applications. Although silver has been used in a wide range of areas for many years, information about its toxicity is still unclear. There are many areas where silver nanoparticles are present, such as antimicrobial, ant biofilm, antifouling, ant parasite, anticancer, drug delivery chain and antiviral. The broad application areas of silver nanoparticles are listed in Figure 3.

AgNPs are widely used as anti-bacterial agents. The most common of these are water purification and sterilization of medical equipment and household appliances (Table 3) (Tamara. B., Francisca M.-B., et al., 2021; Li et al., 2008)

If we consider the optical properties of a metallic nanoparticle, they are mostly based directly on the surface Plasmon resonance. This means that

Plasmon uses the collective oscillation of free electrons present within the metallic nanoparticle.

Table 3. The use of silver nanoparticles in many industries

Industry/applications	Uses of silver nanoparticles
Pharmacological uses	Larvicidal
	Antimicrobial
	Wound healing
Textile	UV-ray blocking
	Medicinal devices and textiles
Water treatment	Potable water
	Ground water disinfection
	Wastewater disinfection
Biomedical industry	Antiviral
	Antibacterial
	Anti-inflammatory
	Antifungal
	Anticancer
Food industry	Food processing
	Food packaging
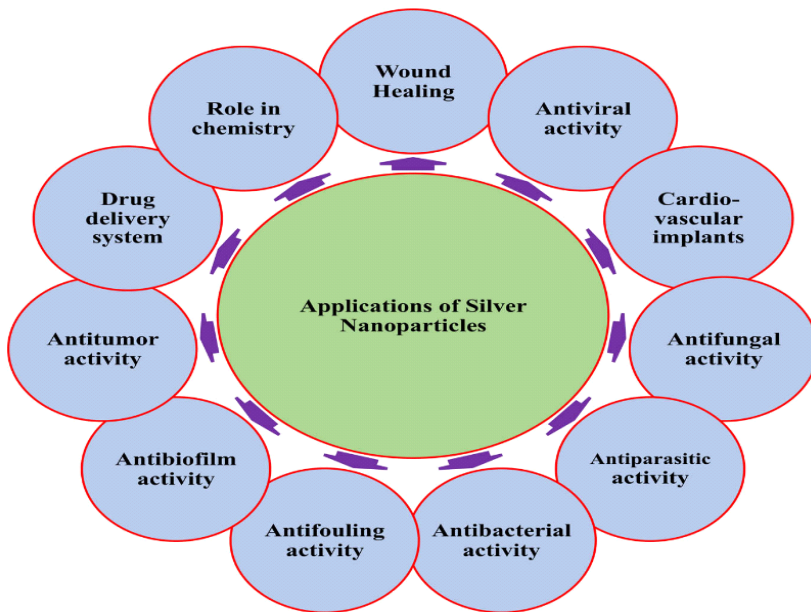
Figure 3. Implementations of silver nanoparticles

CONCLUSIONS

In the last decade, nanoparticles of metals like silver have been recognized with physical, chemical, and biological qualities that vary importantly from their major similar. Nano sized Particles small-scale than 100 nm in diameter are now, it is utilized in several points of industry areas small-scale particle size and high surface area be different seriously from materials, which are the majority significant characteristics of these powders. One of the good things about using nanoparticles is that they are nanosized particles, but another good feature is that the particles can also be irregular without clumping.

Academic studies conducted over the last 10 years clearly show that the optical, electromagnetic and even catalytic aspects of silver nanoparticles are greatly affected by their shape, size and proportion, which generally vary with reducing agents, synthetic methods, and stabilizers. Varied methods for the preparation of silver nanoparticles and implementations of these nanoparticles in disparate areas are introduced.

REFERENCES

Gowramma B, Keerthi U, Rafi M, Rao DM. 2015 Biotech. 2015;5:195–201.

Iravani S. Bacteria in nanoparticle synthesis: current status and future prospects. Int Scholar Res Not. 2014:359316.

Kawasaki, M., Nishimura, N., 2006. Appl. Surf. Sci. 253, 2008

Li, Q., Mahendra, S., Lyon, D., Brunet, L., Liga, M., Li, D., Alvarez, P., 2008. Water Res. 42, 4591

Libo Wu, Jian Zhang, Wiwik Watanabe., 2011. Advanced Drug Delivery Reviews, 63, 456-469

Mahfouz, R., Aires, F., Brenier, A., Jacquier, B., Bertolini, J., 2008. Appl. Surf. Sci. 254, 5181.

Mallesh Kurakulaa,* and G.S.N. Koteswara R.,2020 J Drug Deliv Sci Technol. 60: 102046.

Mohammad S, Havza I, Ameer A., & Shamsul H.,2023. Biometals, doi: 10.1007/s10534-023-00542-5. Online

Oliveira, M., Ugarte, D., Zanchet, D., Zarbin, A., 2005. J. Colloid Interface Sci. 292, 429

Sergeev, G., Shabatina, T., 2008. Colloids Surf. A: Physicochem. Eng. Aspects 313, 18

Huang, H., Yang, Y., 2008. Compos. Sci. Technol. 68, 2948

Taiki, M., Mayuko I.,Gregor .C .B., Kiyotaka N., and Teruo M.Int J Nanomedicine. ; 16: 3937–3999.

Tamara. B., Francisca M-B., Paul. J., Nelson. C., 2021 Int J Mol Sci.4;22,7202

Tao, A., Sinsermsuksaku, P., Yang, P., 2006. Angew. Chem. Int. 45, 4597

Tarasenko, N., Butsen, A., Nevar, E., Savastenko, N., 2006. Appl. Surf. Sci. 252, 4439.

Zhang, Y., Peng, H., Huang, W., Zhou, Y., Yan, D., 2008. J. Colloid Interface Sci. 325, 371.

Zhang, Xi-F.,Liu, Zi-G., Shen, W.,Gurunathan, S. 2016. International Jl of Mol. Sci, 17, 1534.

CHAPTER 6

TREATMENT OF POLYAROMATIC HYDROCARBONS (PAHs) FROM SURFACE WATER USING ZnO/Na$_2$S$_2$O$_8$ NANOCOMPOSITE UNDER SUNLIGHT IRRADIATION

Assoc. Prof. Dr. Sevil AKÇAĞLAR[1]

[1] Dokuz Eylül Üniversitesi, Mühendislik Fakültesi, Makine Mühendisliği Bölümü İzmir, Türkiye, sevil.akcaglar@deu.edu.tr, Orcid ID: 0000-0002-5386-1862

INTRODUCTION

Surface water ratio was 98% of the fresh water resources. The pesticides emitted to agricultural lands elevated extensively in Europe. On the other hand, coastal were polluted by the unknown emissions of organics namely polycyclic aromatic hydrocarbons, etc. by runoff. In some agricultural places irrigation waters was extensively used to irrigate the lands. These waters were originated from the domestic wastewater treatment plants and can be reused (Perez-Ruzafa et al., 2000, Moreno-Gonzal.ez et al., 2013]. Polycyclic aromatic hydrocarbons (PAHs) are organic compounds exhibiting inhibitory effects and originated from the pyrolysis of some organic structures. PAHs enter the human via air, water from aquatic ecosystems and cause mutations in DNA (Vijayanand et al. 2023, ISO 2022).

PAHs are subgroups hydrocarbons. They settle in food chains and have some inhibitory effects on life related to mutagenic properties and lethal effects (Clemons et al. 2004). It was observed that two subtypes of anthropogenic PAHs were taken into consideration: the PAHs were originated from petrochemical and pyrolysis sources. Petroleum originated PAHs coming from the oil emissions of raw and industrial petroleum. From these sources were emitted to aquatic places via some accidents, and discharges from some domestic emissions. These activities perform the production of PAHs with high weights (Brun et al. 2004, Liu et al. 2005). Furthermore, pyrolysis metabolites originated from the fossil fuels and from the death of bio organisms at elevated temperatures, from the pyrolysis of wood and emitted to air to for some dusts (Brun et al. 2004, NRC, 1983, Ramdahl et al. 1982, Tan et al. 1992). Pollution ways in the surface water was extensively researched since contained a lot concentration of PAHs. These compounds emitted to the surface waters via atmospheric facilities, emissions from domestic and industrial activities during oil spills. 14% and 89% of the inlet of PAHs to the aquatic biota related to dust precipitation.

Aromatic hydrocarbons are PAHs having benzene ring and relevant bonds between PAHs. They formed by benzene rings and can be defined as: • Bay Region – It was a last ring on the bay region • L Region - this varied between alpha to two fusion points. • K Region - this contained an electron density at all compositions. • All of places were effectively active. Epoxides originated at 3 sites (Polycyclic aromatic hydrocarbons). Bay place dihydrodiol epoxides were the carcinogenic species. Bay place products show a low percentage of the whole of the main hydrocarbon due to the metabolites produced a lot of points of the molecule. PAHs were compounds that do

organics containing atoms or rings having organic rings. PAHs were in water, air, soil, and oil, and in the textile metabolites by the formation of fossil fuels.
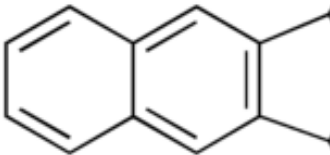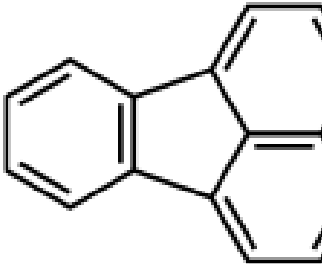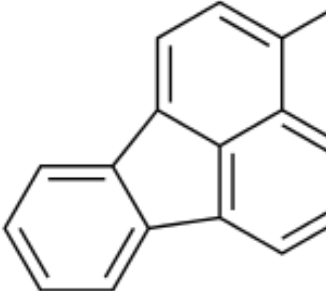
When the PAHs were released to the air, their rings and C atoms affects the distribution of PAH gases. PAHs with high carbons were adsorbed to the suspended matter, while PAHs with low C rings remained as gas products during settled via precipitation (Skupinska et al. 2004). PAH levels in water were about 1000 ng/L due to low solubility. This cause to accumulation in bays aquatic ecosystems. PAHs can be absorbed by vital mases and can be accumulated in land areas. Aromatic organics can be defined as benzene rings with its derivatives exhibiting good degradability. The source of Aromatic Hydrocarbons originated from fossil fuels like oil and coal. When fossil fuels were burned, PAHs emitted into atmosphere. About 200 PAHs were in atmosphere, lands and aquatic ecosystems. Benzo (a) pyrene, a source of cancer, is extensively utilized as an environmental precursor for PAHs (Polycyclic aromatic hydrocarbons, ATSDR, 2012)

1. MATERIALS AND METHODS
Chemicals used in this study

Analytical standards PAH-Mix 3 were taken from Sigma. Aldrich (Germany) containing the 3 compounds understudy, benzo [k]fluoranthene [BkF], fluoranthene [Fl]), and indene[1,2,3-cd]pyrene [In D] at dose varying between 1.2 to 6.2 g mL^{-1}.The physicochemical properties of the PAHs were illustrated in Table 1 [16]. PAHs standards were composed by dilution in a dissolvent in order to get the calibration data and admission doses. The methanol, acetonitrile, and dichloromethane solvents were analytical grade. Deionized water was taken from an ultrapure water device (Millipore, Merck Germany). Zinc oxide (ZnO) (99.9%, 10 m^2 g^{-1}, <70 m), titanium dioxide (TiO2) (99.9%, 45 m^2 g^{-1}, 32 nm, anatase/rutile 88/12) were taken from Merck, Germany. Sodium peroxydisulfate (98%) was taken from Thermo Scientific Chemicals - Fisher (US)

Table 1. Physical–chemical characteristics of the PAHs used in this study

PAH	Chemical structure	Molecular weight	Log KOW	Water solubility (mg L^{-1})	Log KOC
Benzo(k)fluoranthene [BkF]		252.3	5.8	1.5×10^{-3}	5.0
Fluoranthene [Fl]		202.2	5.2	2.6×10^{-1}	4.5
Indene(1,2,3-cd)pyrene [InD]		276.3	6.7	1.9×10^{-4}	6.2

Catalysts and Na$_2$S$_2$O$_8$ doses

During photocatalytic processes, the amount of photocatalyst and oxidant is the main significant parameters affecting the capability. The catalyst dose provides an inhibiting equilibrium at elevated catalyst doses. Therefore, it is necessary to optimize the semiconductor and oxidant doses in laboratory. A photoreactor with a volume of 2L is used with a stirring and 10 W mercury lamps between wave lengths of 300 and 460 nm was set up under batch operation. The optimum value for nanocomposite was between 150 and 200 mg L^{-1}. 92% TOC yield was detected after 200 min. The adding of S$_2$O$_8^{2-}$ into a photoreactor elevated the photo removals of PAHs, since the PAHs accepted more electrons than dissolved oxygen. As a result, via electron-hole recombination of Na$_2$S$_2$O$_8$, SO$_4$ was produced.

Sample extraction

The solid-phase extraction (SPE) apparatus from Merck-Sigma (Germany) was used to collect water samples (8 mL and 250 mg). The samples were first neutralised with 7 mL of dichloromethane and then rinsed with 6 mL of methanol and 6 mL of distilled water. Under vacuum, 50 mL of samples were extracted from the cartridges at a flow rate of 7 mL min1. Following that, 13 mL of dichloromethane was added to 7 mL of distilled water to distil the cartridges. Water content was removed with Na$_2$SO$_4$ and, the extracts were concentrated in an evaporator at a temperature of 24 °C to a volume of 1 mL under N$_2$ gas. As results, the rests were lowered to 0.3 mL. Then the sample filtered and kept in 1 mL vials and kept in a refrigerator.

HPLC analysis

The Alliance HPLC-FLD system was used to inject 10 g L1 samples. The separation module (Waters, Milford, USA) was fitted with an auto sampler, quaternary pump, vacuum degasser and fluorescence detector (Waters). Waters Empower® software was used to combine the data that were gathered. Super guard Discovery C18 guard column (18 mm × 3 mm inside diameter, 8 m, Merck-Sigma, Germany) was utilised with a Supercoil TM LC-PAH (6 cm, 4.2 mm inside diameter, 2 m diameter of column). At 280 and 480 nm in wavelength, assays were carried out.

Synthesis of ZnO photo catalyst

300 mL of ethanol were used to purify 10.98 g of zinc acetate dihydrate at 69 °C. After that, it was dissolved in 40 minutes. At 58 °C, 16 g of oxalic acid dehydrate were dissolved in 300 mL of ethanol. An ethanoic zinc acetate combination was added to the oxalic acid solution and stirred. A white gel was created and allowed to dry for 25 hours at 87 °C. For three hours, the product was calcined at 700 °C (Niu et al., 2012).

Production of ZnO under laboratory conditions

The ZnO was indicated with calcination of melamine (Huang et al., 2017). An incubator was used to raise the temperature of a cup containing 1.7 g of melamine to 590 °C over the course of seven hours. The item was used to make the composite (Rezaee et al., 2014).

Preparation of pH Buffers Solutions

40 g of potassium dihydrogen phosphate were dissolved in 7000 mL of deionized water to prepare the pH between 3.90 and 4. By adding 33 g of disodium hydrogen orthophosphate and 29 g of potassium dihydrogen phosphate, which were heated into solution in 7000 mL of distilled water, the pH was adjusted to 7.0 using potassium dihydrogen phosphate.

Photocatalytic Studies

Solar power plant

By using of sunlight in summer   Visible plus near-infrared values (mean ± SD) (430–1200 nm), UVA (319–409 nm), UVB (289–319 nm), and UVC (209–289 nm) radiation were applied with photo radiometer Delta Ohm HD 2102.2. Average VIS+NIR, UVA, UVB and UVC values at the 14th hour were 969.2 ± 23.9, 24.9 ± 1.9, 1.7 ± 0.2 and 0.2 ± 0.1 (all Wm-2 in), respectively.

Solar reactor

The durable quartz material used to create the solar energy reactor system has a 1.9 L capacity and measures 30 cm in height and 4 cm in diameter. The UV studies were conducted in continuous sunlight at power levels of 70.00–80.00 mW/m2 between 11:00 am and 16:00 pm, when solar radiation was at its strongest.

Power of sunlight

The densities of sunlight photo reactor were measured 33 mW/m^2 at 12:00 in autumn, 58 mW/m^2 at 12:00 in spring, 85 mW/m^2 at 12:00 in summer, 29 mW/m^2 at 12:00 in winter. Philips light meter Model DL-2001 was used to measure Sunlight Powers.

Characterization of ZnO

SEM and XRD measurements were used to establish the photocatalysts' physicochemical characteristics. Using a Philips model X' Pert pro MPD diffractometer operating at 1.96 kW and 49 kV, the crystallinity of the photocatalysts was examined. Using energy dispersive spectroscopy, the chemical configuration of the photocatalyst was determined (OECD, 2007, Daniel et al., 1980).

Kinetics of the photocatalytic process

Kinetics of PAHs degradation was calculated utilizing the first-order equation estimated:

$$C_t = C_0 \, e^{-kt} \text{ or } \ln = kt \tag{1}$$

where C_0 and C_t are the PAH concentration at times zero and t, respectively, and k the rate constant.

Regression analysis was used to get the first-order degradation rate constants. After substituting C for C0 / 2 in Eq. (1), half-lives (t1/2) were computed using the following formula:

$$t_{1/2} = \ln \tag{2}$$

When the times are short, this model works well. Even if acceptable correlation coefficient (R2) values were obtained, it is inappropriate to clarify the fate of contaminants when the reaction is prolonged. Other equations, such as those found in two phase models, can be utilised in the event that linear estimation is unsuccessful and produce results of greater quality. This is especially true when there is an initial phase of fast degradation followed by a subsequent phase in which the chemical vanishes more slowly. A modified version of Hoer's First-order model has been advantageously employed in some instances by certain writers [Sit et al., 1994]:

$$C_t = a \, e^{bt} \, t_c \tag{3}$$

or once linearized

$$\ln C_t = \ln a + b_t + c \ln t \tag{4}$$

a and b parameters are similar to C_0 and k in first-order model, and c is a standard deviation when $C < 0$, the function simulates a biphasic pattern (Zheng et al.,2007, Wan et al.,2005)

2. RESULTS AND DISCUSSION
Physicochemical Characterization

Scanning Electron Microscopy (SEM)

The morphological properties of the ZnO nanoparticles were investigated by SEM technique. SEM image (Figure 1), clearly

indicates that the ZnO nanoparticles exhibited homogeneous shape. From the SEM images it was found that the ZnO nanoparticles have some needles with a diameter of 32-61 nm. The nanoparticle, which exhibited rod-like structures due to these needles and spherical shape, showed high photocatalytic activity.
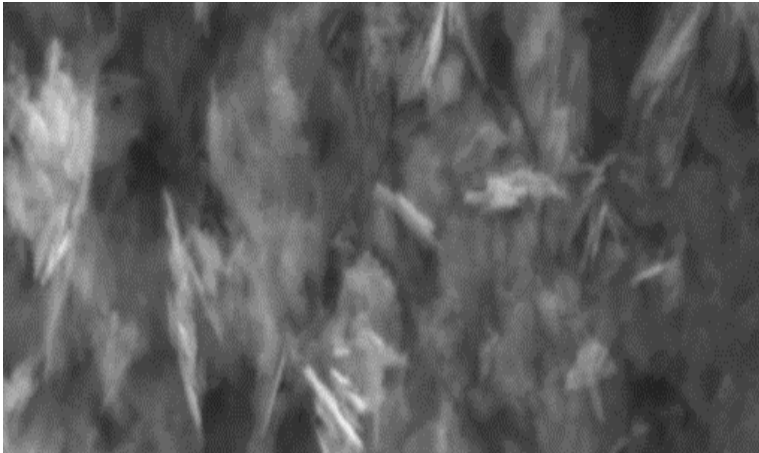
Figure 1. SEM Images of the ZnO nano particles

Transmission Electron Microscopy (TEM)

The samples were examined by TEM microscopy to detect the morphology and the extent distribution of the nanoparticles. From the TEM images it can be determined that the synthesized ZnO nanoparticles have a mean size of 50 nm. The TEM images also confirmed the presence of needles. These images were demonstrated in Figure 2.
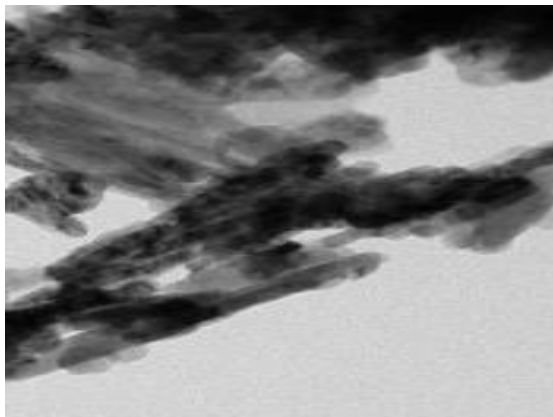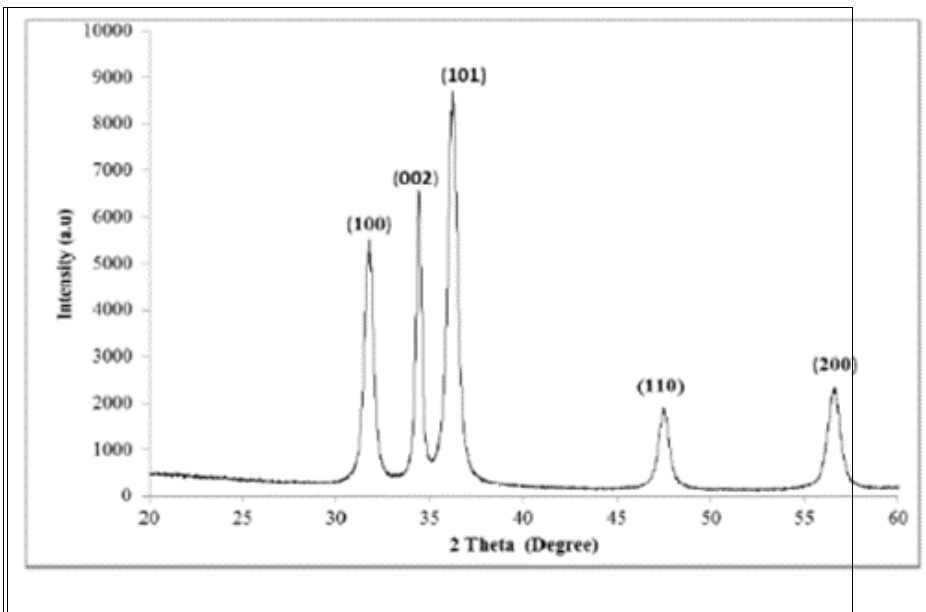

Figure 2. TEM Images of the ZnO nano particles

X-ray Diffraction Technique (XRD)

X-ray diffraction (XRD) was used to identify the synthesised ZnO nanoparticles. The peaks show a good degree of concordance with conventional diffraction peaks and display reflectance, suggesting the synthesis of ZnO (Figure 3). The diffraction peaks were narrow and denser and exhibited good crystalline nature. Furthermore, at the bottom side some short peaks exhibited the crystalline structure of ZnO.

Figure 3. XRD Image of the ZnO nano particles

CONCLUSIONS

In this study a nanocomposite namely $ZnO/Na_2S_2O_8$ was produced under laboratory condition to photodegrade the three PAHs (benzo[k] fluoranthene, fluoranthene, and indene [1, 2, 3-cd] pyrene. The effect of increasing nanocomposite concentration (1, 2, 3, 4, 5, 6 mg/L), photo degradation time (5, 10, 15, 25 and 30 min),PAH concentrations (0.5, 1, 1.5, 2, 3, 4, 5 micro g/L), sunlight irradiation power (2, 5, 15, 30, 60, 80 W/m$^{2)}$) on the photodegradation efficiencies of benzo[k]fluor5 anthene, fluoranthene, and indene [1, 2, 3-cd] pyrene PAHs were investigated. The optimal nanocomposite dose, photodegradation duration, PAH dose and sunlight intensity were 3 mg/l, 15 min, 3 and 5 micro g/L and 30 W/m^2 for 99% and 97% transformation efficiencies of benzo[k]fluoranthene, fluoranthene, and indene [1, 2, 3-cd] pyrene. Optimum $ZnO/Na_2S_2O_8$ dose was calculated as 1.2

mg/L to photodegrade 1.6 mg/L PAHs with an highest removal efficiency of 98% at a sun intensity of 80 mW/m^2 after 15 min at 42 $°C$ in summer. After 5th run assay, the ZnO/Na$_2$S$_2$O$_8$ was recovered with an efficiency of 97%. The photodegradation model of PAHs with a highest yield of 98% at a sun intensity of 80 mW/m^2 after 15 min at 42 $°C$ can be defined with the Langmuir-Hinshelwood (L-H) kinetic model. The use of solar energy in the presence of ZnO as the catalyst produces a very efficient method for the elimination of selected PAHs from surface water. A synergistic impact was detected by elevated the yield of the photodegradation by adding Na$_2$S$_2$O$_8$ as a good oxidant to the ZnO under sunlight.

By taken into consideration the pollution in surface water, photodegradation process offers a good a good treatment process compared to the other traditional water remediation methods. By using a renewable and energy save, economic green source the PAHs can be easily removed from the surface waters.

REFERENCES

Agency for Toxic Substances and Disease Registry (ATSDR) Case Studies in Environmental Medicine Toxicity of Polycyclic Aromatic Hydrocarbons (PAHs) July 1, 2012.

C. Hariharan.(2006)Photocatalytic degradation of organic contaminants in water by ZnO nanoparticles: Revisited, Applied Catalysis A: General 304, 55-61

C. Daniel, F. Woods, Fitting Equations to Data, 2nd ed., John Willey & Sons, New York, (1980).

G. Brun, O. Vaidya, M. Léger, (2004) Atmospheric deposition of polycylic aromatic hydrocarbons to Atlantic, Canada: geographic and temporal distributions and trends 1980–2001, Environ. Sci. Technol. 38 1941–1948.

Huang W, Liua N, Zhanga X, Wub M, Tang L. Metal organic framework g-C3N4/MIL-53(Fe) heterojunctions with enhanced photocatalytic activity for Cr(VI) reduction under visible light. Applied Surface Science, 425, 107-116, (2017).

J. Clemons, L.Allan, C. Marvin, Z.Wu, B. McCarry, D. Bryant, (2004) Evidence of estrogen and TCDD-like activities in crude and fractionated extracts of PM10 air particulate material using in vitro gene expression assays, Environ. Sci. Technol. 32 1853–1860

M.Vijayanand , A. Ramakrishnan , R. Subramanian , P.Kumar Issac, M.Nasr, K. Shiong Khoo , R.Rajagopal , B. Greff , N.I. Wan Azelee , B-H. Jeon , S.W. Chang , B. Ravindran .(2023)Polyaromatic hydrocarbons (PAHs) in the water environment: A review on toxicity, microbial biodegradation, systematic biological advancements, and environmental fate, Environmental Research 227, 115716

M. Pérez-Moya, M. Graells, P. Buenestado, H.D. Mansilla, A comparative study on the empirical modeling of Photo. Fenton process performance, Appl. Catal. B: Environ. 84 313–323.(2008).

Moreno-Gonzalez, R., J. A. Campillo and V. M. Leon (2013) Influence of an intensive agricultural drainage basin on the seasonal distribution of organic pollutants in seawater from a Mediterranean coastal lagoon (Mar Menor, SE Spain). Mar. Pollut. Bull. 77, 400– 411

New ISO Test Method Published for the Determination of Polycyclic Aromatic Hydrocarbons (PAHs) in Footwear Materials January 18, (2022).

Niu P, Zhang L, Liu G, Cheng H-M. Graphene-like carbon nitride nanosheets for improved photocatalytic activities Advanced Functional Materials, 22, 4763-4770, (2012).

NRC, Polycyclic Aromatic Hydrocarbons: Evaluation of Sources and Effects, National Research Council, National Academy Press, ES/l-ES/7, Washington, D.C., (1983).

OECD, Organisation for Economic Cooperation and Development. Guidelines for Testing of Chemicals, No. 312, Leaching in Soil Columns, Paris, (2007).

Perez-Ruzafa, A., S. Navarro, A. Barba, C. Marcos, M. A. Camara, F. Salas and J. Gutierrez (2000). Presence of pesticides throughout trophic compartments of the food web in the Mar Menor Lagoon (SE Spain). Mar. Pollut. Bull. 40, 140–151.

Polycyclic aromatic hydrocarbons, https://www. slideserve.com/ Audrey/pahs

Polycyclic Aromatic Hydrocarbon (PAH) Reference Materials

Rezaee, Abbas; Rangkooy, Hossinali; Khavanin, Ali; Jafari, Ahmad Jonidi. High photocatalytic decomposition of the air pollutant formaldehyde using nano-ZnO on bone char. Environmental Chemistry Letters, 12(2), 353–357. (2014).

Skupinska K, Misiewicz I, KasprzyckaGuttman T. Polycyclic aromatic hydrocarbons: Physiochemical properties, environmental appearance and impact on living organisms. Acta Poloniae Pharmaceutica. 61(3):233-24(2004).

T. Ramdahl, I. Alfheim, A. (1982) Bjorseth, Nitrated polycyclic aromatic-hydrocarbons in urban air particles, Environ. Sci. Technol. 16 861–865. US EPA, Estimation Programs Interface SuiteTM for Microsoft® Windows, v4.1, United States Environmental Protection Agency, Washington, D.C.,(2011).

V. Sit, M. Poulin-Costello, Catalogue of Curves for Curve Fitting. Biometrics Information, Handbook, 4, British Columbia Ministry of Forests, Victoria, BC, (1994)

Q Wan, TH Wang, and JC Zhao, Enhanced photocatalytic activity of ZnO nanotetrapods. Appl. Phys. Letters, 87: p. 083105-083107-(2005).

X. Liu, G. Zhang,K.Jones,X. Li,X. Peng, S. Qi, (2005) Compositionalfractionation of polycyclic aromatic hydrocarbons (PAHs)in mosses (Hypnum plumaeformaeWILS) from the northern slop of Nanling Mountains, South China, Atmos. Environ. 39 5490–5499.

Y.L. Tan, J.F. Quanci, R.D. Borys, (1992) Polycyclic aromatic hydrocarbons in smoke particles from wood and duff burning, Atmos. Environ. 26 1177–1181.

Y Zheng, et al., Luminescence and Photocatalytic activity of ZnO nanocrystals: Correlation between Structure and Property. Inorg. Chem,. 46:p. 6675- 6682 (2007).

https://www.atsdr.cdc.gov/csem/polycyclicaromatichydrocarbons/whearepahs_found.html#print